Cloaked contact grids for perovskite-silicon tandem solar modules

Zur Erlangung des akademischen Grades eines

Doktor-Ingenieurs

von der KIT-Fakultät für
Elektrotechnik und Informationstechnik
des Karlsruher Instituts für Technologie (KIT)

genehmigte

Dissertation

von

Malte Langenhorst, M. Sc.
geb. in Münster

Tag der mündlichen Prüfung:	04.12.2019
Hauptreferent:	Dr. Ulrich W. Paetzold
Korreferenten:	Prof. Dr. Bryce S. Richards
	Prof. Dr. Carsten Rockstuhl

Table of Contents

Kurzfassung

Photovoltaik (PV) spielt eine wichtige Rolle bei der Transformation des globalen Energiesystems von fossilen Brennstoffen hin zu erneuerbaren Energiequellen, die ein Schlüssel zu einer nachhaltigen Zukunft des Planeten Erde ist. Eine solche Transformation wird jedoch hauptsächlich durch die wirtschaftliche Wettbewerbsfähigkeit einer Technologie getrieben, für die die Stromgestehungskosten ein entscheidender Faktor sind. In den letzten Jahren sind die Preise für Solarmodule drastisch gesunken, so dass die weitere Steigerung des Wirkungsgrades (PCE) und des Energieertrags (EY) von PV-Anlagen von zunehmender Bedeutung ist, um die wirtschaftliche Wettbewerbsfähigkeit der PV zu verbessern.

Einer der limitierenden Faktoren moderner Solarmodule ist die Verlustleistung aufgrund inaktiver Flächen, die zur Minimierung der resistiven Verluste während des Ladungstransports über die großen Abmessungen eines Solarmoduls erforderlich sind. Optische Tarnkonzepte haben die Fähigkeit, Licht von inaktiven Bereichen hin zu den aktiven Flächen eines Solarmoduls zu leiten, wodurch die entsprechende Verlustleistung reduziert wird. Unter den verschiedenen optischen Tarnkonzepten sind Freiformoberflächen (FFS) als Tarnkappen eine interessante Technologie, die omnidirektionales Tarnen von inaktiven Flächen verspricht.

Diese Dissertation konzentriert sich auf die Entwicklung und Herstellung von FFS mit der anvisierten Anwendung auf Perowskit/Silizium-Tandem-Solarmodulen, die ihrerseits sowohl für die Forschung als auch für die Industrie von höchstem Interesse sind, da die Kombination zweier Absorbermaterialien das theoretische Limit der PCE von 29 % für Einfachsolarzellen auf 46 % für Tandemsolarzellen erhöht. Eine detaillierte Untersuchung der optischen Verluste mittels optischer Simulation und EY-Modellierung von zwei- (2T) und vier-poligen (4T) Perowskit/Silizium-Tandemsolarmodulen in dieser Arbeit zeigt, dass Leistungsverluste durch inaktive Flächen – neben der parasitären Absorption – einer der größten optischen Verlustmechanismen von Perowskit/Silizium-Tandemsolarmodulen sind.

Auch wenn FFS in einem idealen Design eine perfekte Tarnung von inaktiven Flächen aufweisen, sind sie nicht mit der herkömmlichen Architektur von Solarmodulen kompatibel, da sie eine nicht planare, für Verschmutzung anfälligere Oberfläche aufweisen. Um Verschmutzungen zu vermeiden, wird die Einbettung von FFS unter einer Glasabdeckung untersucht und hierfür zwei optimierte Designs von Freiformoberflächen vorgeschlagen, die unter Berücksichtigung eines geometrischen Füllfaktors (GFF) von inaktiven Flächen von 4 % die Einstrahlungsleistung auf die aktive Fläche theoretisch um 3.5 % erhöhen. Die Fähigkeit des omnidirektionalen Tarnen wird jedoch durch die vorgeschlagenen Designs beeinträchtigt, was zu einem etwas geringeren Anstieg des EY unter realistischen Einstrahlungsbedingungen von 2.4 % jährlich führt. Die effektive Tarnung inaktiver Flächen verschiebt zudem den optimalen Abstand und die optimale Dicke der Frontelektrode. Unter einer zusätzlichen Optimierung der Frontkontaktierung, erhöht sich der Anstieg in EY durch den Einsatz von eingebetteten FFS weiter auf 3.1 %.

Prototypen von Einfachsolarzellen aus $CuIn_xGa_{1-x}Se_2$ (CIGS) und kristallinem Silizium (c-Si) zeigen zwei mögliche Ansätze zur Einbettung von FFS in die vorderen Verkapselungsschichten konventioneller Solarmodule auf: (1) Prägen von FFS in das polymere Verkapselungsmaterial und Einbetten unter einer Glasabdeckung, was zu einer Erhöhung der Kurzschlussstromdichte J_{SC} eines CIGS-Solarmoduls um 4.1 % bei einem GFF inaktiver Flächen von 4.7 % führt, und (2) Einbetten von FFS-Cloaks direkt in das Deckglas durch Anwendung der Flüssigglastechnik, die den J_{SC} von c-Si-Solarzellen um 3.8 % bei einem GFF von 4.4 % erhöht. Beide Ansätze stellen eine praktikable Option für die Anwendung von FFS in 2T Perowskit/c-Si-Tandemsolarmodulen dar. Für 4T Perowskit/c-Si-Tandemsolarmodule ist die Abscheidung der Perowskitsolarzelle (PSC) direkt auf der Glasabdeckung vorzuziehen, da sie Frontschichten höherer optischer Qualität ermöglicht. Um eine Oberflächenqualität zu erreichen, die die Abscheidung der konformen dünnen Schichten einer PSC unterstützt, wird die mit der Flüssigglastechnik hergestellte Glasabdeckung mechanisch poliert. Die Herstellung von funktionierenden Perowskitsolarzellen ist jedoch noch nicht erfolgreich. Die

optische Charakterisierung bestätigt jedoch das effiziente Tarnen von inaktiven Flächen mittels diesen Ansatzes, unterstreicht aber auch die starke Abhängigkeit von optischen Tarnkonzepten von ihrer Ausrichtung bezüglich der inaktiven Flächen.

Im Hinblick auf die zukünftige Entwicklung bleiben die erfolgreiche Abscheidung von PSCs auf Glasabdeckungen, die mit der Flüssigglastechnik hergestellt werden, die Verbesserung der Ausrichtung und die Aufskalierung der Technologie offene Herausforderungen.

Abstract

Photovoltaics (PV) play an important role in the transformation of the global energy system towards renewable energy sources with a smaller CO_2 footprint than fossil fuels, which is a key to a sustainable future of planet earth. However, such a transformation is mainly driven by the economic competitiveness of a technology, for which the levelized cost of electricity (LCoE) is a decisive factor. In recent years, prices for solar modules have drastically fallen, so that advancing the power conversion efficiency (PCE) and energy yield (EY) of PV systems is of increasing relevance to improve the economic competitiveness of PV.

One of the limiting factors of state-of-the-art solar modules is power loss originating from inactive areas, which are required for minimizing resistive losses of charge transport across the large dimensions of a solar module. Optical cloaking concepts have the ability to guide light away from inactive areas and towards the active area of a solar module reducing the corresponding power loss. Among various concepts, freeform surface (FFS) cloaks stand out as an intriguing technology that promises omnidirectional cloaking and, thus, effectively invisible inactive areas.

This thesis focuses on the development and fabrication of FFS cloaks with the targeted application to perovskite/silicon tandem solar modules, which themselves are of highest interest to both research and industry since the combination of two absorber materials in a tandem architecture increases the theoretical limit in PCE from 29 % for single-junction PV to 46 %. A detailed study of optical losses via optical simulations and EY modelling of two-terminal (2T) and four-terminal (4T) perovskite/silicon tandem solar modules in this thesis reveals that power losses due to inactive areas are – besides parasitic absorption – one of the major optical loss mechanisms of perovskite/silicon tandem solar modules.

Even though FFS cloaks in an ideal design yield perfect cloaking of inactive areas, they lack compatibility with the conventional architecture of solar modules since they exhibit a non-planar surface that increases their susceptibility to soiling. To evade any issues associated to soiling, the embedment of FFS cloaks under a protective cover glass is suggested and two optimized designs of FFS cloaks are proposed, which theoretically boost the power incident on the active area by 3.5 % considering a geometrical filling fraction (GFF) of inactive areas of 4 %. However, the ability of omnidirectional cloaking is compromised by the proposed designs, which leads to slightly smaller increase in EY under realistic irradiation conditions of 2.4 % annually. The effective cloaking of inactive areas shifts the optimum spacing and optimum thickness of the front electrode. Once the front contacting scheme is optimized additionally, the benefit in EY of employing embedded FFS cloaks raises further to 3.1 %.

Prototypes of $CuIn_xGa_{1-x}Se_2$ (CIGS) and crystalline silicon (c-Si) single-junction solar cells demonstrate two possible approaches to embed FFS cloaks into the front encapsulation layers of conventional solar modules: (1) imprinting FFS cloaks into the polymeric encapsulant and covering them under a cover glass, which results in a boost in short-circuit current density J_{SC} of a CIGS solar module by 4.1 % for a GFF of 4.7 %, and (2) embedding FFS cloaks directly into the cover glass by applying the liquid glass technique, which increases the J_{SC} of c-Si solar cells by 3.8 % for a GFF of 4.4 %. Both approaches represent a viable option for the application of FFS cloaks to 2T perovskite/c-Si tandem solar modules. For 4T perovskite/c-Si tandem solar modules, the deposition of the perovskite top-cell directly on the cover glass is preferable since it enables optically superior front layers. To achieve a surface quality that supports the deposition of the conformal thin films of a perovskite solar cell (PSC), the cover glass fabricated via the liquid glass technique is mechanically polished. However, the fabrication of working perovskite solar cells is not yet successful. Optical characterization confirms the efficient cloaking of inactive areas via this approach but also highlights the crucial sensitivity of optical cloaking concepts to their alignment with the inactive areas.

In view of future development, the successful deposition of PSCs on cover glasses fabricated via the liquid glass technique, improving alignment and rapid large-scale fabrication remain open challenges.

Acknowledgements

First, I would like to thank my supervisor Dr. Ulrich W. Paetzold for giving me the chance to pursue my PhD as one of the first students in his research group “Advanced Optics for Photovoltaics” at the Karlsruhe Institute of Technology. I am very grateful for his guidance and the trust he placed in me. Furthermore, I would like to thank Prof. Dr. Bryce S. Richards for his continuous support and for creating such a positive and productive environment in his division at the Institute of Microstructure Technology.

Special thanks goes to my colleague Raphael Schmager for the many productive joint projects. The numerous scientific and non-scientific discussions that already started during our master thesis will be fondly remembered. Moreover, I would like to thank Dr. Martin F. Schumann for sharing his vision of freeform surfaces with me and assisting me along the first steps of my PhD. Additionally, I am very grateful to all my collaboration partners during my thesis, namely Tobias Abzieher, Thomas Feeney, Ihteaz Hossain, Jonathan Lehr and Prof. Dr. Uli Lemmer from the Light Technology Institute at KIT, Dr. Frederik Kotz, Patrick Risch and Prof. Dr. Bastian E. Rapp from the Department of Microsystems at the University of Freiburg, Dr. Daniel A. Jacobs from the Australian National University in Canberra, Dr. Florent Sahli from the École Polytechnique Fédérale de Lausanne, Dr. Kaining Ding from the Forschungszentrum Jülich, Dr. Erik Ahlswede and Prof. Dr. Michael Powalla from Zentrum für Sonnenenergie- und Wasserstoff-Forschung Baden-Württemberg. In addition, I am very grateful to my three master students Benjamin Sautter, Pere Casas Soler and David Ritzer for their contribution to my thesis and being the first test objects in managing personnel.

I want to thank the Karlsruhe School of Optics and Photonics for supporting my travels to conferences financially and for enabling me to expand my skill set.

In the beginning of my PhD in 2016, our research group consisted of just three PhD students and our supervisor, but with time, the group increased rapidly. I intensively enjoyed the semi-scientific and semi-social Team Days with my two research groups from the Institute of Microstructure Technology and the Light Technology Institute. The new friends I met during my PhD very much enriched my life and I would like to thank Tobias Berger, my office companion Marius Jakoby, Roman Lyubimenko, Natalia Kiseleva for sharing laughs and adventures outside from working hours. In particular, the two latter I want to thank for the few words of Russian that I am now capable of. Finally yet importantly, I would also like to thank Philipp Brenner, Hennig Mescher and Dominik Theobald for trading nutmegs during football sessions on Monday evenings.

Ein besonderer Dank gilt zudem natürlich meiner Familie. Ganz besonders meinen Eltern Falko und Simone, die mich immer bedingungslos unterstützt haben. Die Freiheit meinen Träumen nachzugehen, haben sie mir erst ermöglicht. Auch meinen Geschwistern Maren und Niels bin ich sehr dankbar für ihre mentale Unterstützung. Unter anderem durch sie war ich in der Lage alle Sorgen und Probleme, die eine Doktorarbeit mit sich bringt für ein paar Momente zu vergessen. Ich bin meiner Freundin Verena unermesslich dankbar, dass sie mich während meiner Doktorarbeit begleitet, unterstützt und auch in schwierigen Phasen ausgehalten hat. Ihr Verständnis für längere Abende vor dem PC und ihre Einfühlsamkeit in frustrierenden Phasen haben mir immer wieder neue Kraft gegeben.

List of abbreviations

PV	Photovoltaic
LCoE	Levelized cost of electricity
PCE	Power conversion efficiency
BOS	Balance of system
c-Si	Crystalline silicon
ITRPV	International technology roadmap for photovoltaics
CIGS	$CuIn_xGa_{1-x}Se_2$
GFF	Geometrical filling fraction
FFS	Freeform surface
J-V	Current density – voltage characteristic
EQE	External quantum efficiency
STC	Standard test conditions
J_{SC}	Short-circuit current density
V_{OC}	Open-circuit voltage
ETL	Electron transport layer
HTL	Hole transport layer
TCO	Transparent conductive oxide
TMM	Transfer-matrix method
DLW	Direct laser writing
TPP	Two-photon polymerization
IPA	Isopropanol
PGMEA	Propylene glycol methyl ether acetate
UV	Ultraviolet
PDMS	Poly dimethyl siloxane
ALD	Atomic layer deposition
PFOTS	Trichloro (1*H*,1*H*,2*H*,2*H*-perfluorooctyl) silane
IPA	Isopropanol
PGMEA	Propylene glycol methyl ether acetate
UV-NIL	Ultraviolet nanoimprint lithography
HEMA	Hydroxy ethyl methacrylate
POE	Phenoxy ethanol
TEGDA	Tetraethylene glycol diacrylate
DMPAP	2,2-dimethoxy-2-phenylacetophenone
EVA	Ethylene vinyl acetate
Spiro-TTB	2,2',7,7'-Tetra(*N*,*N*-di-*p*-tolyl)amino-9,9-spirobifluorene
BCP	Bathocuproine
AFM	Atomic force microscopy
AM1.5G	Air mass 1.5 global
EY	Energy yield
CC	Cloud coverage
TMY	Typical meteorological year
NREL	National renewable energy laboratory
MPP	Maximum power point
SMARTS	Simple model of atmospheric transfer of sunlight
APE	Average photon energy
NOCT	Nominal operating cell temperature
Spiro-OMeTAD	2,2’,7,7’-tetrakis(*N*,*N*-di-4-methoxyphenylamino)-9,9’-spirobifluorene
ITO	Indium tin oxide
FTO	Fluorine-doped tin oxide
NIR	Near-infrared
ARC	Anti-reflection coating
LM	Light management
IZO	Indium zinc oxide
PTAA	Poly[bis(4-phenyl)(2,4,6-trimethylphenyl)amine
SWCT	SmartWire contacting technology
PMMA	Polymethylmethacrylate
RMS	Root mean square
PSC	Perovskite solar cell

List of publications

Peer-reviewed journal publications as first author or shared first author

Parts of this thesis have already been published in peer-reviewed scientific journals:

- **M. Langenhorst**, M. F. Schumann, S. Paetel, R. Schmager, U. Lemmer, B. S. Richards, M. Wegener, and U. W. Paetzold, “Freeform surface invisibility cloaking of interconnection lines in thin-film photovoltaic modules,” Sol. Energy Mater. Sol. Cells **182**, 294–301 (2018).
- **M. Langenhorst**, B. Sautter, R. Schmager, J. Lehr, E. Ahlswede, M. Powalla, U. Lemmer, B. S. Richards, and U. W. Paetzold, "Energy yield of all thin-film perovskite/CIGS tandem solar modules," Prog. Photovoltaics Res. Appl. **27**(4), 290–298 (2019).
- **M. Langenhorst**, D. Ritzer, F. Kotz, P. Risch, S. Dottermusch, A. Roslizar, R. Schmager, B. S. Richards, B. E. Rapp, and U. W. Paetzold, "Liquid glass for photovoltaics: multi-functional front cover glass for solar modules," ACS Appl. Mater. Interfaces **11**(38), 35015–35022 (2019).

The energy yield modelling framework developed for this thesis has been used by the author for simulations together with colleagues and collaboration partners, leading to shared first authorships in the following publications:

- J. Lehr, **M. Langenhorst**, R. Schmager, S. Kirner, U. Lemmer, B. S. Richards, C. Case, and U. W. Paetzold, "Energy yield modelling of perovskite/silicon two-terminal tandem PV modules with flat and textured interfaces," Sustain. Energy Fuels **2**(12), 2754–2761 (2018).
- R. Schmager, **M. Langenhorst**, J. Lehr, U. Lemmer, B. S. Richards, and U. W. Paetzold, "Methodology of energy yield modelling of perovskite-based multi-junction photovoltaics," Opt. Express **27**(8), A507 (2019).
- D. A. Jacobs, **M. Langenhorst**, F. Sahli, B. S. Richards, T. P. White, C. Ballif, K. R. Catchpole, and U. W. Paetzold, "Light Management: A Key Concept in High-Efficiency Perovskite/Silicon Tandem Photovoltaics," J. Phys. Chem. Lett. **10**(11), 3159–3170 (2019).

Peer-reviewed journal publications as co-author

Assistance in the characterization of an early prototype of freeform surface cloaks applied to silicon solar cells resulted in a co-authorship of the following publication:

- M. F. Schumann, **M. Langenhorst**, M. Smeets, K. Ding, U. W. Paetzold, and M. Wegener, “All-Angle Invisibility Cloaking of Contact Fingers on Solar Cells by Refractive Free-Form Surfaces,” Adv. Opt. Mater. **5**(17), 1700164 (2017).

Furthermore, cooperation in other fields closely connected to light management in photovoltaics led to further co-authorships:

- B. Fritz, M. Guttmann, P. Casas Soler, A. Roslizar, **M. Langenhorst**, M. Schneider, U. W. Paetzold, B. S. Richards, U. Lemmer, R. Huenig,and G. Gomard, "Towards mass fabrication of hot embossed plant surface texture replicas as photovoltaic cover layers," in *Nanoengineering: Fabrication, Properties, Optics, and Devices XV* (SPIE, 2018), **10730**, pp. 1–17.

- S. Dottermusch, D. Busko, **M. Langenhorst**, U. W. Paetzold, and B. S. Richards, “Exposure-dependent refractive index of nanoscribe ip-dip photoresist layers,” Opt. Lett. **44**(1), 29-32, (2019).
- J. Lehr, **M. Langenhorst**, R. Schmager, S. Kirner, U. Lemmer, B. S. Richards, C. Case, and U. W. Paetzold, "Energy yield modelling of perovskite/silicon two-terminal tandem PV modules with flat and textured interfaces," Sol. Energy Mater. Sol. Cells **accepted** (2019).

Conference contributions

Parts of this thesis have been presented at international scientific conferences:

- **M. Langenhorst**, M. F. Schumann, R. Schmager, J. Lehr, U. Lemmer, M. Wegener, B. Richards, and U. W. Paetzold, "Performance of Silicon Solar Cells with Cloaked Contact Fingers under Realistic Conditions," *Optical Nanostructures and Advanced Materials for Photovoltaics 2017*. Boulder (CO), United States (6–9 November 2017). Oral presentation.
- **M. Langenhorst**, M. F. Schumann, R. Schmager, J. Lehr, U. Lemmer, B. S. Richards, M. Wegener, and U. W. Paetzold, "Optimization of encapsulated invisibility cloaks for solar modules," *Photonics for Solar Energy Systems*. Straßbourg, France (23–25 April 2018). Oral presentation.
- **M. Langenhorst**, J. Lehr, B. Sautter, R. Schmager, U. Lemmer, B. Richards, and U. W. Paetzold, " Energy Yield Modelling of Wide Bandgap Perovskite-Based Tandem Solar Modules," *Optics for Solar Energy 2018*. Singapore (5–8 November 2018). Oral presentation.
- **M. Langenhorst**, D. Ritzer, F. Kotz, P. Risch, I. Hossain, S. Dottermusch, A. Roslizar, R. Schmager, B. S. Richards, B. E. Rapp, U. W. Paetzold, “Advanced optical microstructures embedded in transparent encapsulation glass for photovoltaics,” *Physics, Simulation, and Photonic Engineering of Photovoltaic Devices VIII*. San Francisco (CA), United States (8 March 2019). Oral presentation.

1 Introduction

In the year 2018, the global energy consumption increased by 2.9 %, the largest growth since 2010 and nearly double the average growth of the preceding ten years [1]. Based on the continuation of this trend, the global energy demand is predicted to increase by more than 25 % until 2040 [2]. In particular, electricity is expected to account for the largest share of global energy demand. In view of the threat of climate change and the indispensable decarbonisation of energy production, renewable energy sources, such as photovoltaics (PV) and wind, are key to a sustainable future of planet earth. However, the transformation of the energy system is not a matter of lowest carbon emission in energy production only, but is mainly driven by economics. Here, the decisive factor is the levelized cost of electricity (LCoE).

In the past two decades, a remarkable reduction of fabrication costs of solar modules due to automated mass production has led PV to become one of the main driving forces – besides wind energy – that are transforming the global electricity mix [2,3]. This progression is caused by the employment of more efficient PV technologies, the substitution of expensive materials, and more efficient production processes of solar modules that rely on automated mass production and consume less material [4]. The continuous reduction of fabrication costs of solar modules manifested itself in a steep learning curve, which states that module prices fall by remarkable 24 % with each doubling of cumulative module production [3]. As a result, PV outperforms every other energy technology with LCoE as low as 4 €cent/kWh as of 2018, assuming utility-scale installations (>2 MWp) in Germany [4].

To maintain economic competitiveness in the future and to uphold the learning curve, either installation costs have to decrease or the power conversion efficiency (PCE) of solar modules has to increase. The former, however, is not only determined by module costs but also costs associated to the balance of system (BOS), whose share of the total cost increased to more than 50 % due to strong reduction of solar module costs [3]. Consequently, higher PCEs play a crucial role in sustaining the economic competitiveness of PV on the energy market.

Tandem photovoltaics

In fact, a trend towards highly efficient solar modules is emerging: (1) the market share of the more efficient crystalline silicon (c-Si) heterojunction technology is increasing drastically, (2) the fabrication of bifacial solar modules is rapidly growing, and (3) highly-efficient multi-junction – in particular tandem – solar modules appear on the International Technology Roadmap for Photovoltaics (ITRPV) [5]. In particular, tandem solar modules are heavily investigated in both industry as well as academia since they promise to overcome the PCE limit of single-junction PV of approximately 29 % [6,7]. By the combination of two absorbers with different bandgaps, the utilizable power density increases significantly compared to single-junction PV as illustrated in **Figure 1.1** and the theoretical limit shifts to a value of around 46 % [8].

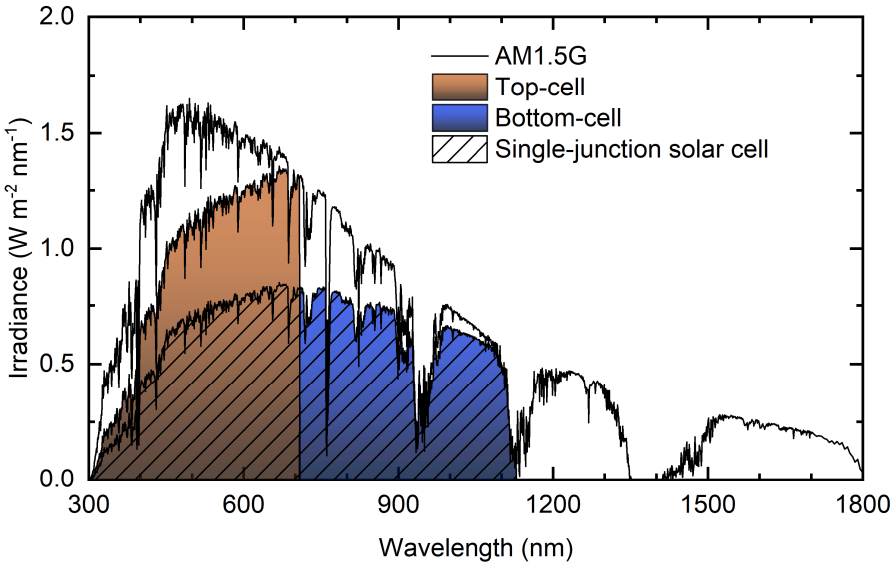

Figure 1.1: Maximum utilizable power density out of the AM1.5G spectrum assuming no optical losses of a tandem solar cell, which consists of a top- and bottom-cell, compared to a single-junction solar cell. Adapted with permission from [9]. © John Wiley & Sons, Ltd.

Potential candidates for a combination with c-Si in a tandem architecture are III/V semiconductors, such as GaAs, and metal-halide perovskites [10–17]. While the use of former results in very high PCEs of up to 32.8 % [18], the latter have the unique advantage of potentially representing a low-cost add-on technology to market-dominating silicon solar cells. The possibility to apply solution-processing techniques promises to reduce production costs. High absorption coefficients and excellent electrical properties ensure high efficiencies that metal-halide perovskites reach 25.2 % in single-junction configuration [19]. Since perovskites comprise an entire material group that are defined by the same crystal structure ABX_3 (A = cation, B = cation, X = anion), the search for more promising materials is still ongoing [20]. The freedom to engineer their composition allows tuning the bandgap of metal-halide perovskite by mixing different halide anions such as iodide and bromide according to the application. The resulting bandgap range of roughly 1.55–2.3 eV covers the predicted optimal bandgap of ~1.7–1.8 eV for silicon-based tandem solar modules [8,21–25]. Focused research has successfully pushed the PCE of perovskite/c-Si tandem devices beyond the PCE of their respective single-junction bottom-cells [26–32]. The latest certified record PCE of a perovskite/c-Si tandem solar cell of 28% set by the company OxfordPV™ [32] already outperforms the record PCE of single-junction c-Si solar cells of 26.7% significantly [33]. This development has been quite remarkable, in particular for perovskite/c-Si tandem PV, but also for the alternative tandem technology perovskite/$CuIn_xGa_{1-x}Se_2$ (CIGS) [34]. Potentially, perovskite-based tandem PV is capable of even surpassing PCEs of 30 % [35–39].

Optical cloaking

Since LCoE reduce with increasing PCEs of solar modules, research efforts are directed towards maximizing the amount of harvestable light per area via the minimization of inactive areas of solar modules. Inactive areas are a key requirement for low resistive losses and an efficient transport of generated charge carriers. These areas are mainly comprised by metallic contact grids (fingers and bus bars) in conventional silicon PV and interconnection lines in thin-film PV. The share of inactive area in the total area of the solar module is defined as the geometrical filling fraction (GFF). Metallic contact grids are responsible for the lateral charge transport across the large dimensions of a solar module, whereas interconnection lines of thin-film PV monolithically connect a large number of individual sub-cell in series and maintain low resistive losses in this

way. A detailed overview of optical losses in solar modules – in the context of perovskite/c-Si tandem PV – and an evaluation of the potential of reducing the optical impact of inactive areas are provided in Chapter 5. Even though, many efforts are dedicated to reduce the optical footprint of inactive areas by modifying the cross-section of metallic contact grids [40–44] or by shrinking the scribing lines of the interconnections, these inactive areas still add to a GFF of around 5 % [45–51].

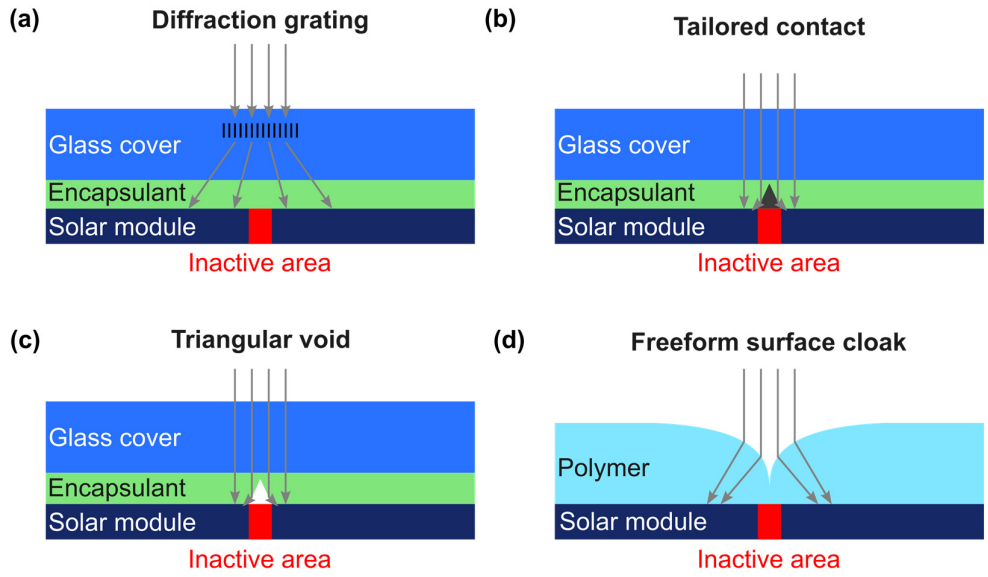

Figure 1.2: Overview of various optical concepts to reduce the impact of inactive areas on the current generation of solar modules. The concepts exploit (a) diffraction by gratings, (b) reflection by tailored contacts, (c) total internal reflection by triangular voids, and (d) refraction by freeform surface cloaks.

One way to reduce or even to eliminate the optical footprint of inactive areas is to guide incident light towards the active areas by optical cloaking concepts. In recent years, various of such concepts have been reported in literature that rely on diffractive optics [52,53], reflection [40–42,54,55] and refraction [56–60] of incident light. The key requirements for the application of optical cloaking concepts in PV are the effective cloaking of inactive areas under solar irradiation on the one hand and the compatibility with the conventional architecture of solar modules, which typically consist of a polymeric encapsulant and a planar protective cover glass on the other. In view of these requirements, all concepts shown in **Figure 1.2** have their advantages and disadvantages:

- **Diffractive optics:** Diffractive optics (see **Figure 1.2a**) scatter light incident on the inactive area so that only a smaller share of the incident power eventually reaches the inactive area. However, any approach to improve light harvesting of solar irradiation based on diffractive optics suffers from its strong dependence on the angle of incidence and wavelength [52,53].
- **Tailored contacts:** Metallic contacts with triangular cross-sections as depicted in **Figure 1.2b** successfully demonstrate to be effectively transparent [40–42]. Yet, the fabrication of tailored contacts remains challenging [61,62] compared to screen-printed contacts. In addition, tailored contacts only pose a potential solution for metallic contact grids of silicon PV and not to the interconnection lines of thin-film solar modules.
- **Triangular voids:** The sidewalls of triangular voids (see **Figure 1.2c**) embedded into the encapsulant of a solar module redirect light towards the active area by total internal reflection [54,55]. To maintain total internal reflection for all angles of incidence, triangular voids require a large aspect ratio (height divided by base width) of ~4.8. Cloaking metallic contact fingers with a typical width of ~40 µm via the incorporation of triangular voids into the polymeric encapsulant seems feasible, since the

minimum height of a triangular void placed directly on top of the inactive area of ~200 µm (base width of 40 µm times aspect ratio of 4.8) remains below common thicknesses of polymeric encapsulants of 400 – 460 µm [5]. However, the usually ~200 µm-wide interconnection lines of thin-film solar modules pose a fundamentally different problem, since triangular voids for cloaking such large dimensions are too large to be incorporated into the encapsulant. Moving the triangular void from the encapsulant further away from the inactive area into the cover glass only intensifies this problem.

- **Prismatic covers:** Prismatic covers [56–59] and freeform surface (FFS) cloaks [60] exploit refraction to guide incident light towards the active areas of a solar module via a distinctly curved surface. First prototypes of FFS cloaks exhibit an excellent ability to hide inactive areas and the concept is theoretically applicable to both metallic contact fingers of silicon PV and interconnection lines of thin-film PV [60,63,64]. However, the non-planar surface of FFS cloak is not compatible with the conventional architecture of solar modules, since the groove of the FFS cloak indicated in **Figure 1.2d** is prone to soiling and the accumulation of dirt. To circumvent soiling, conventional solar modules typically feature a planar protective cover glass. A solution to this problem may be the embedment of FFS cloaks into either the polymeric encapsulant or the cover glass as a void. This way, the solar modules maintain a planar front surface. Due to the flexibility in the design of freeform surfaces, FFS cloaks can assume a geometry of dimensions that are compatible with the architecture of commercial solar modules contrary to triangular voids.

This thesis focuses on optical cloaking of inactive areas of solar modules in the context of perovskite/c-Si PV by means of FFS cloaks. In particular, the development of designs of FFS cloaks compatible with the conventional architecture of state-of-the-art solar modules via embedding the FFS into one of the encapsulation layers is pursued. In addition, the establishment of fabrication techniques for durable FFS cloaks that are potentially applicable for large-scale fabrication is targeted. To begin with, the potential improvement in annual power output is studied in detail and compared to other optical loss mechanisms. Subsequently, this thesis develops the basic understanding of the working principle of FFS cloaks that is required to design embedded FFS cloaks. Further optical simulations highlight the impact of embedded FFS cloaks on the performance of solar modules under realistic conditions and discusses how FFS cloaks possibly open up the way to new electrical connection schemes. Moreover, various prototypes of conventional c-Si solar cells, as well as CIGS and perovskite thin-film solar modules, are fabricated and a process to embed FFS cloak into the robust front cover glass is established.

Outline

In Chapter 2, the theoretical background of this thesis is established. The chapter discusses the working principle of PV introduces the device architectures of the PV technologies used in this work. Furthermore, the fundamentals of light propagation in matter are recapitulated. Then, the design principle of FFS cloaks is described mathematically. In Chapter 3, the fundamental simulation methods are described. In addition, this chapter provides a description of the relevant experimental techniques and characterization methods. Chapter 4 discusses the energy yield modelling framework applied in this work with a focus on the optical simulation module, which the author developed within this thesis.

An analysis and quantitative comparison of optical loss mechanisms of perovskite/c-Si tandem solar modules based on optical simulations and energy yield modelling is presented in Chapter 5. Subsequently, the working principle of bare and embedded FFS cloaks is investigated in Chapter 6. Furthermore, the FFS cloaks are analyzed with regard to their impact on solar modules under realistic irradiation conditions. Again, energy yield modelling is applied to quantify the benefit of guiding incident light into active areas via FFS cloaks. In addition, a new contacting scheme for solar modules enabled by FFS cloaks is proposed and discussed. Prototypes of FFS cloaks that effectively guide incident light towards the active area are shown in

Chapter 7. These are applied to CIGS and perovskite thin-film solar modules as well as encapsulated c-Si solar cells, since each PV technology has different requirements with regard to the fabrication techniques of FFS cloaks and the approach to embed them into conventional architecture of the respective solar modules.

Chapter 8 summarizes the results and discusses them in the context of the current literature and developments in the field of PV. Furthermore, the key challenges for a large-scale fabrication of FFS cloaks are outlined.

2 Fundamentals

This chapter provides an overview of the fundamentals of photovoltaic (PV) energy conversion and light interaction with matter. In the first section, the working principle of single-junction and tandem photovoltaics – alongside the investigated PV technologies – is briefly reviewed. The second section introduces the physics of light propagation in matter.

2.1 Photovoltaics

In this section, photovoltaic energy conversion in solar cells is described briefly. For an in-depth description of the theory of solar cells, the basics of photovoltaic energy conversion and semiconductor physics please refer to corresponding textbooks [65,66].

2.1.1 Working principle

Photovoltaic energy conversion relies on the absorption of solar irradiation in a semiconductor. The absorption of a photon induced via the excitation of an electron from one energy state to another creates an electron-hole pair. In semiconductors, the range of possible energy states of electron is interrupted by the bandgap with the energy E_G, which is characteristic for a semiconductor. Consequently, photons have to carry an energy larger than the bandgap with it to be absorbed in the semiconductor as illustrated in **Figure 2.1a**. The energy range above this bandgap is the conduction band and the energy range below is the valence band. Photons with energies smaller than the bandgap cannot be absorbed and simply pass through the semiconductor or are reflected at its interfaces. Electrons excited by a photon with an energy larger than the bandgap relax to the band edge by generating phonons. The energetic distribution or the probability of electrons occupying a state with the energy E_e is described by the Fermi distribution function (see **Figure 2.1b**) with the characteristic Fermi energy E_F, at which exactly half of the states are occupied.

In a solar cell, the absorber is connected to an n-type and a p-type conductor. Usually, the excess of donors is described as n-type and the excess of acceptors as p-type. Together, this architecture forms p-i-n junction. The absorber itself can also be doped, leaving only the simpler case of a p-n junction. Since most of the applied PV technologies investigated in this thesis employ p-i-n junctions, the subsequent review of photovoltaic energy conversion is based on this junction.

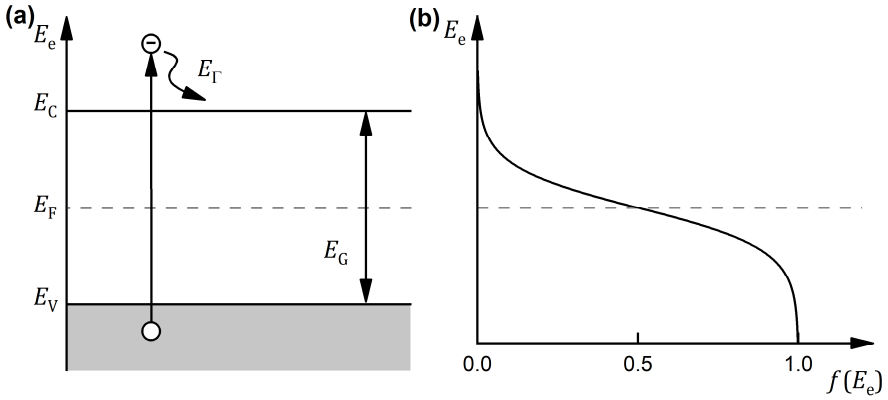

Figure 2.1: (a) Illustration of the electronic band structure of semiconductors with a bandgap (E_G) between the valence band (E_V) and the conduction band (E_C) and (b) the Fermi distribution function, which defines the probability of an electron occupying a state with the energy E_e.

The generated electron-hole pairs are separated and directed towards their corresponding terminals by a gradient in the electrochemical potential, which describes the two forces acting on charges carriers in a p-i-n junction: (1) drift due to a gradient in the electrical energy and (2) diffusion due to an inhomogeneous charge distribution [65]. The electrochemical potentials of electrons and holes are identified by their quasi-Fermi energies $E_{F,n}$ and $E_{F,p}$, which split up in an illuminated solar cell as depicted in **Figure 2.2a**.

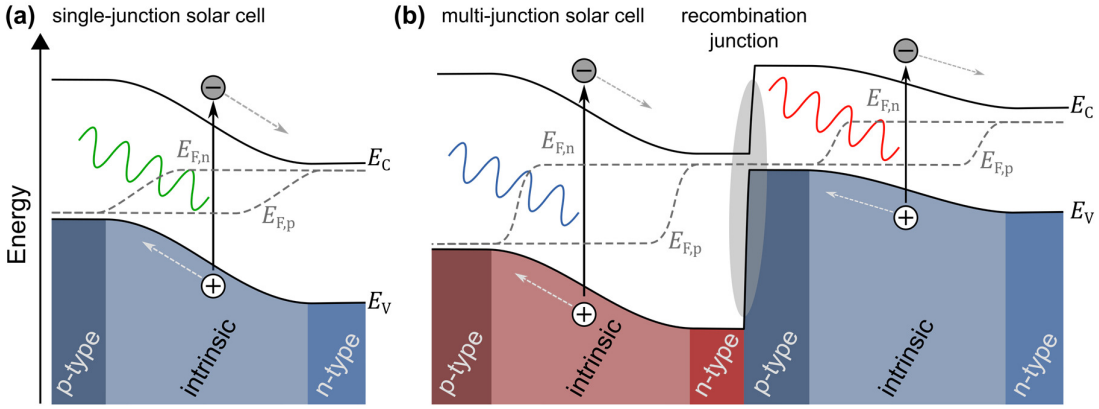

Figure 2.2: Typical band diagram of (a) single-junction solar cell and (b) a monolithic tandem solar cell under illumination at open circuit conditions. Both solar cells exhibit a heterojunction, which is commonly employed in perovskite and c-Si solar cells.

In the monolithic tandem solar cell, a constant charge current is maintained by the recombination of electrons generated in the top-cell and holes originating from the bottom-cell in the recombination junction (see **Figure 2.2b**) that is located in between the two sub-cells.

2.1.2 Solar cell parameters

The performance of solar cells is most commonly identified by two key parameters: (1) the power conversion efficiency (PCE) and (2) the external quantum efficiency (EQE). The former is determined via a measurement of the current density–voltage (J-V) characteristic (see **Figure 2.3**) of the solar cell, which provides information about the maximum power P_{mpp} that is extractable from the device. This measurement is performed under standard test conditions (STC), which involves an ambient temperature of 25°C and an illumination at normal incidence with a global air mass 1.5 (AM1.5G) reference spectrum with an overall intensity of 1000 W/m² [67,68]. The PCE is defined as the ratio of P_{mpp} divided by the incident power P_{in} under STC:

$$\mathrm{PCE} = \frac{P_{\mathrm{mpp}}}{P_{\mathrm{in}}} = \frac{J_{\mathrm{SC}} \cdot V_{\mathrm{OC}} \cdot FF}{P_{\mathrm{in}}}, \qquad (2.1)$$

which can also be expressed in terms of short-circuit current density J_{SC}, open-circuit voltage V_{OC} and the fill factor $FF = P_{\mathrm{mpp}}/(J_{\mathrm{SC}} \cdot V_{\mathrm{OC}})$.

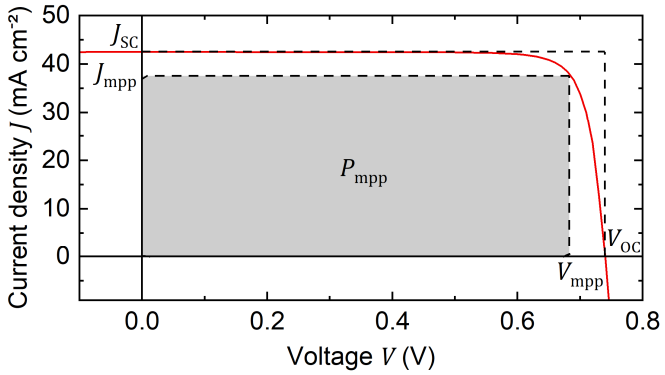

Figure 2.3: Typical J-V characteristic of a crystalline silicon solar cell with the maximum extractable power P_{mpp} indicated by the grey rectangle.

The EQE is a more appropriate figure of merit for the identification of spectrally dependent effects since it refers to the probability of a photon of a specific wavelength to be converted into an extracted charge carrier by a solar cell. It is given by:

$$\mathrm{EQE}(\lambda) = \frac{J_{\mathrm{ph}}(\lambda)}{e \cdot \phi_{\mathrm{p}}(\lambda)}, \tag{2.2}$$

where J_{ph} is the generated photocurrent, e the elemental charge and ϕ_{p} the incoming photon flux. Since usually no voltage is applied during the measurement of the EQE, the integral of the product of EQE and solar spectrum corresponds to the J_{SC}.

Figure 2.4 shows the EQE of a simulated perovskite/c-Si tandem solar cell. The deduction of many important conclusions is possible by analyzing it. One evident feature is, for example, that the perovskite top-cell does not absorb any light below its bandgap at around 800 nm. Furthermore, for wavelength shorter than 500 nm all photons are already absorbed by the perovskite top-cell before even reaching the c-Si bottom cell. Another important spectral region of the EQE is the range above 1000 nm, where the quality of light trapping in the c-Si bottom-cell, which is the ability to trap photons inside the absorber for increased absorption, affects the EQE crucially.

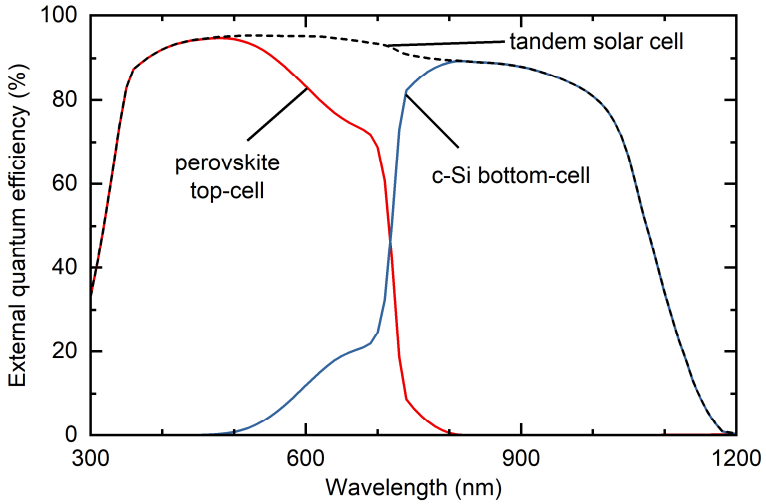

Figure 2.4: Illustration of the EQE of a simulated perovskite/c-Si tandem solar cell. The individual contributions of the perovskite top solar cell (red) and the c-Si bottom solar cell (blue) are indicated.

2.1.3 Device architecture

Owing to the variety of photovoltaic technologies employed in this thesis, this section provides an overview of all relevant architectures and contacting schemes. Firstly, the device architecture of perovskite solar cells commonly exhibits a heterojunction, which consists of an absorber, a n-doped electron transport layer (ETL) and a p-doped hole transport layer (HTL) as indicated in **Figure 2.5a**. This n-i-p junction is fabricated on a glass substrate covered with a transparent conductive oxide (TCO) acting as the front electrode. The architecture is completed with either an Au rear contact for opaque solar cells or another TCO for semitransparent devices [10,69].

One of the major advantages of thin-film PV lies in the possibility to manufacture integrated circuit designs via a monolithic interconnection of a number of individual cell-stripes on large areas. This approach maintains low currents, which go hand in hand with low resistance losses, across an entire module, while it enables modules with higher voltages at the same time. The interconnection consists of three scribing lines

P1, P2 and P3 and connects the rear contact of cell *n* with the front contact of cell *n*+1 [70]. This way, current flows in the lateral direction through all cell stripes.

In c-Si solar cells, the heterojunction architecture is, apart from other architectures, also widespread. The heterojunction, shown in **Figure 2.5b**, is formed by the deposition of selective and passivating contacts consisting of intrinsic as well as n- and p-doped hydrogenated amorphous silicon (*a*-Si:H). A TCO and an Ag layer constitute the rear contact. For the charge transport, a metal grid, which most commonly consists of Ag, covers the front TCO.

Thin-film $CuIn_xGa_{1-x}Se_2$ (CIGS) solar cells are the third PV technology applied in this thesis since they pose a thin-film alternative for the c-Si bottom cell. Additionally, CIGS solar modules were the only monolithically interconnected thin-film technology available at the time of this thesis and thus serve as a guideline for optical cloaking of monolithic interconnections in perovskite solar modules. The core of their architecture, sketched in **Figure 2.5c**, is composed of a p-doped CIGS absorber and an n-doped cadmium sulfide (CdS) buffer. This p-n junction is processed on top of a molybdenum-covered glass substrate. Intrinsic zinc oxide (i-ZnO) and aluminum-doped zinc oxide (ZnO:Al) embody the front electrode. As outlined above, monolithic interconnections replace metallic finger grids for the charge extraction in thin-film PV technology of CIGS.

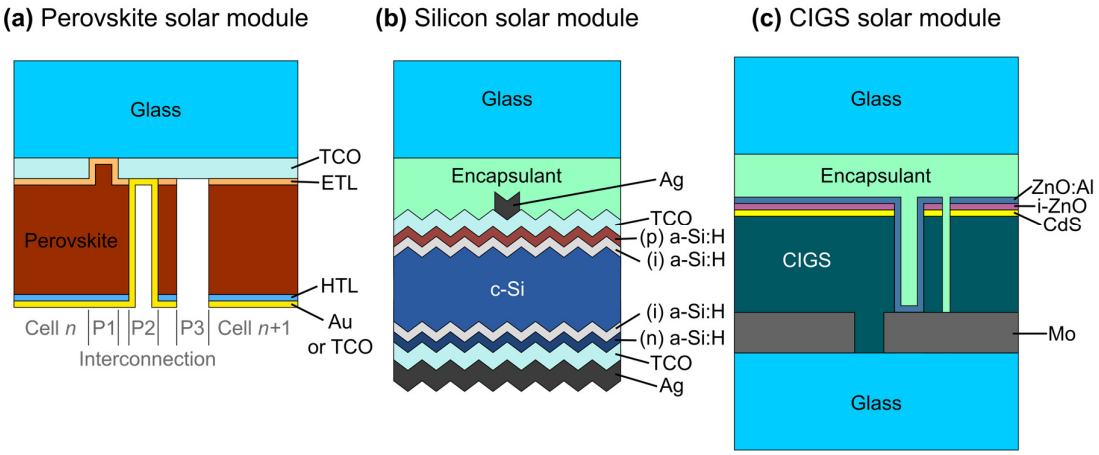

Figure 2.5: Architecture of single-junction (a) perovskite, (b) crystalline silicon and (c) CIGS solar modules. The thin-film PV technologies – perovskite and CIGS – are monolithically interconnected. An identification of the interconnection lines P1, P2 and P3 is provided in (a) and the same applies for (c).

In Chapter 1, it is outlined that the combination of two absorber materials with different bandgaps allows for the creation of tandem solar modules, which exhibit a higher theoretical limit in PCE than the individual PV technologies in isolation. Flat-plate tandem solar modules commonly employ two distinct architectures, which are illustrated in **Figure 2.6**: (1) the monolithically-stacked 2-terminal (2T) architecture and (2) the mechanically-stacked 4-terminal (4T) architecture. The name of the former originates from the fact that it employs only two electrical terminals for the current extraction. In this architecture, generated charge carriers either flow to the two contacts or to the intermediate recombination junction that connects both sub-cells. Owing to this series connection of the top and bottom sub-cells, the lower current density out of both sub-cells limits the maximum extractable current density, which is referred to as current matching. In the 4T configuration, the existence of an insulating, optical spacer the latter enables an individual electrical connection of both sub-cells, which circumvents current matching entirely. The individual connection also entails to integrate the monolithic interconnection the thin-film perovskite top-cell, whereas the 2T configuration relies on the conventional metallic contact grid for lateral charge transport.

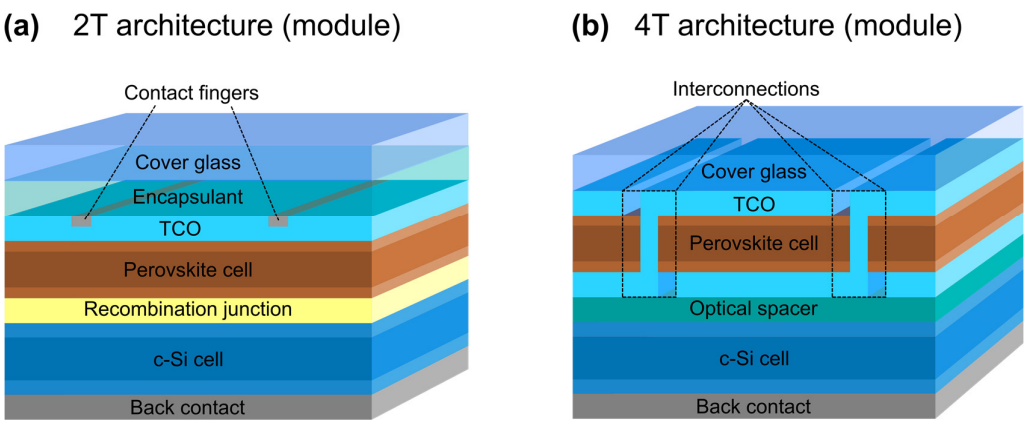

Figure 2.6: Architecture of perovskite/c-Si tandem PV modules in (a) the 2T and (b) the 4T configuration. Depending on the architecture, either metallic contact fingers or monolithic interconnections are employed.

The last feature that distinguishes solar modules optically from solar cells is the module encapsulation. In single-junction c-Si PV, a combination of a polymeric encapsulant and a robust cover glass is the standard. The same encapsulation strategy is compliant with the 2T configuration since the perovskite top-cell is directly processed on top of the c-Si bottom-cell. In contrast, the perovskite top-cell is fabricated separately on glass superstrates for the 4T configuration, which eliminates the need of a polymeric encapsulant to bond the cover glass and the solar cell.

A more detailed evaluation of state-of-the-art perovskite/c-Si tandem solar modules, which discusses the implications of the configurations and architectures on optical losses, material and processing constraints as well as on the power output under realistic conditions, follows in Chapter 5.

2.2 Light propagation in matter

This section outlines the theory of light interaction with matter briefly and is the basis for the methods applied in optical simulations of perovskite/c-Si tandem solar modules that are discussed in Section 4.3.

2.2.1 Electrodynamics

In 1865, James Clerk Maxwell laid the foundation for today's understanding of electromagnetics with a set of partial differential Equations [71,72]. These so-called Maxwell's Equations describe the temporal and spatial evolution of two vectorial fields: (1) the electric field $\boldsymbol{E}(\boldsymbol{r},t)$ and (2) the magnetic field $\boldsymbol{H}(\boldsymbol{r},t)$. Maxwell's Equations in homogeneous, isotropic materials from a macroscopic point of view are:

$$\boldsymbol{\nabla} \times \boldsymbol{H}(\boldsymbol{r},t) = \frac{\partial \boldsymbol{D}(\boldsymbol{r},t)}{\partial t} + \boldsymbol{J}_{\mathrm{f}}(\boldsymbol{r},t), \qquad \text{(Ampére's circuital law)} \qquad (2.3)$$

$$\boldsymbol{\nabla} \times \boldsymbol{E}(\boldsymbol{r},t) = -\frac{\partial \boldsymbol{B}(\boldsymbol{r},t)}{\partial t}, \qquad \text{(Faraday's law of induction)} \qquad (2.4)$$

$$\boldsymbol{\nabla} \cdot \boldsymbol{B}(\boldsymbol{r},t) = 0, \qquad \text{(Gauss' law for magnetism)} \qquad (2.5)$$

$$\boldsymbol{\nabla} \cdot \boldsymbol{D}(\boldsymbol{r},t) = \rho_{\mathrm{f}}(\boldsymbol{r},t), \qquad \text{(Gauss' law)} \qquad (2.6)$$

where $\boldsymbol{D}(\boldsymbol{r},t)$ is the dielectric displacement, $\boldsymbol{B}(\boldsymbol{r},t)$ the magnetic induction, $\boldsymbol{J}_{\mathrm{f}}(\boldsymbol{r},t)$ the free electric current density and $\rho_{\mathrm{f}}(\boldsymbol{r},t)$ the free charge density. In isotropic media with a linear response to external fields, Maxwell's Equations are complement by constitutive relations:

$$\overline{\boldsymbol{D}}(\boldsymbol{r},\omega) = \varepsilon_0 \varepsilon_{\mathrm{r}}(\boldsymbol{r},\omega)\overline{\boldsymbol{E}}(\boldsymbol{r},\omega), \tag{2.7}$$

$$\overline{\boldsymbol{B}}(\boldsymbol{r},\omega) = \mu_0 \mu_{\mathrm{r}}(\boldsymbol{r},\omega)\overline{\boldsymbol{H}}(\boldsymbol{r},\omega), \tag{2.8}$$

$$\overline{\boldsymbol{J}}_{\mathrm{f}}(\boldsymbol{r},\omega) = \sigma(\boldsymbol{r},\omega)\overline{\boldsymbol{E}}(\boldsymbol{r},\omega), \tag{2.9}$$

where $\overline{\boldsymbol{E}}(\boldsymbol{r},\omega) = \frac{1}{2\pi}\int_{-\infty}^{+\infty} \boldsymbol{E}(\boldsymbol{r},t)e^{i\omega t}dt$ is the Fourier transform of the electric field $\boldsymbol{E}(\boldsymbol{r},t)$ in the time domain and ω the angular frequency of a specific wave. The same correlation applies to $\overline{\boldsymbol{D}}(\boldsymbol{r},\omega)$, $\overline{\boldsymbol{B}}(\boldsymbol{r},\omega)$, $\overline{\boldsymbol{H}}(\boldsymbol{r},\omega)$ and $\overline{\boldsymbol{J}}_{\mathrm{f}}(\boldsymbol{r},\omega)$. Additionally, ε_0 is the vacuum permittivity, $\varepsilon_{\mathrm{r}}(\boldsymbol{r},\omega)$ the dielectric function, μ_0 the vacuum permeability and $\mu_{\mathrm{r}}(\boldsymbol{r},\omega)$ the frequency-dependent relative permeability, while $\sigma(\boldsymbol{r},\omega)$ denotes the electrical conductivity.

In non-magnetic ($\mu_r = 1$) and lossless homogeneous media ($\varepsilon_{\mathrm{r}}(\boldsymbol{r},\omega) = \varepsilon_{\mathrm{r}}(\omega) = \Re\{\varepsilon_{\mathrm{r}}(\omega)\}$) without free charges ($\rho_{\mathrm{f}}(\boldsymbol{r},t) = 0$) and without free current density ($\boldsymbol{J}_{\mathrm{f}}(\boldsymbol{r},t) = 0$), Maxwell's equations can be transformed into the Helmholtz wave equations:

$$\Delta\overline{\boldsymbol{E}}(\boldsymbol{r},\omega) + \frac{\omega^2}{c^2}\varepsilon_{\mathrm{r}}(\omega)\overline{\boldsymbol{E}}(\boldsymbol{r},\omega) = 0, \tag{2.10}$$

$$\Delta\overline{\boldsymbol{H}}(\boldsymbol{r},\omega) + \frac{\omega^2}{c^2}\varepsilon_{\mathrm{r}}(\omega)\overline{\boldsymbol{H}}(\boldsymbol{r},\omega) = 0. \tag{2.11}$$

The general solution of these Helmholtz Equations is a linear superposition of plane waves:

$$\overline{\boldsymbol{E}}(\boldsymbol{r},\omega) = \boldsymbol{e}(\boldsymbol{k},\omega)\mathrm{e}^{i\boldsymbol{k}\cdot\boldsymbol{r}}, \tag{2.12}$$

$$\overline{\boldsymbol{H}}(\boldsymbol{r},\omega) = \boldsymbol{h}(\boldsymbol{k},\omega)\mathrm{e}^{i\boldsymbol{k}\cdot\boldsymbol{r}}, \tag{2.13}$$

where $\boldsymbol{e}$ and $\boldsymbol{h}$ are the amplitudes of the plane waves and $\boldsymbol{k}$ is the corresponding wave vector. Considering only waves travelling in one direction, the solution of the electric and magnetic fields is then:

$$\boldsymbol{E}(\boldsymbol{r},t) = \Re\left\{\int_{-\infty}^{+\infty} \boldsymbol{e}(\boldsymbol{k},\omega)\mathrm{e}^{i(\boldsymbol{k}\cdot\boldsymbol{r}-\omega t)}d\omega\right\}, \tag{2.14}$$

$$\boldsymbol{H}(\boldsymbol{r},t) = \Re\left\{\int_{-\infty}^{+\infty} \boldsymbol{h}(\boldsymbol{k},\omega)\mathrm{e}^{i(\boldsymbol{k}\cdot\boldsymbol{r}-\omega t)}d\omega\right\}. \tag{2.15}$$

The wave vector $\boldsymbol{k}$ correlates to the complex refractive index $\tilde{n}$ according to the dispersion relation:

$$k = |\boldsymbol{k}| = \omega|\tilde{n}|/c \tag{2.16}$$

It is evident from the dispersion relation that a complex refractive index $\tilde{n} = \sqrt{\varepsilon_{\mathrm{r}}} = n + i\cdot\kappa$ with a non-vanishing imaginary part, the extinction coefficient κ, leads to an attenuation of the intensity $I(d)$ of the propagating electromagnetic waves according to the Beer-Lambert law [73]:

$$I(d) = I_0 e^{-\alpha d} = I_0 e^{-\frac{4\pi\kappa}{\lambda}d}, \tag{2.17}$$

where $\alpha = -4\pi\kappa/\lambda$ is the absorption coefficient.

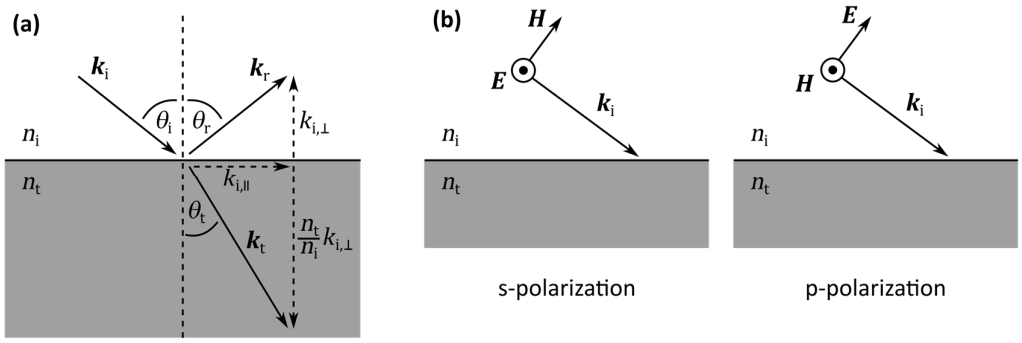

Figure 2.7: (a) Schematic of the propagation of light at an interface between two dielectrics with the refractive indices n_i and n_t. (b) Illustration of the orientation of the electric field $\boldsymbol{E}$ and the magnetic field $\boldsymbol{H}$ with regard to the interface between the two dielectrica.

Beyond the propagation and absorption of light inside a single media, interfaces between two dielectrics with different refractive indices, n_i and n_t, reflect and refract light at such interfaces as illustrated in **Figure 2.7a**. The direction of the wave vectors of the reflected wave $\boldsymbol{k}_\mathrm{r}$ and the transmitted wave $\boldsymbol{k}_\mathrm{t}$ are well described via Snell's law [73], which states that the components of the wave vector parallel to the interface of an incident wave remains constant under reflection and transmission. Mathematically, this is tantamount with:

$$n_\mathrm{i} \sin\theta_\mathrm{i} = n_\mathrm{t} \sin\theta_\mathrm{t}\,, \tag{2.18}$$

where θ_i and θ_t are the propagation angles of the incident and transmitted wave. Because of this relation, the propagation angle of the reflected wave θ_r and the incident angle θ_i are the same since the reflected wave stays within the starting medium.

It is apparent that the wave somehow splits at an interface but this splitting only affects the amplitude of the waves. The amplitudes of the reflected and transmitted wave are linked to the one of the incident wave via the amplitude reflection and transmission coefficients, $r_\mathrm{s,p}$ and $t_\mathrm{s,p}$, according to Fresnel's Equations [73]:

$$r_\mathrm{s} = \frac{n_\mathrm{i}\cos\theta_\mathrm{i} - n_\mathrm{t}\cos\theta_\mathrm{t}}{n_\mathrm{i}\cos\theta_\mathrm{i} + n_\mathrm{t}\cos\theta_\mathrm{t}} \quad , \quad r_\mathrm{p} = \frac{n_\mathrm{t}\cos\theta_\mathrm{i} - n_\mathrm{i}\cos\theta_\mathrm{t}}{n_\mathrm{t}\cos\theta_\mathrm{i} + n_\mathrm{i}\cos\theta_\mathrm{t}} \tag{2.19}$$

$$t_\mathrm{s} = \frac{2n_\mathrm{i}\cos\theta_\mathrm{i}}{n_\mathrm{i}\cos\theta_\mathrm{i} + n_\mathrm{t}\cos\theta_\mathrm{t}} \quad , \quad t_\mathrm{p} = \frac{2n_\mathrm{i}\cos\theta_\mathrm{i}}{n_\mathrm{t}\cos\theta_\mathrm{i} + n_\mathrm{i}\cos\theta_\mathrm{t}} \tag{2.20}$$

Since the orthogonal electric and magnetic field may have various orientations with regard to the interface, the amplitude of transmitted and reflected waves depend on it. The extreme cases, illustrated in **Figure 2.7b**, are s-polarization, in which the electric field is parallel to interface, and p-polarization, where the magnetic field points parallel to the interface. All orientations in between these extreme cases are linear superpositions of both cases. The observable quantities at such an interfaces are on the one hand the reflectivity R:

$$R_\mathrm{s,p} = \left|r_\mathrm{s,p}\right|^2\,, \tag{2.21}$$

and on the other hand the transmittivity T:

s-polarization:
$$T = \frac{\Re[\tilde{n}_\mathrm{t} \cos \theta_\mathrm{t}]}{\Re[\tilde{n}_\mathrm{i} \cos \theta_\mathrm{i}]} |t|^2, \qquad (2.22)$$

p-polarization:
$$T = \frac{\Re[\tilde{n}_\mathrm{t} \cos \theta_\mathrm{t}^*]}{\Re[\tilde{n}_\mathrm{i} \cos \theta_\mathrm{i}^*]} |t|^2. \qquad (2.23)$$

They link the intensities of the transmitted and reflected wave to the intensity of the incident wave rather than the respective amplitudes.

2.2.2 Thin-film interference

Propagating electromagnetic plane waves spontaneously change their phase after a certain amount of time τ and thus the superposition of multiple plane waves loses its phase correlation. If, however, the thickness of a medium is smaller than the distance the wave can travel during τ, the so-called coherence length l, the phase correlation of electromagnetic waves results in the appearance of interference [73]. Therefore, this interference is also often referred to as thin-film interference.

In **Figure 2.8**, the mechanism of thin-film interference is illustrated. Let us imagine a layer stack consisting of three media with the refractive indices n_1, n_2 and n_3. Light hitting the first interface at position A splits into a reflected and a transmitted part. If the transmitted part is subsequently also reflected at the next interface at position B, the reflected light is then partially transmitted back into the starting medium. Here, the light reflected at the second interface acquired a certain phase while travelling through the thin film. Consequently, the reflected light from the first and the second interface may well be out of phase. Thus, their superposition leads to maxima and minima of the overall field amplitudes and interference patterns arise. The consideration of this phenomena is therefore of vital importance for the calculation of light propagation in thin-film multi-layer stacks.

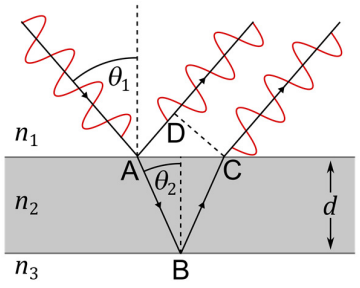

Figure 2.8: Illustration of constructive interference of reflected light at a thin film with the refractive index n_2.

2.3 Design of freeform surface cloaks

The design of smooth freeform surface cloaks was developed by Schumann *et al.* [60]. In the following, the derivation of the height profile is briefly recapitulated according to Ref. [60] and its Supporting Information with the addition of some corrections that are mentioned later on.

As illustrated in **Figure 2.9**, the design of a smooth freeform surface relies on a one-dimensional coordinate transformation of the coordinates x that are located in the interval $[0, R_2]$ onto a smaller interval $[R_1, R_2]$ with the transformed coordinates x'. This transformation mathematically represents the design goal of hindering photons to hit the inactive area in the region $|x| \leq R_1$ and guiding them into the region $[R_1, R_2]$ with a homogeneous spatial distribution. This is achieved via refraction of light at the surface of the cloak.

Due to the reflection symmetry of the targeted freeform surface, the coordinate transformation in the negative x-range is a mirror image of the positive x-range.

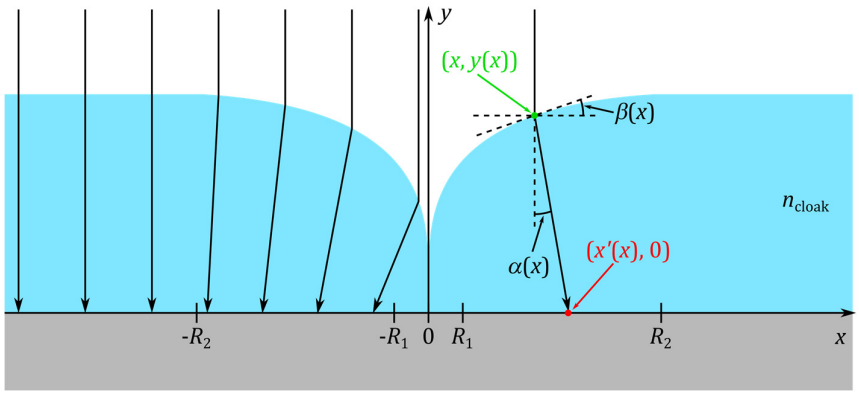

Figure 2.9: Illustration of the one-dimensional linear coordinate transformation $x \rightarrow x'$, which maps the coordinates of the interval $[0, R_2]$ onto a new interval $[R_1, R_2]$. The resulting angular distribution $\alpha(x)$ is obtained via a smooth freeform surface with the height profile $y(x)$, where $\beta(x)$ indicates the local inclination angle of the freeform surface.

Following the transformation for the axial component of the cloaking transformation from a point to a circle by Pendry *et al.* [74], the one-dimensional linear coordinate transformation for $x \geq 0$ can be written as:

$$x' = \frac{R_2 - R_1}{R_2} x + R_1. \tag{2.24}$$

In the range $|x| > R_2$ applies $x' = x$. The coordinates of the height profile $\big(x, y(x)\big)$ are connected to the targeted hit location in the active area $(x', 0)$ via the angle $\alpha(x)$:

$$\tan(\alpha) = \frac{x'(x) - x}{y(x)}, \tag{2.25}$$

as illustrated in **Figure 2.9**. Substituting x' in Equation (2.25) by Equation (2.24) results in:

$$\tan\big(\alpha(x)\big) = \frac{R_1}{y(x)}\left(1 - \frac{x}{R_2}\right), \tag{2.26}$$

which is in contrast to the results reported in the Supporting Information of Ref. [60]. There, $\alpha(x)$ is mistakenly confused with the local surface inclination angle $\beta(x)$. This local inclinate angle $\beta = \arctan(dy/dx)$ leads to the correlation of the height y at point x with the height y_0 at point 0 and the inclination profile $\beta(x)$:

$$y(x) = y_0 + \int_0^x \tan\big(\beta(\tilde{x})\big)\, d\tilde{x}. \tag{2.27}$$

Inserting Equation (2.27) into Equation (2.26) results in a nonlinear differential equation for $\beta(x)$:

$$\frac{R_1\left(1 - \frac{x}{R_2}\right)}{\tan\left(\beta(x) - \arcsin\left(\frac{\sin\big(\beta(x)\big)}{n_{\text{cloak}}}\right)\right)} - y_0 = \int_0^x \tan\big(\beta(\tilde{x})\big)\, d\tilde{x}. \tag{2.28}$$

This Equation can be solved numerically by discretizing the integral on the right side into equidistant intervals of the size Δx and splitting it recursively according to:

$$I_i = I_{i-1} + \int_{x_{i-1}}^{x_i} \tan\big(\beta(\tilde{x})\big)\, d\tilde{x} \approx I_{i-1} + \tan\big(\beta(x_{i-1})\big) \cdot \Delta x, \tag{2.29}$$

with:

$$I_i = \int_{0}^{x_i} \tan\big(\beta(\tilde{x})\big)\, d\tilde{x}. \tag{2.30}$$

The discretized height profile $y(x_i) = y_0 + I_i$ can thus be calculated iteratively starting from $x = 0$, for which the integral on the right side of Equation (2.28) vanishes.

The choice of the three parameters R_1, R_2 and y_0 underlies some constraints. Firstly, the cloaked region R_1 must be larger than the width w of the inactive area but smaller than half the spacing in between two adjacent inactive areas $w/2f$, where f denotes the GFF of inactive areas:

$$\frac{R_1}{w} \in \left[\frac{1}{2}, \frac{1}{2f}\right]. \tag{2.31}$$

Furthermore, the upper limit also applies to the lateral extent of the FFS cloak R_2. The lower limit is defined by R_1 itself [60]:

$$\frac{R_2}{w} \in \left[\frac{R_1}{w}, \frac{1}{2f}\right]. \tag{2.32}$$

Lastly, the minimum distance between the FFS cloak and the inactive area is constraint by the fact the inclination angle $\beta(x)$ must always be smaller than 90°, in particular at $x = 0$. By transforming Equation (2.28) at this point with $\beta(0) = 90°$, a lower limit for $y(0)$ can be obtained:

$$\frac{y_0}{R_1} \geq \left[\tan\left(90° - \arcsin\left(\frac{1}{n_{\text{cloak}}}\right)\right)\right]^{-1}. \tag{2.33}$$

For perpendicular incidence of light, an upper limit for $y(0)$ is obsolete. Simulations of the average annual improvement performed by Schumann *et al.* indicate an optimum when R_2 is maximal while R_1 and $y(0)$ are minimal [60]:

$$\frac{R_1}{w} = \frac{1}{2}, \tag{2.34}$$

$$\frac{R_2}{w} = \frac{1}{2f}, \tag{2.35}$$

$$\frac{y_0}{w} = \frac{1}{2}\left[\tan\left(90 - \arcsin\left(\frac{1}{n}\right)\right)\right]^{-1} \approx 0.45. \tag{2.36}$$

3 Methods

This section describes all applied methods for optical simulations of light propagation in matter, the techniques used for the fabrication of the investigated optical concept, namely freeform surface cloaks. Furthermore, the experimental methods used to characterize prototypes with cloaked contact fingers and interconnection lines of solar cells are briefly outlined.

3.1 Fundamental optical simulation methods

The optical simulations for energy yield modelling performed in this thesis rely on various simulation methods, which are combined and intertwined for the simulation of the complex architectures of perovskite-based tandem solar modules. For the optical simulation of freeform surfaces, rigorous raytracing is applied. This section thus focuses exclusively on the basic simulation methods: (1) the transfer-matrix method (TMM), (2) the Beer-Lambert law, (3) geometrical raytracing and (4) rigorous raytracing. The methodology of optical simulations of perovskite-based tandem solar modules is provided in the Section 4.3 on the methodology of energy modelling of perovskite-based tandem solar modules.

3.1.1 Incoherent "optically-thick" layers: Beer-Lambert law

In layers with a thickness significantly larger than the wavelength, planar waves do not interfere with each other since they lose their phase correlation after travelling a certain distance through a single medium. The loss of phase correlation originates from the fact that propagating waves can be described as planar waves with a distinct phase correlation only for a certain amount of time or distance since spontaneous changes in phase occur [73]. This distance is often referred to as the coherence length of light. For layer thicknesses significantly larger than the coherence length, absorption of light is sufficiently described by the Beer-Lambert law:

$$I(d,\lambda) = I_0 \cdot e^{-\alpha(\lambda)\cdot d}, \tag{3.1}$$

where I_0 is the intensity at the starting position and $I(d,\lambda)$ is the intensity after passing the distance d. It states that the propagating intensity declines exponentially with the distance d travelled inside a medium depending on its absorption coefficient α.

3.1.2 Multi-layer thin-film stacks: the transfer-matrix method

The wave characteristic of light, outlined in Section 2.2.1, becomes especially noticeable in multi-layer thin-film layer stacks with layer thicknesses in the same range as the wavelength of propagating light. Interference patterns appear by the superposition of forward and backward moving plane waves generated by multiple reflections at the many interfaces present in a multi-layer stack as illustrated in **Figure 3.1**. The TMM provides a simple formalism to calculate the light propagation in such multi-layer stacks by relating the amplitudes of the electric field at different positions in the stack via a product of 2 x 2 matrices [75,76].

When considering incoming waves from both sides of a single interface between the media n and $n+1$, the amplitudes of the outgoing waves E'_n and E'^{+}_{n+1} are a superposition of the amplitude of the reflected wave in this medium ($E^{+}_n\ r_{n,n+1}$ and $E'^{-}_{n+1}\ r_{n+1,n}$) and the amplitude of the wave transmitted from the second medium ($E'^{-}_{n+1} t_{n+1,n}$ and $E^{+}_n t_{n,n+1}$):

$$E'^{+}_{n+1} = E^{+}_n t_{n,n+1} + E'^{-}_{n+1} r_{n+1,n} \tag{3.2}$$

and

$$E^{-}_n = E'^{-}_{n+1} t_{n+1,n} + E^{+}_n r_{n,n+1}\,. \tag{3.3}$$

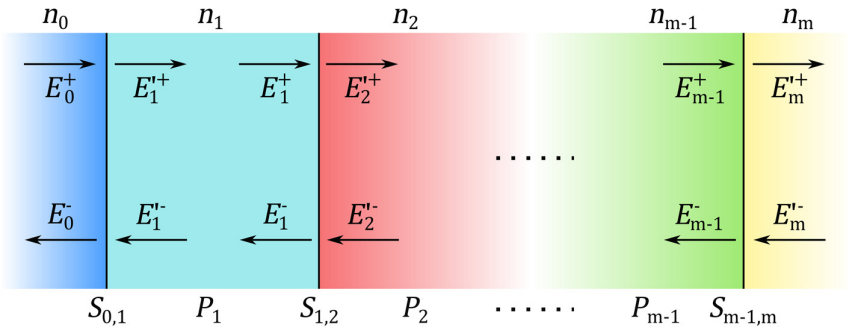

Figure 3.1: Schematic of the principle of the transfer-matrix method for the calculation of propagating electromagnetic waves with the amplitudes E_i in a multi-layer thin-film stack with the refractive indices n_i.

Applying the identities $r_{n,n+1} = -r_{n+1,n}$ and $t_{n,n+1}t_{n+1,n} - r_{n,n+1}r_{n+1,n} = 1$, which result from Equations (2.19) and (2.20), these Equations can be written as:

$$\begin{aligned}\begin{pmatrix} E_n^+ \\ E_n^- \end{pmatrix} &= \boldsymbol{D}_{n,n+1}\begin{pmatrix} E_{n+1}'^+ \\ E_{n+1}'^- \end{pmatrix} \\ &= \frac{1}{t_{n,n+1}}\begin{bmatrix} 1 & r_{n,n+1} \\ r_{n,n+1} & 1 \end{bmatrix}\begin{pmatrix} E_{n+1}'^+ \\ E_{n+1}'^- \end{pmatrix}.\end{aligned} \tag{3.4}$$

The interface matrix $\boldsymbol{D}_{n,n+1}$ thus describes the reflection and transmission occurring at this interface and links the corresponding amplitudes of both the electric field just before and just behind the interface. The field amplitudes at the start and at the end of the n-th layer are connected by the propagation matrix $\boldsymbol{P}_n$:

$$\begin{aligned}\begin{pmatrix} E_n'^+ \\ E_n'^- \end{pmatrix} &= \boldsymbol{P}_n\begin{pmatrix} E_n^+ \\ E_n^- \end{pmatrix} \\ &= \begin{bmatrix} \exp(-i\delta_n) & 0 \\ 0 & \exp(i\delta_n) \end{bmatrix}\begin{pmatrix} E_n^+ \\ E_n^- \end{pmatrix},\end{aligned} \tag{3.5}$$

where $\delta_n = \frac{2\pi\tilde{n}_n d_n}{\lambda}$ is the phase accumulated by passing through the n-th layer. Given a non-zero imaginary part of the complex refractive index $\tilde{n}$, $\boldsymbol{P}_n$ describes the absorption of propagating light. By iteratively multiplying the 2 x 2 propagation and interface matrices, the TMM pursues the path of light and consequently links the field amplitudes in the starting and end media according to:

$$\begin{aligned}\begin{pmatrix} E_0^+ \\ E_0^- \end{pmatrix} &= \boldsymbol{D}_{0,1}\prod_{n=1}^{N}\boldsymbol{P}_n\boldsymbol{D}_{n,n+1}\begin{pmatrix} E_{N+1}'^+ \\ E_{N+1}'^- \end{pmatrix} \\ &= \boldsymbol{M}\begin{pmatrix} E_{N+1}'^+ \\ E_{N+1}'^- \end{pmatrix}.\end{aligned} \tag{3.6}$$

This Equation needs to fulfill the following boundary condition:

$$\begin{aligned}\begin{pmatrix} 1 \\ r \end{pmatrix} &= \boldsymbol{M}\begin{pmatrix} t \\ 0 \end{pmatrix} \\ &= \begin{bmatrix} M_{00} & M_{01} \\ M_{10} & M_{11} \end{bmatrix}\begin{pmatrix} t \\ 0 \end{pmatrix}.\end{aligned} \tag{3.7}$$

This Equation states that there is no light source in the end medium and thus no backward running wave in it ($E_{N+1}'^- = 0$). Furthermore, the amplitude of the incoming wave in the starting medium E_0^+ is unity and the amplitude of the reflected wave E_0^- and the transmitted wave $E_{N+1}'^+$ are the amplitude reflection and

transmission coefficients, r and t, of the entire stack. These can then be expressed in terms of the matrix elements of $\boldsymbol{M}$:

$$t = 1/M_{00} \quad , \quad r = M_{10}/M_{00}\,. \tag{3.8}$$

The overall transmittance T and reflectance R are correlated to the amplitude coefficients according to Fresnel's Equations (2.21) - (2.23). Via these Equations, the TMM also considers the polarization of incident light. Unpolarized light is considered as a superposition of p-polarized and s-polarized light.

The last parameter of relevance is the absorptance A in each individual layer. The subtraction of the net power flowing through both interfaces of the n-th layer allows the calculation of its absorptance. The net power flux at a given position in the multi-layer stack is mathematically represented by the normal component of the time-averaged Poynting vector $\langle \boldsymbol{S}_n \rangle_T \cdot \hat{\mathbf{z}}$ [76]. For the s-polarization, we obtain the following:

$$\begin{aligned} \boldsymbol{E}_n &= E_n^+ \hat{\mathbf{y}} + E_n^- \hat{\mathbf{y}} \\ \boldsymbol{H}_n &\propto \tilde{n} E_n^+ (-\cos\theta\, \hat{\mathbf{x}} + \sin\theta\, \hat{\mathbf{z}}) + \tilde{n} E_n^- (\cos\theta\, \hat{\mathbf{x}} + \sin\theta\, \hat{\mathbf{z}}) \\ \langle \boldsymbol{S}_n \rangle_T \cdot \hat{\mathbf{z}} &= \frac{1}{2} \mathrm{Re}[\hat{\mathbf{z}} \cdot (\boldsymbol{E}^* \times \boldsymbol{H})] \propto \mathrm{Re}\left[\left(E_n^{+^*} + E_n^{-^*} \right) (E_n^+ - E_n^-) \tilde{n} \cos\theta \right] \end{aligned} \tag{3.9}$$

For reasons of simplicity, the normal component of the Poynting vector is normalized to the total incident power $E_0^+ = 1$ and $E_0^- = 0$:

$$\langle \boldsymbol{S}_n \rangle_T \cdot \hat{\mathbf{z}} = \frac{\mathrm{Re}\left[\left(E_n^{+^*} + E_n^{-^*} \right) (E_n^+ - E_n^-) \tilde{n} \cos\theta \right]}{\mathrm{Re}[\tilde{n}_0 \cos\theta_0]}\,. \tag{3.10}$$

Analogue, for p-polarization:

$$\begin{aligned} \boldsymbol{E}_n &= E_n^+ (\cos\theta\, \hat{\mathbf{x}} - \sin\theta\, \hat{\mathbf{z}}) + E_n^- (-\cos\theta\, \hat{\mathbf{x}} - \sin\theta\, \hat{\mathbf{z}}) \\ \boldsymbol{H}_n &\propto \tilde{n} E_n^+ \hat{\mathbf{y}} + \tilde{n} E_n^- \hat{\mathbf{y}} \\ \langle \boldsymbol{S}_n \rangle_T \cdot \hat{\mathbf{z}} &= \frac{1}{2} \mathrm{Re}[\hat{\mathbf{z}} \cdot (\boldsymbol{E}^* \times \boldsymbol{H})] \propto \mathrm{Re}\left[\left(E_n^{+^*} - E_n^{-^*} \right) (E_n^+ + E_n^-) \tilde{n} \cos\theta^* \right]. \end{aligned} \tag{3.11}$$

In the same way as for s-polarization, $\langle \boldsymbol{S} \rangle_T \cdot \hat{\mathbf{z}}$ is normalized to the total incident power:

$$\langle \boldsymbol{S}_n \rangle_T \cdot \hat{\mathbf{z}} = \frac{\mathrm{Re}\left[\left(E_n^{+^*} - E_n^{-^*} \right) (E_n^+ + E_n^-) \tilde{n} \cos\theta^* \right]}{\mathrm{Re}[\tilde{n}_0 \cos\theta_0^*]}\,. \tag{3.12}$$

The absorption in the n-th layer is then nothing else then a mere subtraction of the Poynting vectors at the beginning of two adjacent layers:

$$A_n = \langle \boldsymbol{S}_n \rangle_T \cdot \hat{\mathbf{z}} - \langle \boldsymbol{S}_{n+1} \rangle_T \cdot \hat{\mathbf{z}}\,. \tag{3.13}$$

Finally, all relevant parameters of the optical performance of a thin-film multi-layer stack are obtained using the TMM.

3.1.3 Pyramidal textures: geometrical raytracing

The high degree of symmetry of microscopic, pyramidal textures allows the application of geometrical raytracing as proposed by Baker-Finch and McIntosh [77]. Geometrical raytracing is a simple approach that exploits geometrical principles of pyramidal textures and enables the rapid calculation of their impact on the overall reflectance of an interface. Due to the high symmetry of pyramids, incoming light propagates along a very limited number N of precisely predictable paths through these textures as illustrated in **Figure 3.2** for (a) regular upright and (b) inverted pyramids.

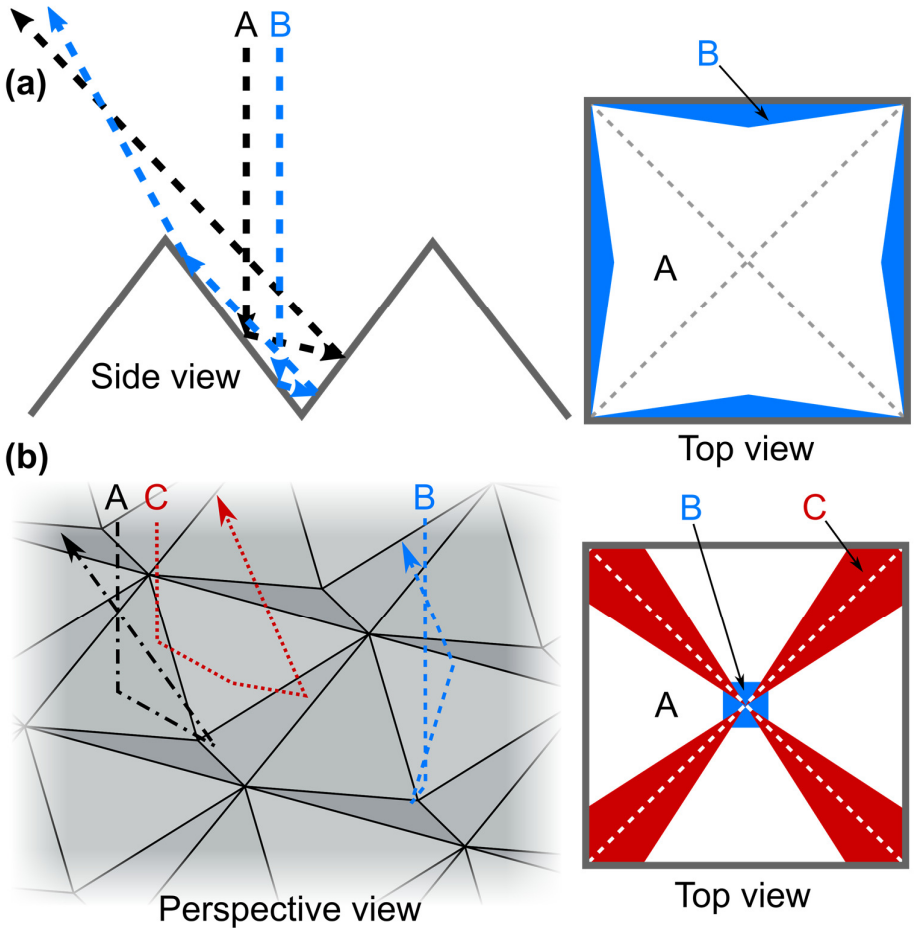

Figure 3.2: Illustration of the principle of geometrical raytracing. Depending on the location that an incident ray hits inside the pyramidal texture, only a characteristic path (A, B or C) is possible. For regular upright pyramids (a) and inverted pyramids (b), the corresponding areas at normal incidence are shown schematically.

The overall reflectance R is then given by the summation of the reflectance along all characteristic paths:

$$R = \sum_{i=1}^{N} p_i R_i \ , \tag{3.14}$$

where p_i is the probability and R_i the reflectance of path i. If the textured interface is covered with one or more thin films, the TMM, outlined in Section 3.1.1, needs to be applied to calculate the reflectance R_i for all intersections along each individual path. Otherwise, the calculation according to the Fresnel Equations (see Equations (2.19) and (2.20) in Section 2.2.1) suffices. The determination of the overall transmittance T follows the same considerations:

$$T = \sum_{i=1}^{N} p_i T_i \ , \tag{3.15}$$

Representative for other textures, the characteristic paths A, B and C of inverted pyramids at normal incidence illustrated in **Figure 3.2b**. The path data for inverted, regular upright and random upright pyramids used in this thesis are extracted from the optical simulator OPAL 2 [78,79]. An extract of this data for normal incidence is provided in **Table 3.1**. Furthermore, it needs to be pointed out that light travelling through pyramidal textures is assumed to be always fully unpolarized and polarization due to reflection proposed by Yun *et al.* [80] is not considered.

While the determination of the characteristic paths of inverted and regular upright pyramids follows this basic geometrical analysis, random upright pyramids rely on geometrical raytracing [77]. This computational method considers a series of adjacent pyramids that feature a random height and are randomly displaced with regard to each other in vertical and horizontal direction. Nonetheless, even these random textures only allow a limited set of characteristic paths, which limits the overall computational effort for the simulation of textured perovskite-silicon tandem solar modules.

Table 3.1: Characteristic paths of light impinging on an inverted pyramidal texture at normal incidence, which are characterized by a distinct number of intersections and an exit angle.

Path	Path probability p_i	Angle of intersection (°)			Exit angle (°)
		1	2	3	
A	0.5924	54.7	15.8	-	39.0
B	0.4001	54.7	78.9	33.5	31.6
C	0.0075	54.7	15.8	86.3	31.6

3.1.4 Freeform surface cloaks: raytracing

For more advanced features with a significantly lower degree of symmetry, rigorous raytracing needs to be applied. This technique emits a certain amount of rays with an adequate resolution of their spatial distribution. Each ray has two specific attributes: (1) a wave vector and (2) an intensity. In homogeneous media, light propagates in the direction of its wave vector and is absorbed according to the Beer-Lambert law in Equation (3.1). At an interface, light rays split up into a reflected and transmitted ray. The direction of the latter is given by Snell's law in Equation (2.18) and the intensities of reflected and transmitted rays are calculated based on the Fresnel Equations (2.19) and (2.20). Each ray is traced until its intensity falls below a threshold of 0.1 % of the incident intensity.

3.2 Fabrication of freeform surface cloaks

The available fabrication techniques for FFS cloaks is limited quite considerably since the distinct dimension and geometry of FFS cloaks covers microscopic to macroscopic feature dimensions. On the one hand, the center of the FFS cloak features a delicate notch or tip, depending on whether the positive or negative of the structure is considered. For perfect cloaking, this notch or tip ideally would display a vanishing width. Additionally, the defined curvature profile of the FFS cloak requires a fabrication technique that can be controlled on a microscopic level. On the other hand, FFS cloaks need to cover the entire length of inactive areas that are present on conventional PV devices, where metallic contact fingers may stretch across entire

silicon wafers or interconnection lines across an entire thin-film solar module. For the first demonstration of FFS cloaks in PV, direct laser writing (DLW) is the fabrication technique of choice since it enables rapid prototyping of almost any desired geometry in the required dimensional range [81] and was already used successfully to fabricate the first FFS cloaks for PV applications [60,64].

3.2.1 Direct laser writing

Direct laser writing (DLW) relies on the phenomenon of two-photon polymerization (TPP), where the polymerization energy threshold of a photoresist can be overcome by the combination of the energy of two photons. Single photons with energies below the polymerization energy threshold do not possess the ability to initialize the polymerization. In DLW, a femtosecond pulsed laser with photon energies below this threshold is focused via an objective to a tiny spot (see **Figure 3.3a**). Since the energy of the photons is below the threshold, they simply pass through the photoresist towards the focal point. The focusing leads to a very high photon density and, thus, increases the probability of TPP. The volume of the focus with a sufficiently high photon density for TPP is called a volumetric pixel (short 'voxel'). In this work, all master structures are fabricated with a commercial DLW system (Photonic Professional GT, Nanoscribe GmbH) as depicted in **Figure 3.3b**. The system comprises a 780 nm laser with a pulse length of 100 fs at a repetition rate of 80 MHz. The large dimensions of the FFS cloaks necessitate a comparably large voxel size to reduce fabrication time. For this, a 25× 0.8NA (LCI Plan-Neofluar Imm CorrDIC, Carl Zeiss) objective is used, which is immersed into the photoresist IP-S (Nanoscribe GmbH). This choice results in a voxel diameter of ~600 nm and a voxel height of ~3 µm.

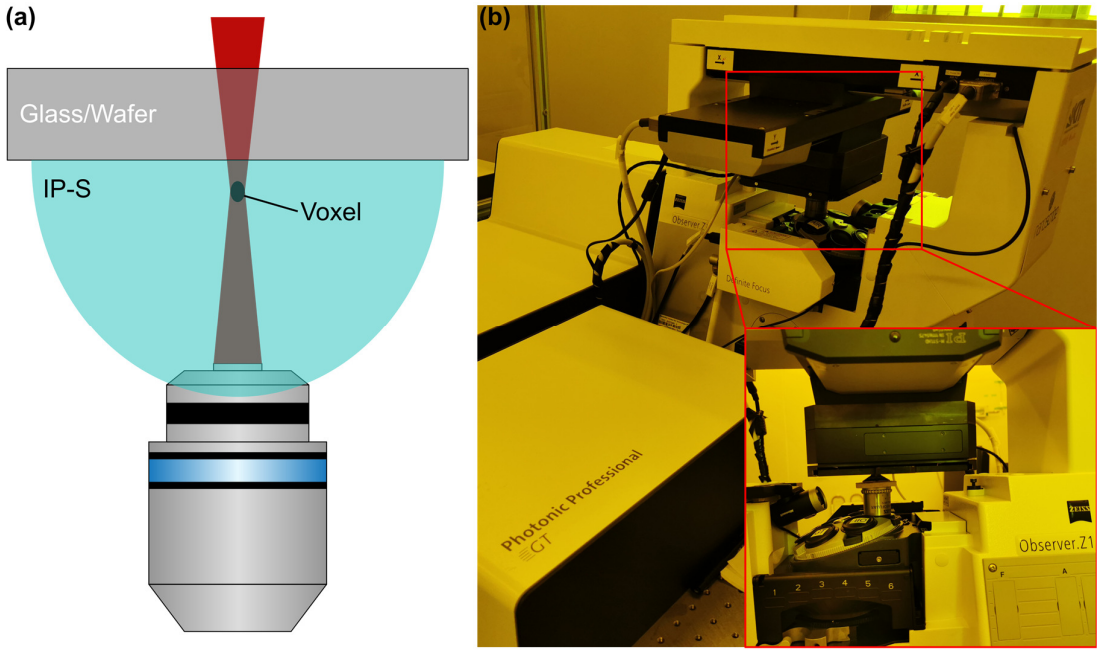

Figure 3.3: (a) Schematic representation of the dip-in technique. (b) Photograph of the Nanoscribe Photonic Professional GT during fabrication. The inset shows a side view of the objective and the working stage.

Silicon wafers (4") or indium tin oxide (ITO)-coated glass slides (25 x 25 mm) are used as substrates. The ITO layer on the glass slides interrupts the continuous transition of refractive indices from the photoresist to the glass and thus aids in the identification of the substrate interface when using the dip-in writing technique. The substrates are initially cleaned with a wiping cloth drained with acetone (Sigma-Aldrich) and isopropanol (IPA, Sigma-Aldrich). Solvent residues are removed using a nitrogen gun. Directly before applying the IP-S

photoresist via drop-casting, the substrates are placed on a hotplate with a temperature of 150°C for 15 min. This way, any water residuals are evaporated, which improves the adhesion of the photoresist to the substrate. To avoid any free-hanging parts of the structures due to a slight tilt of the substrate with regard to the scan stage, the structures are submerged into the substrate by 5 µm. The FFS cloaks needed to be written in a number of adjacent blocks since their dimension exceeds the maximum writing field of 300 x 300 x 300 µm³. The blocks also overlap by 5 µm and display a share angle of 15° to increase stability and avoid any stitching artifacts. After DLW exposure, unexposed resist is removed by placing the samples in a bath of propylene glycol methyl ether acetate (PGMEA, Sigma Aldrich) for 20 min and a subsequent bath of IPA for another 10 min. After drying, only the exposed structures remain. Since the fabricated structures in this thesis are not entirely exposed by the laser but rather consist of an outer shell and a scaffold, they are flood exposed in a ultraviolet (UV) irradiation chamber (BSL-01, Opsytec Dr. Gröbel GmbH) with a dose of 120 J/cm².

As indicated by the use of a shell and scaffold to fabricate the structures, the fabrication time of the FFS cloaks needs to be minimized. Exposing an impenetrable shell (20 layers) and a sparse tetrahedral scaffold (see **Figure 3.4**) beneath that is then cured via flood exposure marks the first and biggest step towards the minimization of fabrication time. In addition, fabrication is further reduced by optimizing four essential writing parameters:

(1) Piezo settling time: the necessary time for the piezo-controlled stage to move to the next writing position.
(2) Galvo settling time: the time that the galvanometric mirror system needs to settle down at a new position.
(3) Galvo acceleration: a unitless value proportional to its maximum controllable acceleration.
(4) Scan speed: the writing velocity of the laser.

For the investigation of these parameters, representative blocks of the scaffold illustrated in **Figure 3.4** are written with different sets of parameters and compared in terms of writing time. The first two parameters do not show any effect on the writing time and are thus kept at their default values of 20 ms and 2 ms, respectively.

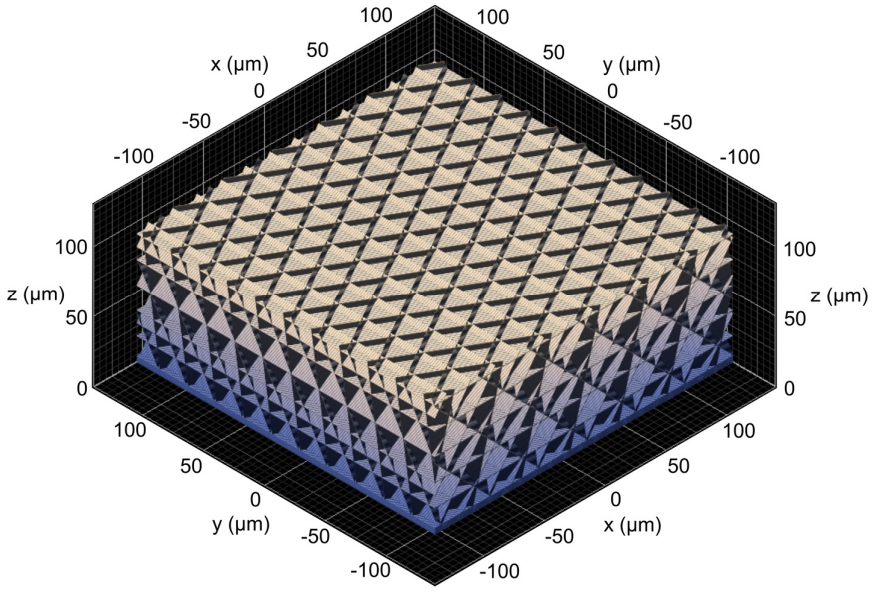

Figure 3.4: Illustration of the representative block of the scaffold carrying the outer shell of the FFS cloak, which is used to optimize the fabrication time in terms of writing parameters.

For the representative blocks, the galvo acceleration has far greater impact on the fabrication time than the piezo and galvo settling times. When fixing the laser scan speed at 80 mm s^{-1}, the fabrication reduces significantly with an increasing galvo acceleration but saturates at a value of 20 (see **Figure 3.5a**). The same trend is observable for the laser scan speed in **Figure 3.5b**, when keeping the galvo acceleration at its optimum value of 20. Scan speeds faster than 100 mm s^{-1} do not yield any significant additional reduction of the fabrication time. Therefore, a galvo acceleration of 20 and a scan speed of 120 mm/s are used throughout all experiments in this thesis. It should be pointed out that increasing galvo acceleration and scan speed may lead to fabrication inaccuracies. However, keeping the large dimensions of the FFS cloaks in mind these inaccuracies are of lesser concern.

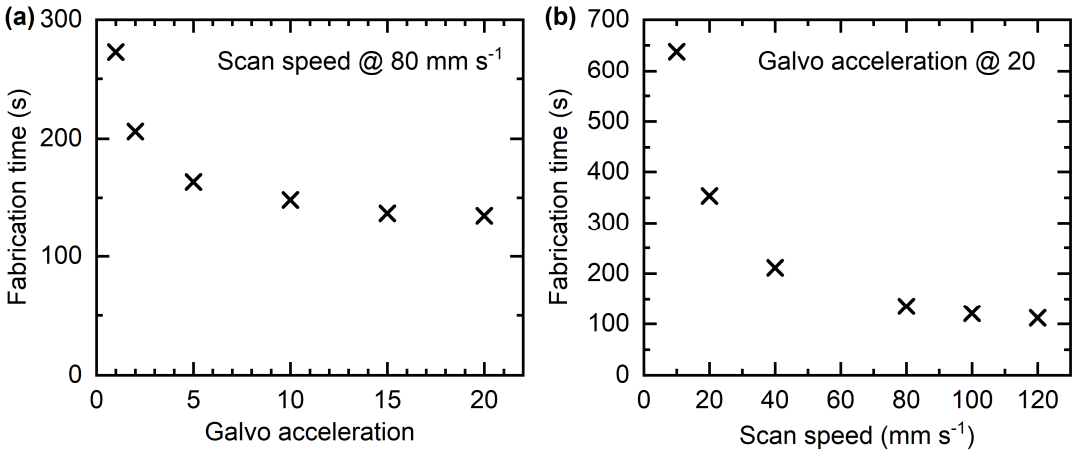

Figure 3.5: Fabrication time of the representative scaffold block in dependence of (a) the galvo acceleration and (b) the scan speed of the laser. The respectively other parameter is kept at a fixed value as indicated in each graph.

3.2.2 Fabrication of stamps for photo-nanoimprint lithography

The master structures fabricated via DLW are fragile and take a long time to be reproduced. Therefore, they are not suited for the direct use as stamps for the fabrication of FFS cloaks via photo-nanoimprint lithography, which is described in the next section. The stamp material of choice is polydimethylsiloxane (PDMS) since it enables the facile replication of master structures by drop casting and thermal curing. For the transfer of the master structures into a PDMS mold, a twofold replication into PDMS is required. The process is sketched in **Figure 3.6**.

First, the samples are coated with a 20 nm thick Al_2O_3 layer deposited via atomic layer deposition (ALD). In **Figure 3.6**, this layer is omitted for clarity. Since ALD is not in the focus of this study, the reader is referred to textbooks [82,83]. This Al_2O_3 layer acts as a bonding agent for the silane trichloro (1*H*,1*H*,2*H*,2*H*-perfluorooctyl) silane (PFOTS, Sigma Aldrich), which is coevaporated from a 3 mmol solution in cyclohexane (Sigma Aldrich) in the desiccator at a pressure of ~200 mbar. For an efficient coating, the samples are activated via an oxygen plasma in an in-house-built plasma asher for one minute at a power of 100 W. The PFOTS coating reduces the surface energy of the samples and thus avoids any undesired sticking of the PDMS to the IP-S master structure and the glass substrate [64]. Subsequently, the PDMS base and curing agent (Sylgard 184, Dow Corning) are mixed in a ratio of 10:1 and thoroughly stirred with a glass rod. Before usage, the mixture is placed under vacuum in a desiccator to eliminate all air inclusions.

In a next step, the PDMS is drop-casted over the coated master structures. A manually formed basin of aluminum foil prevents any PDMS of running down the samples. The basin is heated on a hotplate at 60°C for two hours, which increases the thermal curing of the PDMS. The replicated PDMS layer is then peeled off from the master structures and passes through the same silanization process including plasma activation

and the evaporation of PFOTS as described above. In a second replication step, PDMS is again drop-caster over the coated PDMS replica and thermally cured. This twofold replication results in an exact copy of the master structures. Only the shrinkage of PDMS during thermal curing of ~4% needs to be anticipated. After a final silanization of the second replica, the PDMS stamp is ready to be used for photo-nanoimprint lithography.

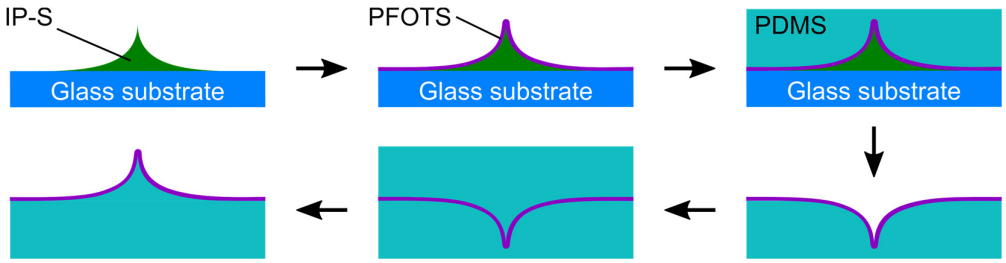

Figure 3.6: Schematic process of the fabrication of the master stamps used for photo-nanoimprint lithography. The used materials are indicated. Adapted with permission from [64]. © John Wiley & Sons, Ltd.

3.2.3 Photo-nanoimprint lithography

Photo-nanoimprint lithography, which is also known as ultraviolet nanoimprint lithography (UV-NIL), is a precise replication technique of nano- and microstructures on large scales that enables a high throughput [84–86]. It is designed for many optical and optoelectronic purposes [87,88]. The process relies on imprinting a master structure into a liquid photoresist layer, which is then cured via the exposure to UV light [89]. In this thesis, the glass-like photoresist OrmoComp (microresist technology GmbH) is used since it displays a high transparency, which is a key factor for any optoelectronic application [90].

The process applied in this thesis is roughly sketched in **Figure 3.7**. First, the stamp is aligned with regard to the surface of the solar module and with regard to the location of the inactive area. Subsequently, the stamp is imprinted into the resist (see **Figure 3.7b**), which is then cured via exposure to UV light. The vertical position is fixed by spacers explicitly designed for the dimensions of the FFS cloak. Finally, the stamp is lifted and the structured photoresist layer remains (see **Figure 3.7c**).

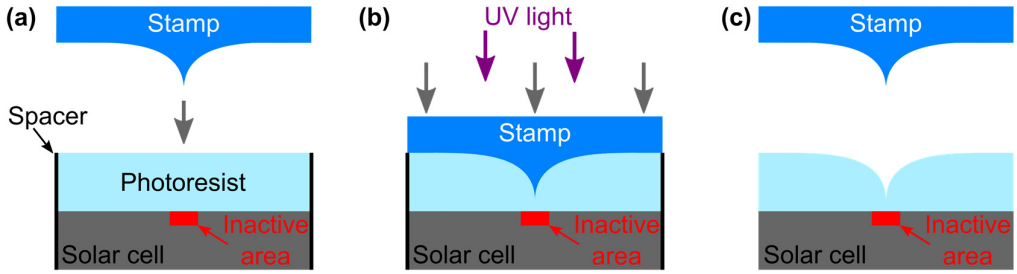

Figure 3.7: Illustration of the process of UV nanoimprint lithography of FFS cloaks. (a) The stamp is aligned with regard to the solar module's plane and the inactive area. (b) The stamp is imprinted into the liquid photoresist, which is then cured by UV light. (c) After curing, the imprinted FFS cloak remains in the cured photoresist.

One crucial aspect of UV-NIL in the context of FFS cloaking of inactive areas of solar modules and cells is the alignment of the FFS cloak with regard to the position of the inactive areas. For this, a dedicated optical setup is assembled (see **Figure 3.8**). It consists of two goniometric stages to compensate tilt between the solar cell and the stamp, a rotary stage to compensate rotational misalignment and an XYZ-stage to match the cloak's position with the inactive areas of the solar cell. Furthermore, the setup comprises a 1.2 W UV LED (WEPUV3-S2, Winger Electronics) with a wavelength of 400 nm for UV curing of the photoresist.

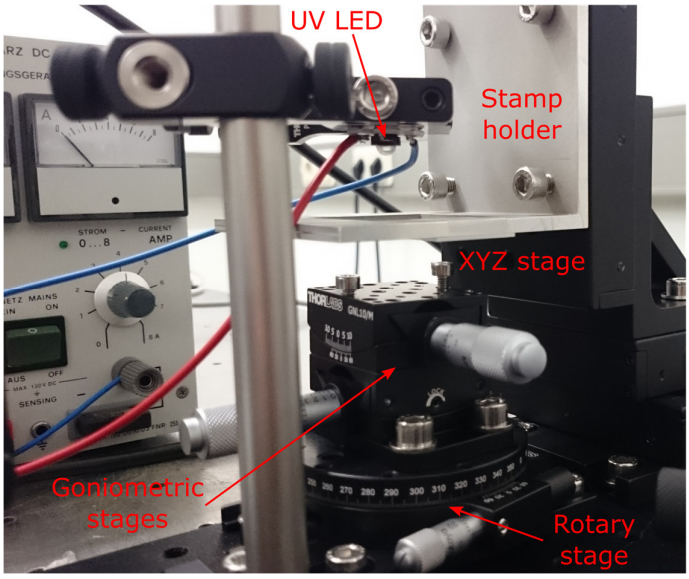

Figure 3.8: Photograph of the assembled optical setup for UV nanoimprint lithography.

3.3 Embedding freeform surface cloaks

Embedding the FFS cloaks in the conventional architecture of solar modules represented one of the main challenges of this thesis. Before the emergence of the liquid glass technique, the most intuitive approach for embedding FFS cloaks was the polymer encapsulant. This approach introduces the additional challenge to attach the cover glass to the structured polymer encapsulant. This section describes the applied techniques for encapsulation via polymer bonding and outlines the incorporation of FFS cloaks directly into the cover glass of the solar modules.

3.3.1 Polymer bonding

Imprinting the FFS cloak into a polymer layer requires the polymer to be shape-preserving under the subsequent encapsulation with a cover glass. The material of choice for this approach is the glass-like OrmoComp (micro resist technology GmbH) resist since it displays high optical transmittance and a good adhesion to a substrate after curing in addition to its high strength. However, its sturdiness poses a problem for the attachment of a cover glass. For a bond free of air inclusions between the glass and the glass-like resist, a perfectly planar OrmoComp surface is required. Such an idealized planar surface is hard to achieve, though, without intensive post-processing of the surface. Naturally, a liquid glue comes to mind that mediates the bond between the cover glass and the FFS cloak and accommodate the possible surface roughness in the planar regions of the cloaking layer due to fabrication inaccuracies. However, a liquid glue comes at the risk that not only the desired cavities would be filled but also the FFS cloak itself. Therefore, a slightly different approach is chosen.

The mold material PDMS, which is also used in several over techniques in this thesis, exhibits the unique properties of an excellent optical transparency far into the UV, easily controllable bonding properties and a certain elasticity that may be exploited to eliminate any air lock. For this, a thin layer of PDMS is cured and then placed in between the cover glass and the FFS cloak as a mediator as illustrated in **Figure 3.9**. It is then attached to the cover glass via plasma bonding. In plasma bonding, the PDMS film and the cover glass (Menzel cover slides, strength 1) are exposed to oxygen plasma in an in-house-built plasma asher for 15 s at a power of 100 W. Subsequently, both parts are firmly pressed together resulting in a permanent bond. This

step is repeated for the bond between PDMS and OrmoComp. Finally, a fully encapsulated solar cell with embedded FFS cloaks is obtained.

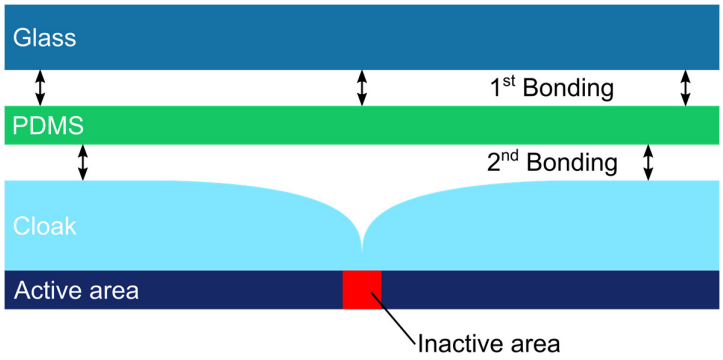

Figure 3.9: Schematic of the polymer bonding technique used to attach a cover glass to a FFS cloak, which is imprinted into an OrmoComp layer covering the solar cell.

3.3.2 Liquid glass

The recently developed liquid glass technique offers the unique ability to embed optical concepts as cavities into pure fused silica glass of a high optical quality [91]. Liquid glass is a photo-curable silica nanocomposite consisting of a silicon dioxide (SiO_2) nanopowder and a photo-curable monomeric binding matrix [92]. The latter enables the user to form the nanocomposite in any arbitrary geometry that the huge variety of polymer processing techniques enables [93,94].

The recipe of liquid glass has already been reported several times in literature and may even be varied depending on the targeted application [92–94]. Throughout this thesis, the monomeric binding matrix is composed of 68 vol% of a hydroxyethylmethacrylate (HEMA) monomer, 25 vol% of a phenoxyethanol (POE) solvent and 7 vol% of a tetraethyleneglycoldiacrylate (TEGDA) crosslinker as reported in Ref. [91]. No further modifications to this recipe are performed in the studies shown in Chapter 7. The monomeric mixture is then loaded with 50 vol% (with regard to the final mass of the nanocomposite) of a high-purity amorphous silica nanopowder (Zandosil) with a particle diameter of ~100 nm. In a final step, 0.5 wt% (with regard to the monomer mass) of a 2,2-dimethoxy-2-phenylacetophenone (DMPAP) photoinitiator is added to enable UV curing of the monomer matrix.

The property of being UV curable – or depending on the recipe thermally curable – opens up a vast variety of applicable fabrication techniques. Stereolithography, gray-scale lithography, various hot embossing techniques, subtractive machining of cured parts and photo-nanoimprint lithography find themselves among the already demonstrated techniques [92–94]. Due to the facile replication of the complex and fragile master structures into transparent PDMS stamps, UV nanoimprint lithography is used to transfer the FFS cloaks into the liquid glass nanocomposite for all results reported in Chapter 7.

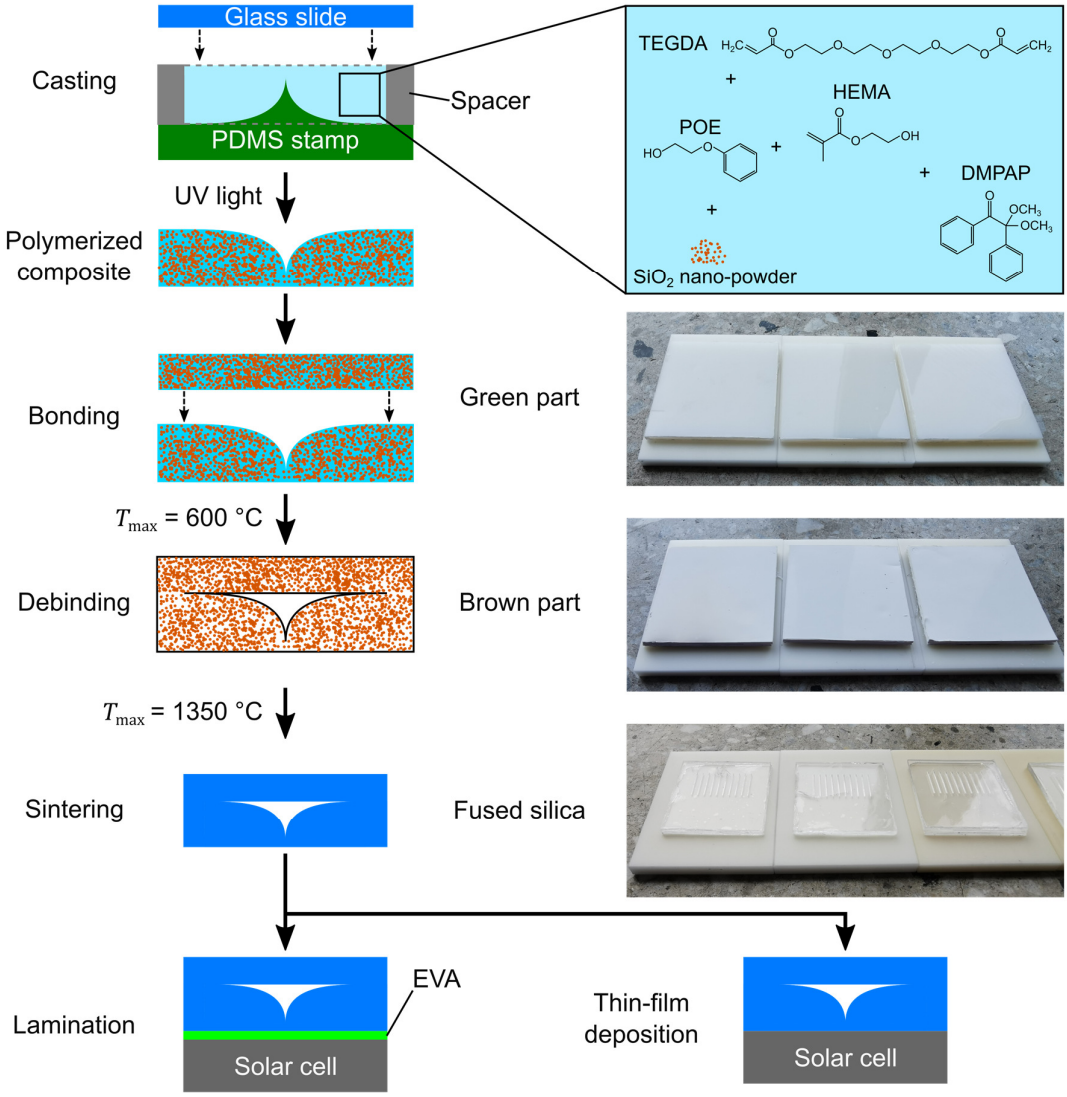

Figure 3.10: Illustration of the process steps of the liquid glass technique. The components of the nanocomposite are shown in the inset of the top right. Additionally, photographs of the samples after bonding (green part), debinding (brown part) and sintering (fused silica glass) are shown. Adapted with permission from [91]. © 2019 American Chemical Society.

The process steps of the applied liquid glass technique are sketched in **Figure 3.10**. First, a quadratic metallic frame with a specific inner side length and usually a thickness of ~1 mm is carefully positioned on the PDMS stamp to form a basin, which is then filled with the LG nanocomposite. A planar glass slide is pressed on the basin from the top. Additionally, the PDMS stamp is coated with PFOTS to reduce adhesion as outlined in Section 3.2.2. For the same purpose, a plastic foil is attached to the glass slide, which also facilitates the removal of the stiff glass slide later on. The enclosed nanocomposite is then exposed to UV light of a UV-LED array (E.E.T.S., U.K.) with a wavelength of $\lambda \sim 365$ nm and an intensity of 4.7 mW/cm² for 45 seconds. At this point the radical polymerization of the nanocomposite is not yet fully completed, which results in a slightly sticky surface. Additionally, a second slab of the nanocomposite with a thickness of ~500 µm is prepared in between two planar glass slides, which also display attached plastic foils, and exposed for mere 15 seconds. Thus, the radical polymerization of the second slab just started, which gives the slab a wax-like solidity. After peeling of the PDMS master stamp of the first slab and one of the planar glass slides, both half-cured slabs of nanocomposite are firmly pressed together and bonded under the UV-LED array by

finalizing the polymerization after another 30 seconds of UV exposure. This solid nanocomposite is the so-called 'green part'.

Subsequently, all polymeric material is thermally debinded from the green part in a tube furnace (GSL-1100X-LD, MTI Corporation) at a maximum temperature of 600°C, which results in the so-called 'brown part'. The used alumina tube is constantly flushed with ambient air via a pump to maintain an ambient atmosphere inside it. Afterwards, another tube furnace (GSL-1500X-50-UL, MTI Corporation) is used to sinter the brown part at 1350°C under vacuum ($p \sim 4 \cdot 10^{-2}$ mbar) to form high-purity fused silica glass. The detailed temperature curves for debinding and sintering are displayed in **Figure 3.11**. It should be noted that the heating rates during debinding might be increased for smaller parts. Therefore, the used temperature curve differs from the previous reports [94]. Another important aspect of the liquid glass technique is the solid loading of the nanocomposite with silica nanopowder, which leads to a precisely predictable isotropic shrinkage during sintering [93]. In the case of a solid loading of 50 vol% with the silica nanopowder, the shrinkage sums up to a value of 20.63 %, which needs to be anticipated in the fabrication of the metallic frames for UV nanoimprint lithography.

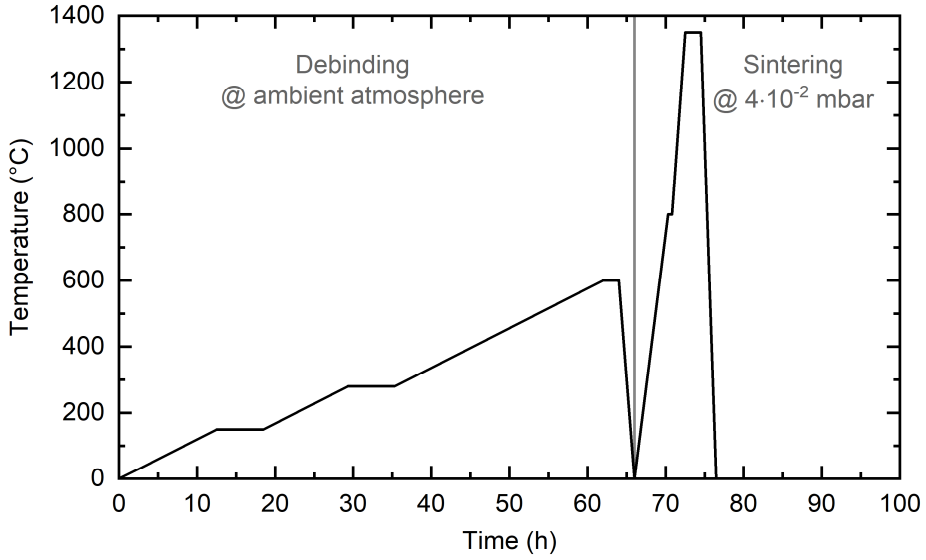

Figure 3.11: Temperature curves used during debinding and sintering of the polymerized nanocomposite. The applied atmospheric conditions are indicated.

Since it is common to silicon and CIGS PV to laminate cover glass to the solar cells or modules with a polymeric encapsulant, the embedded FFS cloaks are laminated to the investigated silicon solar cells in the same way. For this, a commercial PV module laminator (E.E.T.S.) and ethylene vinyl acetate (EVA) – a standard polymeric encapsulant – are employed. The lamination is performed at a temperature of 100°C and a pressure of 4 mbar.

To reduce surface roughness and to facilitate the deposition of thin-film solar cells on the cover glass fabricated via the liquid glass technique, mechanical polishing is conducted. For grinding and polishing, a grinding and polishing machine (Saphir 350 E with Rubin 520, ATM GmbH) is used. The detailed steps of the polishing process are summarized in **Table 3.2**. For all process steps, a pressure of ~1 bar is applied.

Table 3.2: Summary of the grinding and polishing process applied to cover glass fabricated via the liquid glass technique to reduce surface roughness. All process steps are performed at a pressure of ~1 bar.

Step	Base	Lubricant	Speed (rpm)	Time (min)
1	MD Piano 220[1]	Water	300	Until planar
2	MD Piano 500[1]	Water	300	2:00
3	MD Piano 1200[1]	Water	300	2:00
4	SiC paper 2000[1]	Water	300	2:00
5	SiC paper 4000[1]	Water	300	2:00
6	MD Plan[1]	Diamond suspension 9 µm[2]	150	10:00
7	MD Plan[1]	Diamond suspension 3 µm[2]	150	10:00
8	MD Plan[1]	Diamond suspension 1 µm[2]	150	10:00

3.4 Fabrication of perovskite solar cells

For the deposition of perovskite solar cells on top of cover glass fabricated via the liquid glass technique, a fully evaporated layer stack is used. To reduce resistive losses on the targeted active area of 381 mm², a 75 nm-thick gold grid with 200 µm-wide fingers spaced 1.8 mm apart is deposited via thermal evaporation. Additionally, 150 nm of sputtered ITO complement the front electrode. Then, a 5 nm-thick layer of 2,2',7,7'-Tetra(*N,N*-di-*p*-tolyl)amino-9,9-spirobifluorene (Spiro-TTB) is employed as the hole transport layer. It is deposited via thermal evaporation. The absorber $CH_3NH_3PbI_3$ is deposited with a final thickness of 500 nm via the co-evaporation of CH_3NH_3I and PbI. Details on the co-evaporation process are available in Ref. [95]. Furthermore, 21 nm of C_{60} and 5 nm of bathocuproine (BCP) are processed via thermal evaporation. The layer stack of the perovskite solar cells (see **Figure 3.12**) is completed by a 75 nm-thick gold rear metallization processed by thermal evaporation. For sputtering and thermal evaporation, machines of Kurt J. Lesker Company Ltd. are used. Since the optimization of thin-film deposition techniques is not in the focus of this thesis the reader is referred to textbooks [96].

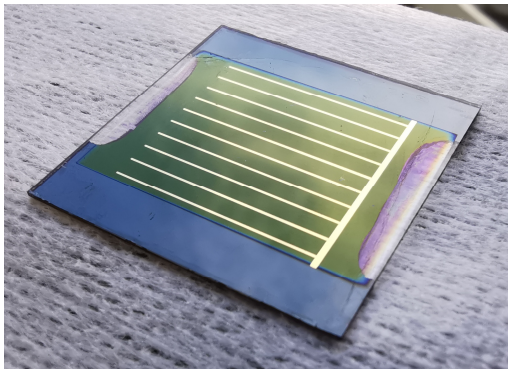

Figure 3.12: Image of a perovskite solar cell deposited on a fused silica glass wafer with a size of 30 mm x 30 mm.

[1] The MD Piano resin bonded diamond discs, the SiC paper and the MD Plan polishing cloths are supplied by Struers GmbH.

[2] The diamond suspensions with various diamond grain sizes are supplied by ATM GmbH.

3.5 Characterization

This section provides a brief overview and short descriptions of all characterization techniques and setups applied. For further information on the techniques for PV characterization, spectrophotometry, optical and atomic force microscopy the reader is referred to textbooks [65,97–99].

Current density – voltage characteristic:
The power conversion efficiency, which is derived from the *J-V* characteristic, is one of the most important figures-of-merit for photovoltaic devices. The *J-V* characteristic is standard test conditions under illumination with a reference AM1.5G solar spectrum (see **Figure 1.1**). This spectrum is defined as the irradiance of the sun at 41° above the horizon, which corresponds to an air mass of 1.5 atmospheres, onto a solar cell that is tilted by 37°. The total irradiance sums up 1000 W/m². The measurements shown in this thesis are performed with a commercial solar simulator of class AAA (WXS-90S-L2 by WACOM, Saitama, Japan), which imitates the AM1.5G spectrum using a halogen and a Xenon lamp.

External quantum efficiency:
The EQE provides information about the wavelength-dependent performance of a solar cell. It is defined as the probability of an incident photon to contribute to the extracted current. The EQE measurements reported in this thesis are performed with a home-built setup that consists of a xenon lamp as a light source, a monochromator with a spectral bandwidth of approximately 5 nm and a chopper that is set to 120 Hz. The EQE measurement is a relative quantity that relates the measured current to the current of a reference cell with a known EQE. As a reference cell, a silicon photodiode (SN: 8B047) with a certified EQE in the wavelength range of 300 – 1100 nm is used.

Optical microscopy:
For the qualitative analysis of the fabrication quality of freeform surface cloaks, optical microscopy is applied, which enables simple imaging of microscopic features. In this work, a VHX-500 optical microscope (Keyence Corporation) is used, which employs a VH-Z500 (Keyence Corporation) lens system with a maximum magnification of 5000x.

Spectrophotometry:
For measurements of diffuse reflectance and transmittance, a commercial Lambda 950 UV-Vis spectrophotometer (PerkinElmer, Inc.) is used. In spectrophotometry, the amount of light reflected or transmitted by a sample is compared to a calibration measurement to quantify reflection and transmission. For area-dependent measurements, the spot is shaped in a rectangular form with a size of 1mm x 4mm by integrating apertures into the beam path.

Scratching tests:
Pencil tests according to the ASTM D3363 standard are carried out to determine the resistance of cover glass fabricated via the liquid glass technique to scratch damage [100]. In this work, Staedtler Mars Lumograph drawing pencils in the hardness range from 9H to 9B are employed, whose heads are flattened before the test by rubbing the lead to abrasive paper (grit 400). An angle of 90° is maintained the pencil's head exhibits a planar tip. The standard defines that the pencil should be firmly pushed across the sample's surface for minimum 3 mm at an angle of 45°.

Atomic force microscopy:
For the analysis of the surface roughness of substrates with embedded freeform surface cloaks processed from liquid glass, atomic force microscopy (AFM) is performed using a JPK NanoWizard ULTRA Speed 2 (Bruker Nano GmbH). This technique provides the possibility to extract 2D height profiles by running a microscopic cantilever across the sample and tracing its deflection via the investigation of a reflected laser beam in an interferometer.

4 Methodology of energy yield modelling

The prevailing figure-of-merit for solar cell performance – the power conversion efficiency (PCE) – provides only a limited assessment of the realistic performance of tandem solar cells and modules. It poorly represents the constantly varying solar irradiation and temperature conditions that a solar module is exposed to in a realistic scenario since the PCE is determined under standard test conditions (STC), which specifies a standard global reference irradiance spectrum of 1000 W/m² with an air mass 1.5 (AM1.5G), normal incidence and a solar cell temperature of 25°C The complex architecture of tandem solar modules, in particular the combination of two absorber materials with different bandgaps, requires another, more appropriate parameter that describes the ability to convert incoming sunlight into power. Alongside the rise of III-V/silicon and perovskite/silicon tandem PV, the parameter energy yield (EY) cut its way into the PV community [9,21–25,101–106]. The EY is a more suitable figure-of-merit, especially in the context of tandem PV, since it accounts for the varying spectral distribution and intensity levels of specular and diffuse solar irradiation, the impact of cloud cover (CC), temperature changes over the course of hours, months and seasons, as well as the module installation at various geographical locations (see **Figure 4.1**). In particular, EY modelling enables a more realistic assessment of the impact of these varying conditions on current matching in the two-terminal configuration of tandem solar modules. In order to meet these requirements, EY modelling relies on a number of models and assumptions. This section thus provides a detailed overview about the methodology employed in our EY modelling framework, which was already used in various publications [9,24].

Acknowledgements and contributions

The methodology of energy yield modelling outlined in the following chapter was already published in Ref. [107]. *This chapter is separated from the main methods chapter since this well-enclosed topic is a result of this thesis. The underlying simulation framework consists of four individual modules: the energy yield core module (developed by the first author Raphael Schmager), the irradiance module (developed by the co-author Ulrich W. Paetzold and advanced by the shared first authors Raphael Schmager and Malte Langenhorst), the optics module (developed by Malte Langenhorst) and the electrics module (developed by the co-author Jonathan Lehr and enhanced by Raphael Schmager). The publication is a joint project of the shared first author Malte Langenhorst, who composed the parts on realistic irradiation conditions and optical modelling of perovskite-based textured tandem solar modules, and the first author Raphael Schmager, who wrote the sections on electrical modelling, energy yield calculation and the demonstration of the framework.*

4.1 Framework for energy yield modelling

The framework for EY modelling developed in the research group of Ulrich W. Paetzold consists of four independent modules (see **Figure 4.2**): (1) the energy yield core module, (2) the irradiance module, (3) the optics module and (4) the electrics module. The flow of this framework starts with the calculation of hourly-resolved irradiance spectra $I(\lambda)$ for an entire year at a given location based on measured typical meteorological year (TMY3) data available from the National Renewable Energy Laboratory (NREL) [108]. In addition, the optics module provides the spectrally resolved absorptance $A(\lambda, \alpha)$ of a tandem solar module for all angles of incidence. The energy yield core module subsequently combines these two inputs and determines the hourly resolved J_{SC}, which itself is key to the calculation of the J-V characteristic conducted within the electrics module. By summing up the resulting power at each single maximum power point (MPP) the energy yield core module is capable of determining the annual EY for a specific module orientation at a given location. The detail modelling steps in each module are outline in the following sections.

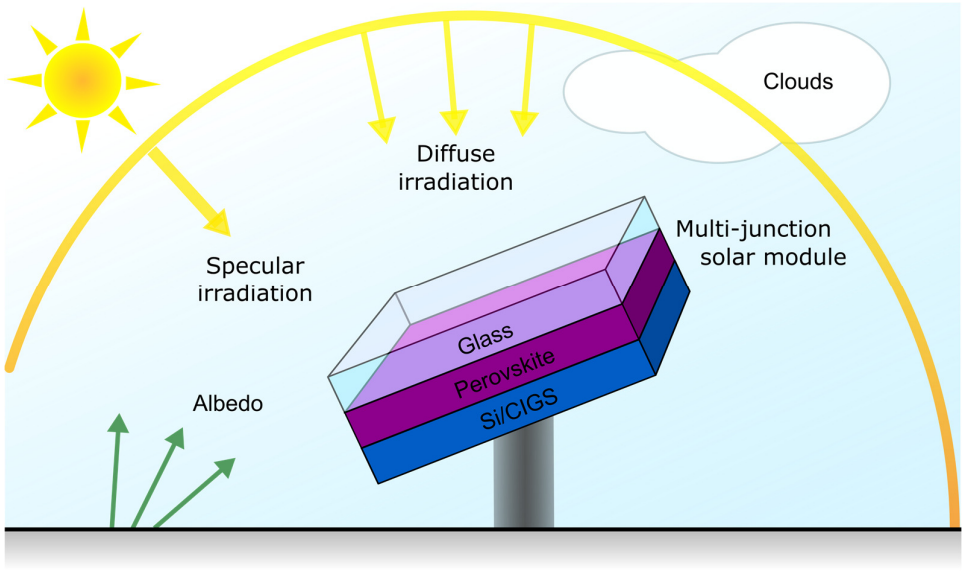

Figure 4.1: Schematic of the module installation and the daily variations of specular and diffuse solar irradiation, albedo, cloud cover and temperature. Adapted with permission from Ref. [107], © 2019 Optical Society of America.

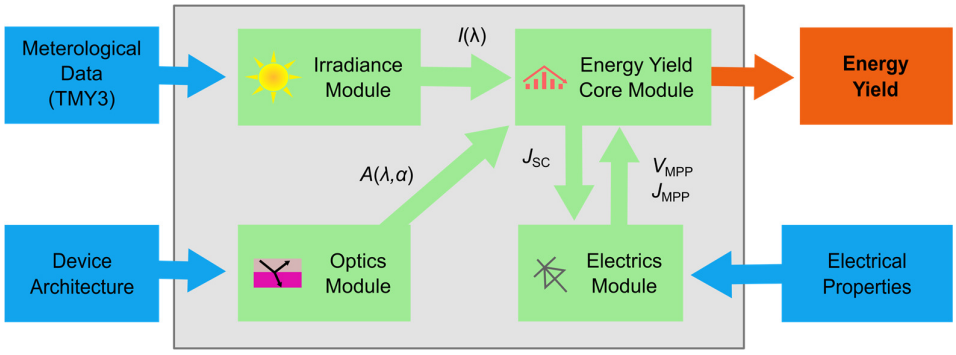

Figure 4.2: Schematic of the flow of the modular framework for energy yield modelling, which consists of the irradiance, the optics, the electrics and the energy yield module. Reprinted with permission from Ref. [107], © 2019 Optical Society of America.

4.2 Realistic irradiation conditions

For each location, the irradiance module calculates the incident irradiance spectra based on meteorological data provided by the TMY3 data set [108]. This data covers several climatic zones ranging from tropical to boreal climates and enables the EY modelling of PV devices in numerous locations. This data includes a variety of meteorological parameters, such as the direct normal and diffuse horizontal irradiance, CC, dry-bulb temperature, pressure, precipitable water, aerosol optical depth and albedo. In the first instance, the framework calculates the clear sky irradiance in the range of 280 – 4000 nm via the 'simple model of radiative transfer of sunshine' (SMARTS) [109]. Proceeding from this clear sky irradiance, the framework applies a simple model for cloud cover. This model assumes that the spectral distribution of direct irradiation $I_{\mathrm{clear,dir}}(\lambda)$ is not affected; only its overall intensity is scaled to the measured absolute intensity of direct irradiance $I_{\mathrm{meas,dir}}$ in the TMY3 data:

$$I_{\mathrm{clouds,dir}} = \frac{I_{\mathrm{clear,dir}}(\lambda)}{\int I_{\mathrm{clear,dir}}(\lambda)\, d\lambda} I_{\mathrm{meas,dir}} \,. \tag{4.1}$$

In contrast, the spectral distribution of diffuse clear sky irradiance changes dependent on the amount of cloud cover, since grey to white clouds differ significantly in color from the usually blue-colored diffuse solar irradiation. The framework thus assumes that light originating from clouds exhibits the same spectral distribution as direct clear sky irradiance. Furthermore, the diffuse irradiance is scaled to the measured absolute intensity of diffuse irradiance $I_{\mathrm{meas,diff}}$ in the TMY3 data:

$$I_{\mathrm{clouds,diff}} = \frac{I_{\mathrm{clear,diff}}(\lambda)\cdot(1-\mathrm{CC}) + I_{\mathrm{clear,dir}}(\lambda)\cdot\mathrm{CC}}{\int\left[I_{\mathrm{clear,diff}}(\lambda)\cdot(1-\mathrm{CC}) + I_{\mathrm{clear,dir}}(\lambda)\cdot\mathrm{CC}\right] d\lambda} I_{\mathrm{meas,diff}} \,. \tag{4.2}$$

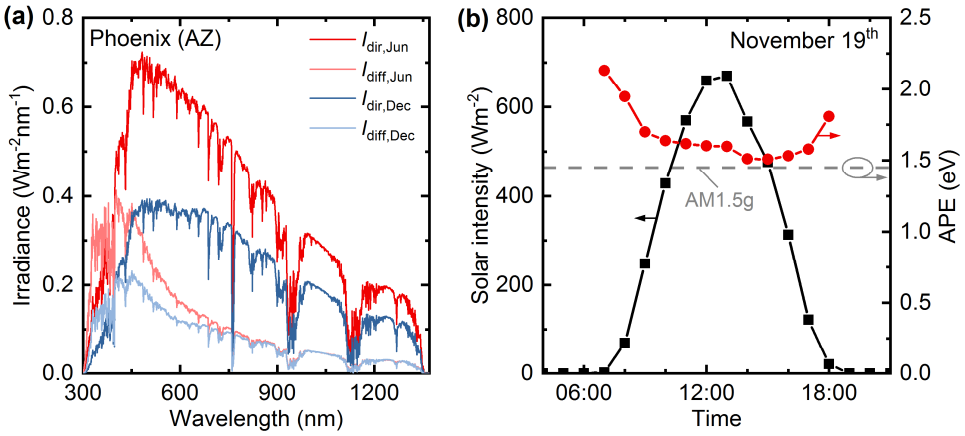

Figure 4.3: (a) Monthly averaged direct and diffuse irradiance spectra for June (red spectra) and December (blue spectra) in Phoenix, Arizona. (b) Varying solar intensity and average photon energy (APE) for a chosen day (Nov 19th) in Phoenix, Arizona. Reprinted with permission from Ref. [107], © 2019 Optical Society of America.

In order to illustrate the irradiance model, the average direct and diffuse irradiance in Phoenix (Arizona, USA) for June and December are displayed in **Figure 4.3a**. Apart from the obviously higher irradiance in summer, this figure reveals a strong blue-shift of diffuse irradiation in June compared to December, due to the low cloud cover prevailing in the sunny and arid summer of Phoenix. In general, diffuse irradiation exhibits a strong blue-shift compared to direct irradiation due to the strong wavelength dependence of Rayleigh scattering ($\sim\lambda^{-4}$). Spectral variations in solar irradiation are well described by the average photon energy (APE), which is an important parameter in the following discussions on EY. This APE does not only

vary with seasons as implied by the blue-shift of diffuse irradiation in summer in **Figure 4.3a**, but it varies also on much smaller time scales, such as a single day (see **Figure 4.3b**). For the chosen day (Nov 19th), the APE increases in the early morning and late evening hours due to the predominant contribution of blue-rich diffuse irradiation [9,25]. Moreover, the APE of realistic spectra differs significantly compared to AM1.5G throughout the most of the day. This fact highlights the importance of considering realistic irradiation conditions for the assessment of the performance of tandem solar modules.

Even though the applied model for CC is simple it should be kept in mind that radiative transfer in clouds is a multifaceted matter [110,111] since the transmission and scattering behavior of clouds depends on a variety of parameters, such as cloud thickness, particle density and particle size [112]. For this reason, there is no unified model for the radiative transfer of solar irradiation through clouds [113]. Nonetheless, this simple model provides a possibility to consider CC in EY modelling. In addition, the assumption of more blue-rich irradiance for low levels of CC matches with a previous study by Bartlett *et al*. [110].

4.3 Optical modelling of textured tandem solar modules

Optical modelling of the architecture of state-of-the art perovskite-based tandem solar modules represents a key challenge since these solar modules commonly exhibit three distinct features – (1) thin-film multi-layer stacks, (2) 'optically-thick' layers and (3) textured interfaces – that require the application of different optical simulation methods. Some simulation methods, like finite-difference time-domain simulations, are capable of simulating such complex architectures but significantly exceed acceptable computation times. For this reason, the author developed a new simulation code based on a matrix formalism for the calculation of light propagation [114]. This optical simulation code, which is a module of an entire EY modelling framework, is on the on hand able to handle the complex architecture of textured tandem solar modules and on the other hand keeps computation times below 30 seconds using main-stream computing hardware (Intel i5-8250u).

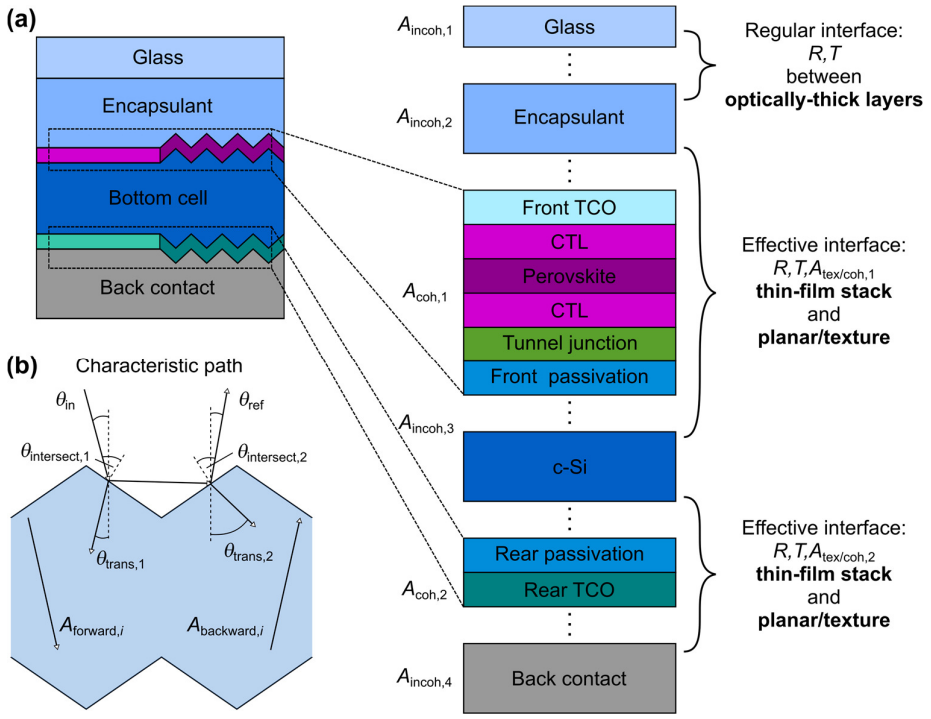

Figure 4.4: (a) Illustration of the separation of the complex architectures into smaller domains. The absorptance of textured tandem solar modules for all relevant wavelengths λ and all angles of incidence θ_{in} is simulated by combining all domains via a matrix formalism. (b) Illustration of a characteristic light path of pyramidal textures. Reprinted with permission from Ref. [107], © 2019 Optical Society of America.

The modelling approach breaks down the architecture into smaller domains (see **Figure 4.4a**) that are treated separately with the adequate simulation methods. In the end, the optical response is then calculated by combining the individual results via redistribution matrices following a formalism for light propagation in 'optically-thick' layers proposed by Eisenlohr *et al.* [114]. This formalism is extended by considering thin-film covered textured interfaces as *effective interfaces* that are able to absorb light.

Thin-film multi-layer stacks: The first distinct feature of perovskite-based tandem solar modules are the multiple thin films of the electrodes, ARC and the perovskite top cell, in which thin-film interference patterns may arise. The transfer-matrix method (TMM) is a rapid and accurate method suitable for the calculation of the absorptance A_{coh} in such features. The applied code is inspired by previous work on multilayer optical calculations [76] and is described in detail in Section 3.1.1.

'Optically-thick' layers: Contrary to thin-film multi-layer stacks, which require coherent treatment of light, absorptance in incoherent, thick layers A_{incoh} is sufficiently described using the classical Beer-Lambert law (please refer to Section 3.1.1):

$$A_{\mathrm{incoh}}(\lambda) = \begin{bmatrix} e^{-\alpha(\lambda)\cdot d/\cos\theta_1} & & 0 \\ & \ddots & \\ 0 & & e^{-\alpha(\lambda)\cdot d/\cos\theta_n} \end{bmatrix}, \tag{4.3}$$

where $\alpha(\lambda)$ is the absorption coefficient, d the thickness of the incoherent layer, and θ_{n} the angle of light propagating through the medium.

Textured interfaces: As outlined in Section 3.1.3, geometrical raytracing, as proposed by Baker-Finch and McIntosh [77], is an elegant method suitable for the rapid calculation of the impact of pyramidal textures on an interface for all angles of incidence θ_{in}. The high symmetry of pyramidal textures commonly employed in PV allows only for a limited set of characteristic paths with specific intersection angles $\theta_{\mathrm{intersect}}$ (see **Figure 4.4b**). Further illustrations of the characteristic paths of pyramidal textures is provided in the dedicated description of geometrical raytracing in Section 3.1.3. For textures covered with a thin-film multi-layer stack, the total absorptance $A_{\mathrm{path},i}$ along a path i is then calculated by summing up the absorption at each intersection j:

$$\begin{aligned} A_{\mathrm{path},i}(\lambda,\theta_{\mathrm{in}}) &= A_{\mathrm{coh}}\left(\lambda,\theta_{\mathrm{intersect},1}\right) \\ &+ \sum_{j=2}^{j_{\max}} \prod_{k=1}^{j-1} R_{\mathrm{coh}}\left(\lambda,\theta_{\mathrm{intersect},k}\right)\cdot A_{\mathrm{coh}}\left(\lambda,\theta_{\mathrm{intersect},j}\right). \end{aligned} \tag{4.4}$$

Subsequently, summing up the absorptance along all characteristic paths weighted by their individual probabilities $p_{\mathrm{path},i}$ allows the determination of the total absorptance of a thin-film covered texture:

$$A_{\mathrm{tex,coh}}(\lambda,\theta_{\mathrm{in}}) = \sum_i p_{\mathrm{path},i}(\theta_{\mathrm{in}})\cdot A_{\mathrm{path},i}(\lambda,\theta_{\mathrm{in}}). \tag{4.5}$$

The impact of texturing on reflectance $R_{\mathrm{path},i}$ and transmittance $T_{\mathrm{path},i}$ along path i is defined similary:

$$R_{\mathrm{path},i}(\lambda,\theta_{\mathrm{in}}) = \prod_{k=1}^{j_{\max}} R_{\mathrm{coh}}\left(\lambda,\theta_{\mathrm{intersect},k}\right) \tag{4.6}$$

$$T_{\mathrm{path},i}(\lambda,\theta_{\mathrm{in}}) = T_{\mathrm{coh}}\left(\lambda,\theta_{\mathrm{intersect},1}\right) + \sum_{j=2}^{j_{\max}} \prod_{k=1}^{j-1} R_{\mathrm{coh}}\left(\lambda,\theta_{\mathrm{intersect},k}\right) \cdot T_{\mathrm{coh}}\left(\lambda,\theta_{\mathrm{intersect},j}\right) \ . \quad (4.7)$$

Analogous to Equation (4.5), a summation weighted by the probability of each path then leads to the overall reflectance and transmittance of the thin-film covered textured interface:

$$R/T_{\mathrm{tex,coh}}(\lambda,\theta_{\mathrm{in}}) = \sum_{i} p_{\mathrm{path},i}(\theta_{\mathrm{in}}) \cdot R/T_{\mathrm{path},i}(\lambda,\theta_{\mathrm{in}}) \ . \quad (4.8)$$

In addition to the mere amount of reflectance and transmittance, geometrical raytracing also provides the possibility to determine the angular distribution of both parameters. For each wavelength, R and T can thus be described in terms of redistribution matrices $\left(\theta_{\mathrm{in}} \rightarrow \theta_{\mathrm{ref/trans}}\right)$ analogue to the approach of J. Eisenlohr and N. Tucher [114,115]:

$$R/T_{\mathrm{tex,coh}}(\lambda) = \begin{bmatrix} R/T_{\mathrm{tex,coh}}(\lambda,\theta_1 \rightarrow \theta_1) & \cdots & R/T_{\mathrm{tex,coh}}(\lambda,\theta_{\mathrm{n}} \rightarrow \theta_1) \\ \vdots & \ddots & \vdots \\ R/T_{\mathrm{tex,coh}}(\lambda,\theta_1 \rightarrow \theta_{\mathrm{n}}) & \cdots & R/T_{\mathrm{tex,coh}}(\lambda,\theta_{\mathrm{n}} \rightarrow \theta_{\mathrm{n}}) \end{bmatrix} . \quad (4.9)$$

The Equations (4.3) - (4.9) define a thin-film covered texture in the form of an *effective interface* (see **Figure 4.5a**), which should meet the condition that all incident light will be either reflected, transmitted or absorbed:

$$\sum_{\theta_{\mathrm{ref}}} R_{\mathrm{tex,coh}}(\lambda,\theta_{\mathrm{in}} \rightarrow \theta_{\mathrm{ref}}) + \sum_{\theta_{\mathrm{trans}}} T_{\mathrm{tex,coh}}(\lambda,\theta_{\mathrm{in}} \rightarrow \theta_{\mathrm{trans}}) + A_{\mathrm{tex,coh}}(\lambda,\theta_{\mathrm{in}}) = 1 \ . \quad (4.10)$$

Finally, the Equations (4.3) and (4.9) provide all information required for applying the redistribution matrix formalism proposed by Eisenlohr *et al.* [114], which is extended in this work by considering absorption at each *effective interface* according to Equation (4.5). This extended matrix formalism is illustrated in **Figure 4.5b**. When substituting the angular power distribution of both reflectance $R_{\mathrm{tex,coh}}$ and transmittance $T_{\mathrm{tex,coh}}$ (see **Figure 4.5a**) by a generalized redistribution matrix S_i, the angular power distribution x_i' and x_i are linked to each other via the following set of matrix multiplications:

$$\begin{aligned} x_{2i}' &= (S_1 M S_2 M)^i x_0' \\ x_{2i+1}' &= (S_2 M S_1 M)^i S_2 M x_0' \\ P_i' &= \sum_{\theta} (x_i')_{\theta} \\ x_2 &= M S_2 M x_0' \\ x_{2i} &= (M S_2 M S_1)^{i-1} x_2 \\ x_{2i+1} &= (M S_1 M S_2)^i M x_0' \\ P_i &= \sum_{\theta} (x_i)_{\theta} \end{aligned} \quad (4.11)$$

Here, the angular power distribution describes how much power propagates in a certain angular direction inside the optically-thick layer.

All remaining power P_i and P_i' is obtained by summation over all angles θ of the angular power distribution x_i and x_i', respectively. Finally, the total absorptance in an incoherent layer is then determined

by iteratively summing up the absorption of all light running in forward and backward direction through this layer until the incident power is completely absorbed:

$$\begin{aligned} A(\lambda,\theta_{\mathrm{in}}) &= A_{\mathrm{forward}}(\lambda,\theta_{\mathrm{in}}) + A_{\mathrm{backward}}(\lambda,\theta_{\mathrm{in}}) \\ &= \sum_{i=0}^{i_{\max}} A_{\mathrm{forward},i}(\lambda,\theta_{\mathrm{in}}) + \sum_{i=1}^{i_{\max}} A_{\mathrm{backward},i}(\lambda,\theta_{\mathrm{in}}) \\ &= \left(\sum_{i}^{i_{\max}} (P'_{2i} - P_{2i+1})\right) + \left(\sum_{i}^{i_{\max}} (P'_{2i+1} - P_{2i})\right). \end{aligned} \tag{4.12}$$

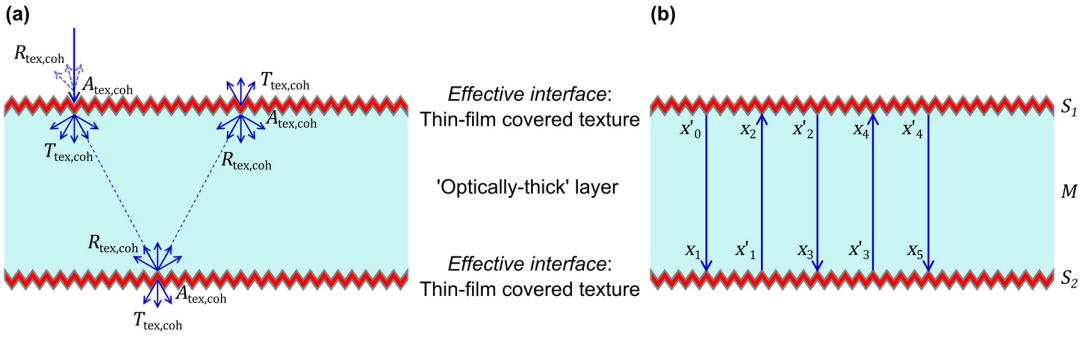

Figure 4.5: (a) Illustration of the extended redistribution matrix formalism for light propagation in 'optically-thick' layers. (b) Illustration of light propagation in the 'optically-thick' layer.

An incoherent layer does not necessarily need to be coated by a thin-film layer and might just behave like a classical interface according to the Fresnel Equations (see Equation (2.19) and (2.20) in Section 2.2.1) and Snell's law (see Equation (2.18) in Section 2.2.1). Moreover, the presence of planar interfaces obviates the need for geometrical raytracing. In the end, adding the absorptance of one incoherent layer after the other in the direction of light propagation according to Equation (4.12) enables calculating of the overall absorptance of the complex architecture of a textured perovskite-based tandem solar module.

4.4 Electrical modelling

In order to calculate the power output for a given J_{SC}, the electrics module computes the J-V characteristic of a solar module for a set of electric solar cell properties, such as the dark saturation current density J_0, the series resistance R_{S}, the shunt resistance R_{sh}, the diode ideality factor n and the module temperature T_{module}. For this, it employs the single-diode model based on the Shockley diode Equation:

$$J(V) = J_{\mathrm{SC}} - J_0\left(e^{\frac{V+JR_{\mathrm{S}}}{nkT_{\mathrm{module}}}} - 1\right) - \frac{V + JR_{\mathrm{S}}}{R_{\mathrm{sh}}}. \tag{4.13}$$

The second meteorological parameter, apart from the irradiance, that affects the J-V characteristic of a solar module and thus its annual energy yield is the temperature. In general, temperature modelling of solar modules is a complex matter since T_{module} relies crucially on meteorological conditions, such as wind and precipitation, and on the module installation as well as the heat transfer in between various parts of the module's architecture [116]. At this point, it should be noted that temperature effects are neglected throughout this thesis since the following investigations are of a purely optical nature. Nonetheless, the

methodology of temperature-dependent EY modelling of solar modules is provided within this section. The module temperature used in Equation (4.13) is calculated based on the nominal operating cell temperature (NOCT). T_{module} deviates from the ambient temperature T_{ambient} based on the NOCT and the insolation S [117,118]:

$$T_{\mathrm{module}} = T_{\mathrm{ambient}} + \frac{\mathrm{NOCT} - 20°\mathrm{C}}{800\ \mathrm{W/m^2}} \cdot S\,. \tag{4.14}$$

In this model, the NOCT is defined as T_{module} at an insolation of 800 W/m², wind speed of 1 m/s and an ambient temperature of 20°C. In addition, the impact of a decreasing bandgap with increasing T_{module} on the parameters V_{OC} and J_{SC} is often modeled via:

$$V_{\mathrm{OC}} = V_{\mathrm{OC,0}}\left(1 + \frac{t_{V_{\mathrm{OC}}}}{10^6}(T_{\mathrm{module}} - T_0)\right) \tag{4.15}$$

$$J_{\mathrm{SC}} = J_{\mathrm{SC,0}}\left(1 + \frac{t_{J_{\mathrm{SC}}}}{10^6}(T_{\mathrm{module}} - T_0)\right), \tag{4.16}$$

where $V_{\mathrm{OC,0}}$ and $J_{\mathrm{SC,0}}$ are the V_{OC} and J_{SC} at room temperature $T_0 = 25°\mathrm{C}$. The temperature coefficients $t_{V_{\mathrm{OC}}}$ and $t_{J_{\mathrm{SC}}}$ are commonly defined with the unit ppm K^{-1} [119].

Since Equation (4.13) is a transcendental Equation, it cannot be solved conventionally. Employing the Lambert*W* function [120,121] offers a route to obtain an explicit analytical solution for J following the approach of Jain *et al.* [122]:

$$\begin{aligned} J(V) = &-\frac{nV_{\mathrm{th}}}{R_{\mathrm{S}}}\mathrm{Lambert}W\left(\frac{R_{\mathrm{S}}J_0R_{\mathrm{sh}}\exp\left(\frac{R_{\mathrm{sh}}(R_{\mathrm{S}}J_{\mathrm{SC}} + R_{\mathrm{S}}J_0 + V)}{nV_{\mathrm{th}}(R_{\mathrm{S}} + R_{\mathrm{sh}})}\right)}{nV_{\mathrm{th}}(R_{\mathrm{S}} + R_{\mathrm{sh}})}\right) \\ &- \frac{V + R_{\mathrm{sh}}(J_0 + J_{\mathrm{SC}})}{R_{\mathrm{S}} + R_{\mathrm{sh}}}, \end{aligned} \tag{4.17}$$

where $V_{\mathrm{th}} = kT_{\mathrm{module}}$ is the thermal voltage. The voltage V for a given T_{module} then correlates to J according to:

$$\begin{aligned} V(J) = &-JR_{\mathrm{S}} + (J_{\mathrm{SC}} + J_0 - J)R_{\mathrm{sh}} + \Delta V_{\mathrm{OC}} \\ &-nV_{\mathrm{th}}\mathrm{Lambert}W\left(\frac{J_0R_{\mathrm{sh}}}{nV_{\mathrm{th}}}\exp\left(\frac{(J_{\mathrm{SC}} + J_0 - J)R_{\mathrm{sh}}}{nV_{\mathrm{th}}}\right)\right). \end{aligned} \tag{4.18}$$

In Equation (4.18), a shift in voltage due to varying temperatures as introduced in Equation (4.15) is considered via $\Delta V_{\mathrm{OC}} = V_{\mathrm{OC,0}}\frac{t_{V_{\mathrm{OC}}}}{10^6}(T - T_0)$ with:

$$V_{\mathrm{OC,0}} = (J_{\mathrm{SC}} + J_0)R_{\mathrm{sh}} - nV_{\mathrm{th}}\mathrm{Lambert}W\left(\frac{J_0R_{\mathrm{sh}}}{nV_{\mathrm{th}}}\exp\left(\frac{(J_{\mathrm{SC}} + J_0)R_{\mathrm{sh}}}{nV_{\mathrm{th}}}\right)\right). \tag{4.19}$$

Ultimately, the electrics module locates the maximum power point (MPP) of the *J-V* characteristic in order to determine the power output of a solar cell:

$$P_{\mathrm{MPP}} = \max(V \cdot J)\ . \tag{4.20}$$

As already mentioned in Section 2.1.3, one important aspect for the EY of tandem solar modules under realistic irradiation conditions is the electrical configuration. The power output of tandem solar modules in the 2T configuration is limited by the lower generated current density $J_{\mathrm{MPP,top}}$ and $J_{\mathrm{MPP,bot}}$ out of the two sub-cells due to their monolithic integration:

$$P_{\mathrm{2T}} = V_{\mathrm{MPP}} \cdot \min\left(J_{\mathrm{MPP,top}}, J_{\mathrm{MPP,bot}}\right). \tag{4.21}$$

The 4T configuration, however, circumvents these current matching losses but requires a larger number of electrodes and an insulating intermediate layer. The generated power at maximum power point $P_{\mathrm{MPP,top}}$ and $P_{\mathrm{MPP,bot}}$ of both sub-cells can simply be extracted individually:

$$P_{\mathrm{4T}} = P_{\mathrm{MPP,top}} + P_{\mathrm{MPP,bot}}\,. \tag{4.22}$$

The described approach performs well for solar cell architectures that are translatable into simple equivalent circuit diagrams. More complex architectures, such as three-terminal tandem solar modules, require a numerical approach. The consistency of the described method with a numerical approach has been verified with the circuit simulation software LTspice®.

4.5 Annual energy yield calculation

Having outlined the determination of the power output for every hour of the year, the annual energy is a mere summation of P over this time frame. However, the power output at a given point in time not only depends on the irradiance spectrum, the absorptance of the device and its electrical performance, but also on the installation of the solar module and its orientation with regard to the sun's position. For this, the polar angle θ_{sun} and azimuth angle φ_{sun} of the sun's coordinates $\boldsymbol{S}$ need to be transformed into the local coordinate system of the solar module via:

$$\begin{aligned} \theta_{\mathrm{sun}} &\rightarrow \theta'_{\mathrm{sun}} \\ \varphi_{\mathrm{sun}} &\rightarrow \varphi'_{\mathrm{sun}}\,. \end{aligned} \tag{4.23}$$

This transformation into the new sun coordinates $\boldsymbol{S}'$ can be described with a quaternion $\boldsymbol{q}$ rotation about the corresponding Euler angle θ_{e} around the Euler axis, which is given by:

$$\boldsymbol{S}' = \boldsymbol{q}\boldsymbol{S}\boldsymbol{q}^{-1} \quad \text{with} \quad \boldsymbol{q} = \cos\frac{\theta_{\mathrm{e}}}{2} + \left(S_{\mathrm{x}}\boldsymbol{x} + S_{\mathrm{y}}\boldsymbol{y} + S_{\mathrm{z}}\boldsymbol{z}\right)\sin\frac{\theta_{\mathrm{e}}}{2} \tag{4.24}$$

Since direct irradiation is assumed to originate from a point-like source whereas diffuse irradiation is assumed to be distributed Lambertian [123] across the hemisphere in this model, the contributions of direct and diffuse irradiation to the J_{SC}, need to be calculated separately. The direct short-circuit current density $J_{\mathrm{SC}}^{\mathrm{dir}}$ is then obtained by integrating over the wavelength λ of the incident solar irradiation:

$$\begin{gathered} J_{\mathrm{SC}}^{\mathrm{dir}} = \frac{q}{hc}\int \chi(\lambda) A(\theta'_{\mathrm{sun}}, \lambda) I_{\mathrm{dir}}(\lambda)\lambda \cos(\theta'_{\mathrm{sun}})\, d\lambda \\ \theta'_{\mathrm{sun}} < 90° \\ \Gamma(\theta'_{\mathrm{sun}}, \varphi'_{\mathrm{sun}}) = 1\,, \end{gathered} \tag{4.25}$$

where the absorptance of the investigated sub-cell $A(\theta'_{\mathrm{sun}}, \lambda)$ and the direct irradiance $I_{\mathrm{dir}}(\lambda)$ are defined in the preceding Sections 4.2 and 4.3 and the collection efficiency χ of generated charge carriers is assumed unity. Here, the function $\Gamma(\theta'_{\mathrm{sun}}, \varphi'_{\mathrm{sun}})$ expresses all polar coordinates from which light can impinge

on the solar module ($\Gamma = 1$). Thus, light hitting the rear side of monofacial solar module is disregarded ($\Gamma = 0$), which is crucial for the calculation of the diffuse short-circuit current density $J_{\mathrm{SC}}^{\mathrm{diff}}$, in particular for tilted solar modules:

$$J_{\mathrm{SC}}^{\mathrm{diff}} = \frac{q}{hc} \iiint \chi(\lambda) A(\theta'_{\mathrm{sun}}, \lambda) I_{\mathrm{dir}}(\lambda) \lambda \Gamma(\theta', \varphi') \sin(\theta') \cos(\theta')\, d\varphi' d\theta' d\lambda\,, \qquad (4.26)$$

where q, h, c symbolize the elementary charge, the Planck constant and the speed of light. It should be noted that due to the omnidirectional nature of diffuse irradiation we integrate over both the polar and the azimuth angle.

Beyond the contributions of direct and diffuse irradiation, tilted solar modules are exposed to another contribution, namely albedo. The framework allows the consideration of this additional contribution of diffuse ground reflection $J_{\mathrm{SC}}^{\mathrm{diff,albedo}}$ for more than 3000 reflectance spectra of natural and synthetic materials analogue to Equation (4.26). The angular distribution of the diffuse albedo is also assumed Lambertian. Since the impact of albedo is not in the focus of this thesis, it is neglected throughout all investigations.

5 Light management in perovskite-based tandem photovoltaics

This chapter discusses light management in perovskite-based tandem photovoltaics at the examples of perovskite/c-Si tandem solar cells and modules as well as perovskite/CIGS tandem solar modules. At the beginning, the historical evolution of light management in perovskite-based tandem PV is reviewed representative for perovskite/c-Si tandem solar cells. However, the conclusions on the development of less absorbing transparent electrodes, selective contacts and charge transport materials can directly be transferred to perovskite/CIGS tandem PV. Furthermore, the optical loss mechanisms reflection and parasitic absorption are analyzed in detail for two representative perovskite/c-Si tandem solar cells in the 2T and 4T configuration to highlight the specific advantages and disadvantages of each configuration. The optical models used in this analysis are based on state-of-the-art architectures of 2T and 4T perovskite/c-Si tandem solar cells [26,27]. Both devices rank among the most efficient perovskite/c-Si tandem solar cells reported so far. Moreover, this chapter provides a detailed study on the impact of realistic irradiation conditions on optimal device architectures of both perovskite/c-Si and perovskite/CIGS tandem PV. Here, a special focus is directed towards the comparison of the 2T and 4T configuration of tandem devices. Additionally, a discussion on optical losses associated to inactive areas of perovskite-based tandem solar modules is provided. The role of the 2T and 4T configuration with regard to the contacting scheme is elaborated and the inactive areas are calculated exemplary for solar modules with contacting schemes based on metallic contact grids and interconnection lines.

Acknowledgements and contributions

The majority of this chapter on light management in perovskite-based tandem PV was already published Refs. [9,124]*. The perspective paper on light management in perovskite/c-Si tandem solar modules* [124] *was a collaboration between Daniel A. Jacobs from the Australian National University (ANU, Canberra) and the author. The author conducted all optical simulations of this publication and contributed the energy yield modelling under realistic conditions using the self-written EY modelling framework outlined in Chapter 4. In this thesis, several aspects have been reorganized and updated. The second publication on energy yield of perovskite/CIGS tandem solar modules is based on the same self-written EY modelling framework. The basic underlying simulations were performed by Benjamin Sautter within his master thesis, which was supervised by the author. The results were complemented by further simulations conducted by the author to advance the project to publication maturity.*

5.1 Historical evolution of light management in perovskite-based tandem photovoltaics

Owing to the fact that silicon single-junction PV closes in on its theoretical limit in terms of PCE, research dedicates huge efforts on advancing possible technologies as an add-on to conventional c-Si and CIGS PV in tandem architectures. Tandem architectures promise a higher theoretical limit in PCE of around 46 % compared to around 29 % for single-junction PV [6,7]. Auspicious candidates for the top absorber are perovskites ($E_G \approx 1.55 - 2.3$ eV), since they provide a cooperative route for the fabrication of low-cost tandem solar cells that could potentially exceed a PCE of 30%. Nevertheless, the substantially more complex tandem architecture, illustrated in **Figure 5.1**, increases the challenge to reduce the breach between actual PCE and theoretical limit. Compared to single-junction PV, tandem architectures rely on a larger number of layers to extract electric current from the absorbers and direct them to the terminals. Transparent electrodes, selective contacts, ETLs and HTLs as well as passivation layers are found among these layers. In addition, tandem architectures show an exclusive need for coupling layers: a recombination/tunnel junction for the 2T configuration or an insulating optical spacer layer for the 4T configuration. The increasing number of layers in tandem solar modules consequently entails increased optical losses, which are also depicted in **Figure 5.1**. These optical losses can be roughly classified into four categories:

(1) **Reflection losses** at either one of the many interfaces,
(2) **Parasitic absorption losses** in transparent electrodes, charge transport layers and coupling layers,
(3) **Current matching losses** due to imperfect balance of current generation between the top- and the bottom-cell, and
(4) **Inactive area losses** due to the integration of metallic contacts or monolithic interconnections.

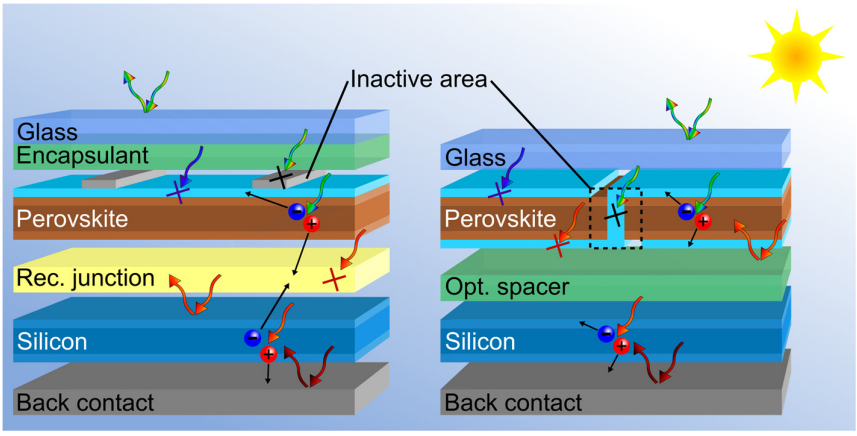

Figure 5.1: Illustration of the manifold optical losses in 2T (left) and 4T (right) perovskite/c-Si tandem solar modules. Adapted with permission from [124]. © 2019 American Chemical Society.

Before investigating the above-mentioned loss mechanisms in detail, this section provides a brief review of the past developments in the field of light management in perovskite/c-Si tandem PV with a focus on the applied deposition processes and employed materials that enabled the uprise of perovskite/c-Si tandem solar cells. **Figure 5.2** shows the historical evolution of the EQE of 2T and 4T tandem solar cells. It is evident that the improvement in the PCE of perovskite/c-Si devices over time (from yellow over orange and blue to grey) comes along with an improved optical performance as indicated by the increase in EQE. For the 2T devices in **Figure 5.2a**, the most striking observation is the poor performance in the blue part of the solar spectrum (<550 nm) compared to the 4T devices in **Figure 5.2b**. This distinct limitation of the 2T configuration originates from processing constraints imminent for the deposition of the perovskite top-cell directly on top of the c-Si bottom-cell. When using the c-Si bottom-cell as the substrate, the charge transport layer and

electrode at the front side of the perovskite solar cell are the last in the fabrication sequence. This circumstance constraints the process conditions for the deposition of these layers to low temperature processes, the use of compatible solvents and in some cases even the integration of protective buffer layers [125,126]. Consequently, it remains a severe challenge to achieve highly transmissive front-side layers for 2T perovskite/c-Si solar cells, while still preserving low sheet resistivity of these layers. A suitable example for the reduction of parasitic absorption in the blue part of the spectrum is the replacement of poorly performing Spiro-OMeTAD (2,2',7,7'-tetrakis(*N,N*-di-4-methoxyphenylamino)-9,9'-spirobifluorene) HTL, which accounts for losses in current density of up to 2.7 mA cm^{-2} [127], by the evaporation of very thin front-side CTLs [27,126]. In contrast, 4T devices sidestep any processing constraints since mechanical stacking allows an independent fabrication of the two sub-cells. Therefore, high quality front TCOs, such as indium-doped tin oxide (ITO) or fluorine-doped tin oxide (FTO), and ETLs, such as mesoporous TiO_2, compact TiO_2 or compact SnO_2, are within reach. Since all of these materials absorb hardly in the UV range, the UV response of 4T devices is inherently outperforming that of 2T devices.

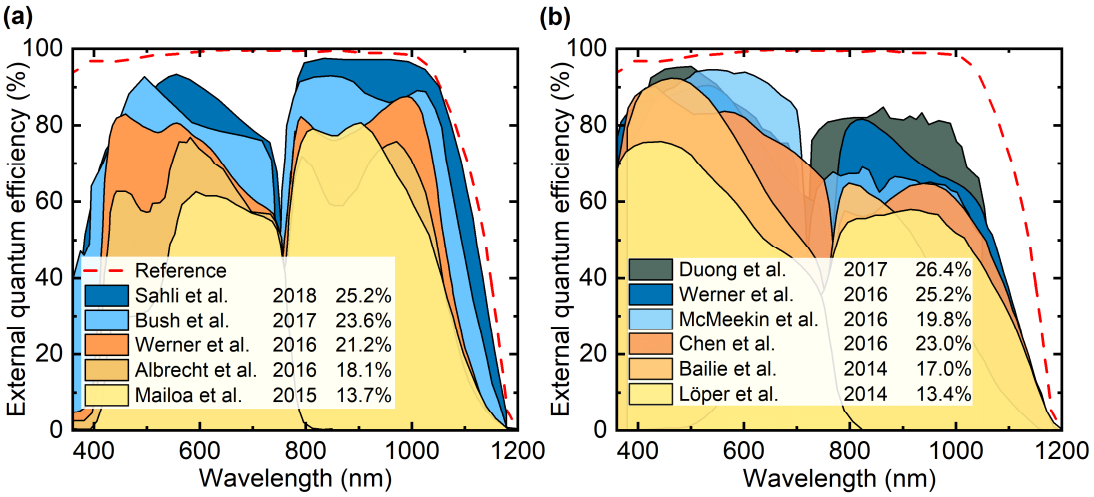

Figure 5.2: Evolution of the EQEs of laboratory-scale (a) 2T perovskite/c-Si tandem solar cells [27,126,128–130] and (b) 4T perovskite/c-Si tandem solar cells [12,26,69,131–133]. Additionally, the published EQE of the c-Si single-junction solar cell with the highest certified J_{SC} to date is shown as a reference [134]. For reasons of clarity, further recent results are left out [28–31]. Adapted with permission from [124]. © 2019 American Chemical Society.

Nevertheless, the optical coupling layers and the larger number of electrodes required by the 4T configuration become noticeable, when taking a closer look to EQE in the near-infrared (NIR). For a long time, the NIR-EQE of the 4T devices was limited to values of maximum 80 % due to parasitic absorption induced by the additional layers [26,29]. Only recently, the employment of advanced light management textures and index matching liquids allowed to overcome this value [28]. In this spectral range, there is apparently still a tremendous potential for improvement, in particular when comparing the NIR-EQE of 4T devices to that of 2T devices. The latter have the advantage of not requiring additional electrodes or optical adhesives in between the two sub-cells but only weakly absorbing recombination or tunneling junctions. Consequently, in the NIR, the EQE of the 2T perovskite/c-Si tandem solar cell of Ref. [27] is remarkably close to the EQE of the reference c-Si single-junction solar cell. This achievement, however, is not only attributable to reduced parasitic absorption but is also a result of improved light incoupling and light trapping by the use of texturing.

In particular, exploiting the random pyramid texture obtained from anisotropic wet-etching of the Si wafer's surface is very attractive from an optical point of view since the texture simultaneously reduces the device's reflection and increases light trapping in the c-Si bottom-cell. Due to the independent fabrication of top- and bottom-cell in 4T devices, the texture of c-Si bottom-cells does not constrain the fabrication of the

perovskite top-cell and has become a common feature of 4T perovskite/c-Si tandem solar cells [12,26,131,132]. However, textures have only recently been successfully employed in 2T devices, which resulted in the above-mentioned exceptional NIR-EQE of the fully-textured 2T perovskite/c-Si solar cell of Ref. [27].

In the following sections, this work provides a detailed discussion of techniques and challenges associated to the four optical loss mechanisms outlined above. For the discussion on reflection and parasitic absorption losses, two optical models of representative state-of-the-art 2T and 4T perovskite/c-Si tandem solar cells are established [26,27]. Both models are calibrated with regard to the experimentally measured EQE (see **Figure 5.3**). It should be pointed out that even though these discussions primarily handle perovskite/c-Si tandem PV, they are also applicable to all thin-film perovskite/perovskite and perovskite/CIGS tandem architectures. To highlight this aspect, the part on current matching losses and on the question about the superior configuration includes both perovskite/CIGS and perovskite/c-Si tandem solar modules.

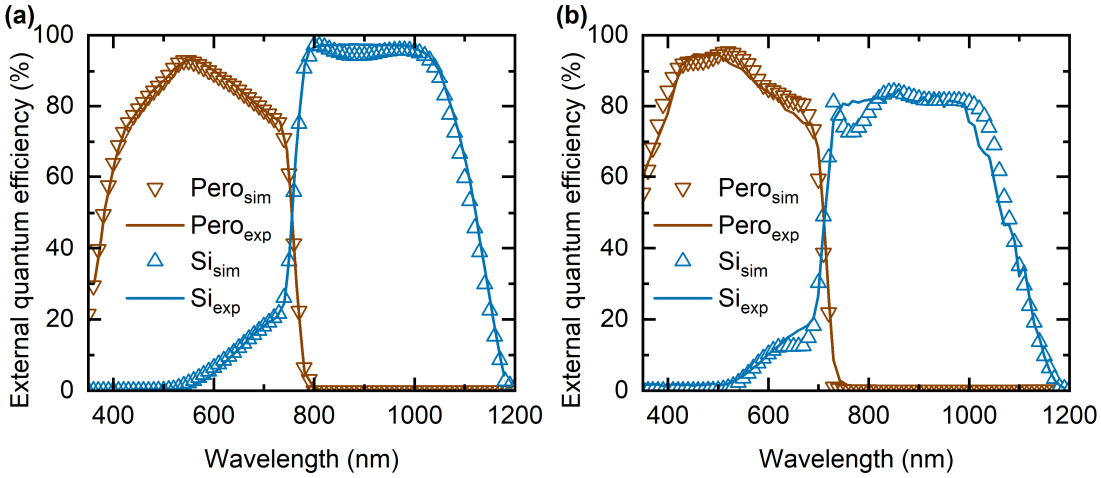

Figure 5.3: Comparison of the experimentally measured EQE of state-of-the-art perovskite/c-Si tandem solar cells in the 2T and 4T configuration from references [26,27] and the calculated EQE of the respective optical models developed within the self-written EY modelling framework outlined in Chapter 4.

5.2 Reflection losses

Maintaining low solar-weighted reflection is a crucial requirement for PV devices in general, but has an even higher importance for tandem solar cells due to their complex architectures. The reduction of reflection losses via texturing is well established in Si single-junction PV [134]. Additionally, textures applied to the front surface of the protective cover glass of solar modules via light management foils or texturing of the glass itself represents an interesting alternative to textured Si wafers [28,91,135–141]. Therefore, the role of texturing in the reduction of reflection of perovskite/c-Si tandem solar cells and modules is discussed. A special focus here lies on the two investigated electrical configuration of the tandem devices, 2T and 4T.

In contrast to current 4T record devices [26], light management is a particularly complex matter for 2T configurations [27], since the fabrication of a complex monolithic architecture introduces several processing constraints as outlined above. Commercial single-junction c-Si solar cells typically employ random pyramids with a dimension of ~1-5 µm, which minimize front-side reflection resulting in an EQE exceeding 97 % [134]. Light reflected on the first contact with a pyramid's facets is redirected to the facets of a second pyramid. Thus, the overall solar-weighted reflectance at normal incidence nearly vanishes due to the pyramidal texture. These pyramids are usually obtained via anisotropic wet etching of the Si wafers [142]. However, solution-processing of perovskite solar cells directly on top of a textured c-Si solar cell represents a severe

technological challenge. The only processing technique capable of depositing conformal layers on pyramidal textures of these dimensions is a hybrid evaporation–solution process technique [27]. A full co-evaporation process stands out as an interesting alternative since it relies on a lower number of process steps and achieves large-area films with a superior homogeneity than the hybrid process. However, further research is required to advance the maturity this technique [143]. The large amount of research effort invested into the conformal coating of c-Si solar cells with a high-quality perovskite layer naturally raises the question: is texturing of the c-Si bottom-cell necessary and, if yes, how many textures need to be employed? Architectures employing c-Si absorbers with a polished front side and a textured rear side increase the number of viable processing techniques for the perovskite top-cell and enables, in particular, the inexpensive solution-processing of high-quality perovskite films directly on top of a c-Si solar cell substrate. Even though these architectures are optically inferior, the devices with a rear texture exhibit PCEs comparable to that of fully textured architectures due to the superior electrical characteristic of the perovskite top-cell [28,128,131,144].

To quantify the difference in current generation between 2T perovskite/c-Si solar cells with a rear texture and those with a double-side texture from an optical point of view, simulations of architectures based on Ref. [27] employing various textures in the cell and the module environment were performed. The investigated architectures span across a bare perovskite/c-Si tandem solar cell (architecture I) and modules (architectures II–IV) encapsulated with ethylene vinyl acetate (EVA) and a cover glass with an anti-reflection coating (ARC). Contrary to the planar cover glass employed in architecture II, architectures III and IV employ cover glass with a textured front side, which is supposed to take on the anti-reflective and light-trapping role of the texture on the front side of the Si absorber. However, deeply-textured cover glass is not yet established in the market on a large scale due to the small benefit to already textured single-junction c-Si solar cells [145]. For 2T perovskite/c-Si devices, however, textured glass poses a viable alternative to front-side texturing of the c-Si absorber. It enables the application of solution-processing, while it optically performs like polymeric light management (LM) foils attached to the front side of solar modules [91]. In realistic outdoor conditions, textured glass has the advantage of not being afflicted with the reliability concern that polymeric materials suffer from [146,147].

Figure 5.4 shows the total absorbed current density (perovskite + c-Si) of the four investigated architectures. The largest difference between a rear textured and a double-side textured c-Si absorber is evident for the cell architecture I (∼1.9 mA cm^{-2}). In the absence of windows layers, that smooth the transition of refractive indices towards the absorber layers, this unencapsulated architecture exclusively relies on light management textures. Moving from the bare cell to an encapsulated environment (architecture II) supports light incoupling. Thus, the discrepancy between a planar and a textured c-Si front surface reduces to ∼1.7 mA cm^{-2}. Apart from its anti-reflective properties, textured glass exhibits the additional benefit of improving the light trapping behavior drastically. The benefit is more pronounced for the case of a rear texture than for the case of a double-side texture, which already inherits good light trapping from its textured front surface. Thus, the benefit of front-side texturing reduces to only ∼1.4 mA cm^{-2}. Assuming that either durable LM foils or reasonably priced textured cover glass are available, it seems that both rear textured and double-side textured c-Si bottom cells are a worthwhile option for 2T perovskite/c-Si tandem solar cells and modules.

Pushing 2T devices beyond the ∼1.4 mA cm^{-2} absorption deficit is only feasible at the cost of increasing the complexity of the layer sequence. In particular, the EVA/TCO interface and the interface between the perovskite top-cell and the c-Si bottom-cell are the most reflective interfaces in the investigated 2T configuration. A simple coating with an ARC on top of the TCO poses a simple solution for the first interface. Here, $SiO_{0.4}N_{0.6}$ is a possible ARC because it has a refractive index of around 1.75, which is in between those of EVA (∼1.5) and indium zinc oxide (IZO; n∼2.2) [148]. Interlayers at the second interface interrupt the cell structure substantially. Consequently, the requirement for a highly conductive and transparent material with

a suitable refractive index narrows down the search for suitable materials considerably. Recently, the interest in the index-tunable SiO_x increased in the context of reducing reflection losses at this interface [149]. Employing interlayers at both discussed interfaces in architecture IV increases the overall absorbed current density of the rear-textured device by ~1.2 mA cm^{-2} and the discrepancy with regard to the device with a double-side texture reduces to only 0.3 mA cm^{-2}. It is noteworthy that these interlayers have been considered non-absorbing. Consequently, this value only serves as a benchmark for ideal interlayers. It should be pointed out that the identified increase of ~1.2 mA cm^{-2} is significantly smaller than reference [149], which investigated bare solar cells instead of solar cells in a module environment. As indicated above, the encapsulant and glass window layers play an important role when assessing the optical performance in photovoltaics.

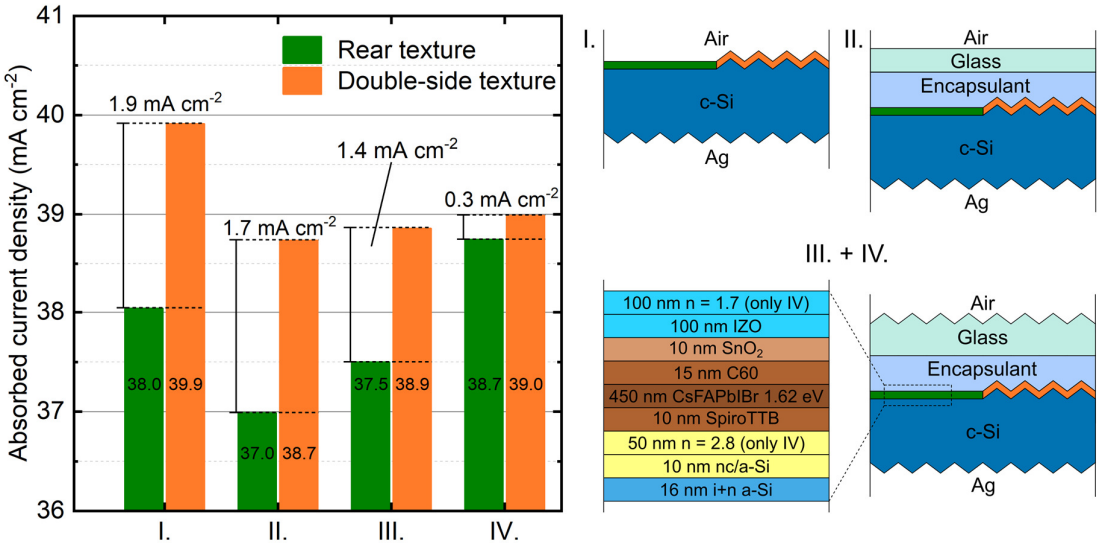

Figure 5.4: Quantification of the total absorbed current density of 2T perovskite/c-Si tandem devices employing either a rear texture or a double-side texture in dependence of the cells environment. The optical impact of front-side texturing is shown for four different architectures: (I) a bare lab-scale device without encapsulation, (II) a module consisting of a cell encapsulated behind EVA and a planar cover glass, (III) a module employing a textured cover glass and (IV) a module with a textured cover glass and additional interlayers. All architectures (II-IV) additionally exhibit an antireflection coating (100 nm MgF_2; $n \approx 1.37$) either directly on top of the cell (I) or on top of the cover glass (II-IV). Adapted with permission from [124]. © 2019 American Chemical Society.

5.3 Parasitic absorption

Beside the relevance of the above-discussed consideration of reflection losses, the reduction of losses due to parasitic absorption also plays an important role in optimizing the optical performance of a perovskite/c-Si tandem solar cell. These losses occur in most of the many layers of the device architecture and, thus, the minimization of them is a multi-faceted challenge. In fact, parasitic absorption losses are substantially more significant compared to reflection losses. Simulations of two different architectures of state-of-art perovskite/c-Si tandem solar cells in the 2T [27] and the 4T [26] configuration confirm this statement. Here, the 2T device, which is adopted from the first reported fully-textured monolithically-stacked perovskite/c-Si device, is calculated once as-is and once with a planar front side. It should be noted that the following analysis is conducted with two representative architectures and the derived conclusions are also valid for other devices employing similar materials and architectures.

For both architectures of the 2T device, as well as for the 4T device, the reflection losses are constantly lower than the total current density losses associated to parasitic absorption as shown in **Figure 5.5**. For the

solar cell with double-side texture, the parasitic absorption loss in some layers even outweighs the reflection losses. The most noticeable offenders in terms of parasitic absorption are the TCOs, the CTLs, the optical coupling layer in the 4T configuration and to a small extent the metallic back contacts. The 2T configuration suffers mostly from parasitic absorption in the front-side ETL (C_{60}) of the perovskite top-cell with a current density loss of ~1 mA cm^{-2}, even though this layer with a thickness of only 15–20 nm is relatively thin. Nonetheless, this already marks an improvement compared to early designs employing Spiro-OMeTAD as outlined in the introduction of this section [127,128]. A further reduction of the layer thickness of C_{60}, while maintaining a conformal and pinhole-free layer at the same time, represents a technological challenge that might be achievable via evaporation techniques. Theoretically, a layer thickness of 1 nm is enough to build a selective contact [150]. The other IZO and MgF_2 layers could potentially be optimized in the same way or replaced entirely by superior materials as discussed in the following. An interesting aspect, in particular in the comparison between the 2T and 4T configuration, is the fact that the parasitic absorption in the nc/a-Si:H recombination junction of the 2T device is close to vanishing [151]. Earlier prototypes made use of ITO as a recombination junction, which resulted in current density losses of up to 1 mA cm^{-2} [127]. Alternative to a nc/a-Si:H recombination junction, interlayer-free 2T configurations are recently emerging, which could potentially circumvent the issue of parasitic absorption in the recombination junction entirely [152,153].

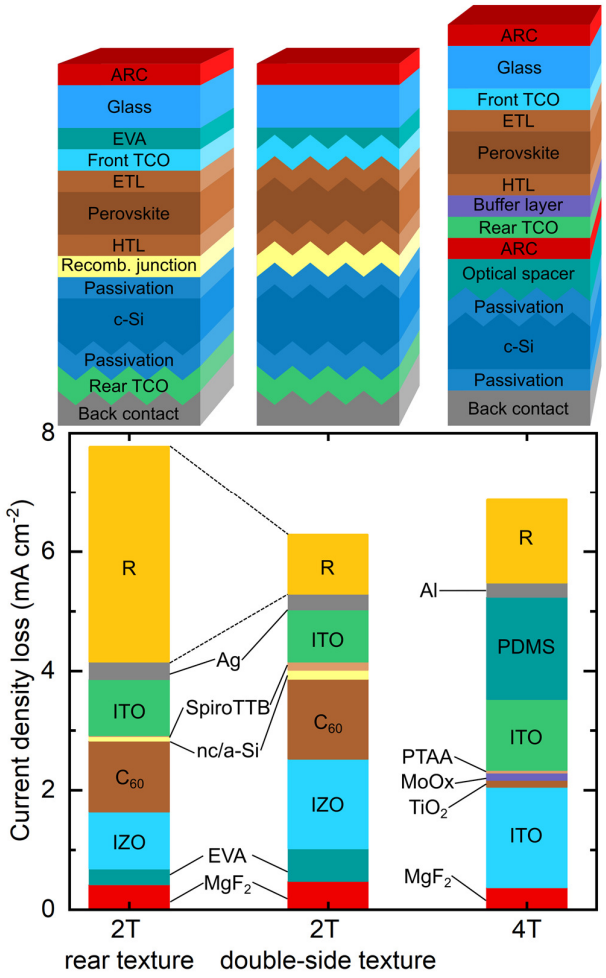

Figure 5.5: Illustration of the manifold optical losses in 2T (left) and 4T (right) perovskite/c-Si tandem solar modules. The models of the 2T device with a double-side texture and the 4T device are calibrated with regard to their respective EQE and $(1 - R)$ data. Data for reflection losses is shown without the contribution of escape reflection due to incomplete light trapping in the Si absorber. Reprinted with permission from [124]. © 2019 American Chemical Society.

Owing to the relaxed processing constraints for the front-side TCO and CTL in the 4T configuration, parasitic absorption losses in these layers are relatively small. The modelled state-of-the-art 4T device employs optically superior charge transport layers – a combination of compact and mesoporous TiO_2 with a high optical quality on the front side and a thin layer of poly[bis(4-phenyl)(2,4,6-trimethylphenyl)amine (PTAA) on the rear side – compared to the modelled 2T device. On the downside of this architecture is the absorption in the polydimethylsiloxane (PDMS) coupling layer of ∼1.5 mA cm^{-2}, which is relatively large compared to that of the nc/a-Si:H recombination junction of the 2T device. This loss, which occurs predominantly in the NIR, can be attributed to the molecular vibration of the polymer's CH group [154]. Nevertheless, reducing the thickness of this layer from the current ∼1.5 mm to more conventional encapsulation thickness of ∼300 µm should suffice to reclaim a major share of the loss in current density.

In general, this analysis demonstrates that the majority of parasitic absorption losses originate from the TCOs, which sum up to >1 mA cm^{-2} for the 2T configuration and are even close to 3 mA cm^{-2} for the 4T configuration. A recent review gathered a variety of superior TCO materials and alternative deposition techniques [155], which is illustrated in **Figure 5.6**. The materials are identified in terms of their sheet resistance and average AM1.5G-weighted absorption. Owing to their compatibility with low-temperature processing (<150 °C), all shown materials are suitable for either deposition as the front electrode of the perovskite top-cell in the 2T configuration or both as front and rear electrode in the 4T configuration. For the latter, it is apparent that both sputtering hydrogenated indium tungsten oxide (IWO:H) and hydrogenated indium oxide (IO:H) results in TCOs with significantly lower AM1.5G-averaged absorption than any other suitable TCO. This provides a good indication that there is still potential for further development of TCOs for tandem PV.

The discussion about the impact of TCOs on the solar cell performance just appears straightforward at the first glance. In reality, the electrodes are critically affected by the solar cell dimension and the presence of a metal grid. Here, it is necessary to distinguish between the 2T and 4T configuration. Since the perovskite top-cell is processed directly on top of a c-Si solar cell in the 2T configuration, the tandem device inherits its dimension from the c-Si wafers (currently 239 mm^2) and its contacting scheme from the c-Si bottom-cell. Consequently, the 2T configuration would be contacted with a metallic finger grid on top of the front TCO, in the same way as c-Si single-junction solar cells. In the 4T configuration, however, the independent cell fabrication and contacting enables the monolithic interconnection of the thin-film perovskite top-cell via narrow cell stripes (∼5 mm). This approach circumvents a front-side metallization required for the lateral charge transport across an entire c-Si wafer. In contrast to the metallized front electrode in a 2T device, the front electrode in a 4T device is just a bare TCO. In the 4T configuration, the rear electrode of the perovskite top-cell is last in the processing sequence and the same processing constraints apply as for the front electrode of a 2T device. Therefore, the rear electrode is also a candidate for the complementation by a metal grid [156].

Figure 5.6 shows the effect of implementing optimally spaced 50 µm-wide metal fingers on the sheet resistance and AM1.5G-averaged optical losses [157]. The bare TCO data from reference [155] serve as a starting point. This calculation is subject to three underlying assumptions. Firstly, the maximum factor by which the TCO thickness can be reduced from its original value does not exceed a factor of up to ∼4, which results in minimal final layer thicknesses of around 50 nm. Secondly, the amount of parasitic absorption in the TCO scales proportionally with its layer thickness. Thirdly, the spacing of the metal fingers and the TCO thickness are optimized for a charge transport over a distance of 2.5 cm, which is derived from a configuration of a 156 mm wafer with three bus bars. Furthermore, the invariant contributions of bus bar shading and resistive losses in the metal fingers are disregarded. The apparent trends towards improved sheet resistance and optical losses highlight that the differences in TCO performance fade once metallization is considered. The TCO materials can be tuned for high optical transparency by smaller thicknesses, while the metal grid contributes to a reduction of the sheet resistance. Nonetheless, the choice of TCO material

and deposition technique is of highest importance once a bare TCO is required as an electrode, in particular for the front electrode of the perovskite top-cell in the 4T configuration.

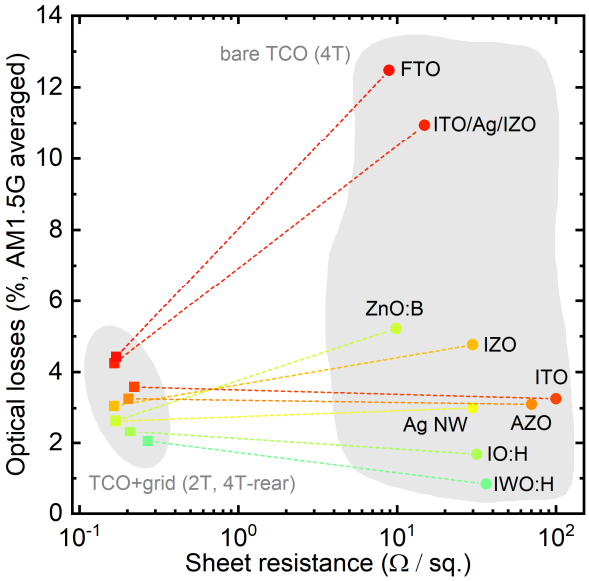

Figure 5.6: Illustration of the effect of metallization on the performance of a variety of TCO materials in terms of sheet resistance and AM1.5G-averaged optical losses both by shading and parasitic absorption in the TCO (data mostly adapted from [155]). Reprinted with permission from [124]. © 2019 American Chemical Society.

5.4 Current matching and optimal perovskite bandgap

Beyond the optimization of the auxiliary layers and textures discussed in the previous section, light management in perovskite-based tandem photovoltaics is primarily a matter of the optimization of the absorber layers themselves. In particular, current matching in the 2T configuration is critically affected by the optical absorption of the perovskite top-cell and, thus, by two important parameters: (1) the perovskite bandgap and (2) the perovskite thickness. A balanced current generation of the two sub-cells is key to maximize the power output of 2T devices. Contrary to the investigation of optical losses originating from parasitic absorption and reflection, current matching losses cannot be assessed well under the assumption of standard test conditions (STC: AM1.5G irradiation at normal incidence and 25°C). STC define a constant spectrum and poorly reflect the constantly changing environmental conditions solar modules are exposed to in a realistic setting. A more accurate approach to evaluate the impact of absorber properties on the performance of tandem solar modules is energy yield (EY) modelling. It considers the many aspects of realistic irradiation, such as location-specific ratio of diffuse versus direct irradiance, temporal changes in the irradiation spectrum and the orientation of the sun with respect to the solar module and many more [9,23–25,107]. Building up on the previous sections, this section provides a brief discussion of the optimal perovskite bandgap in perovskite/c-Si tandem solar modules. Additionally, a detailed analysis of various characteristics of realistic irradiation conditions on the optimal device architecture is given for the example of the very similar perovskite/CIGS tandem technology and the conclusions are discussed in the context of perovskite/c-Si tandem PV. These irradiation characteristics encompass: (1) climatic conditions, (2) ratio of specular versus diffuse irradiance, and (3) location-specific spectral distribution. Due to the similar bandgaps of Si and CIGS, most of the conclusions are also applicable to perovskite/c-Si PV. The methodology of the applied EY modelling framework is described in detail in Chapter 4.

Optimal bandgap – STC versus realistic conditions

To begin with, the impact of realistic irradiation conditions on optimal device parameters, in particular the perovskite bandgap, are investigated. For this, the nominal power under STC and the EY for two representative locations – Phoenix (Arizona) with a large share of direct irradiation and Portland (Oregon) with a large share of diffuse irradiation – of the aforementioned state-of-the-art architectures of references [26,27] are analyzed. In both cases, the architectures, sketched in **Figure 5.5**, are on one hand calculated as reported in literature and on the other hand with optimized perovskite bandgap and layer thickness. To avoid any ambiguous or biased impact of electrical properties on this investigation, the FF (~78 %) and the V_{OC}/E_G ratio are kept constant. Additionally, the maximum perovskite thickness is limited to 750 nm in order to remain within a realistic thickness range of solution-processed perovskite layers.

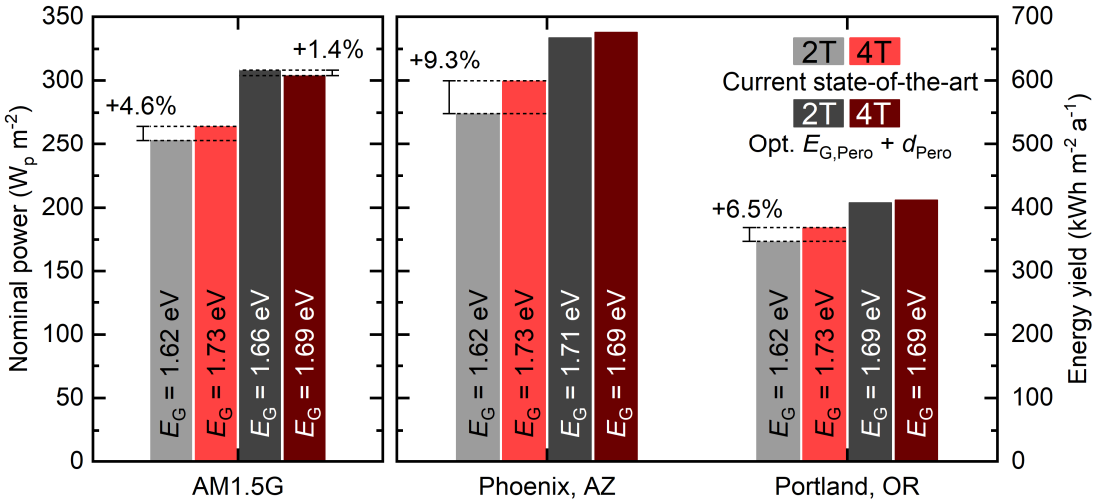

Figure 5.7: Nominal power output under STC (left) and realistic annual energy yield (right) of the 2T [27] and 4T [26] perovskite/c-Si tandem solar cells investigated throughout this section in two representative locations. For each location and architecture, an optimum tilt angle is used. The energy yield (EY) of the devices is once calculated as reported in literature (light gray and light red) and once with optimized perovskite bandgap and thickness (dark gray and dark red). The relative difference in nominal power and EY are indicated with labels. Adapted with permission from [124]. © 2019 American Chemical Society.

Modelling of the nominal power under STC and the EY under realistic conditions reveals several insights into the role of optical losses for the optimal perovskite bandgap. Starting from the idealized assumption of a step-function absorption and the absence of parasitic absorption, the ideal bandgap of the perovskite top-cell in the 2T configuration is well-known to be located in the energy range of 1.7–1.8 eV [8,21]. Nevertheless, this assumption is very different from the absorption of realistic materials. In addition, parasitic absorption in the auxiliary layers necessitates further corrections to this idealized approximation. As discussed in Section 5.3, the vast majority of parasitic absorption in the 2T configuration occurs in the window layers of the perovskite top-cell. Consequently, the optimal perovskite bandgap decreases with respect to the architecture without parasitic absorption. Furthermore, incomplete absorption of light in the perovskite top-cell intensifies the trend towards lower optimal perovskite bandgaps. This effect originates from the finite thickness of the perovskite absorber and the fact that its absorption profile naturally deviates from a step function profile. These considerations are reflected in the optimal perovskite bandgaps of 1.66 eV for both the 2T and 4T configurations under STC (see **Figure 5.7**). In contrast, the optimal perovskite bandgap under realistic irradiation conditions rebounds to slightly higher values of 1.69–1.71 eV for both configurations. An interesting side note of **Figure 5.5** is that the 2T configuration benefits strongly from a device optimization for realistic irradiation conditions, contrary to the 4T configuration, which does not suffer from current

matching losses. Nonetheless, the increasing trend in optimal perovskite bandgap indicates that the properties of the impinging irradiance play an important and non-negligible role in the evaluation of optimal device parameters for perovskite-based tandem solar modules.

Impact of irradiation characteristics

In the following, the role of various characteristics of realistic irradiation conditions on the annual energy is investigated in detail for representative all thin-film perovskite/CIGS tandem solar modules. Furthermore, the optimal perovskite bandgap and perovskite thickness for various locations are identified. The extent to which the results presented below are applicable to perovskite/c-Si tandem solar modules is explained in the corresponding sections of the text.

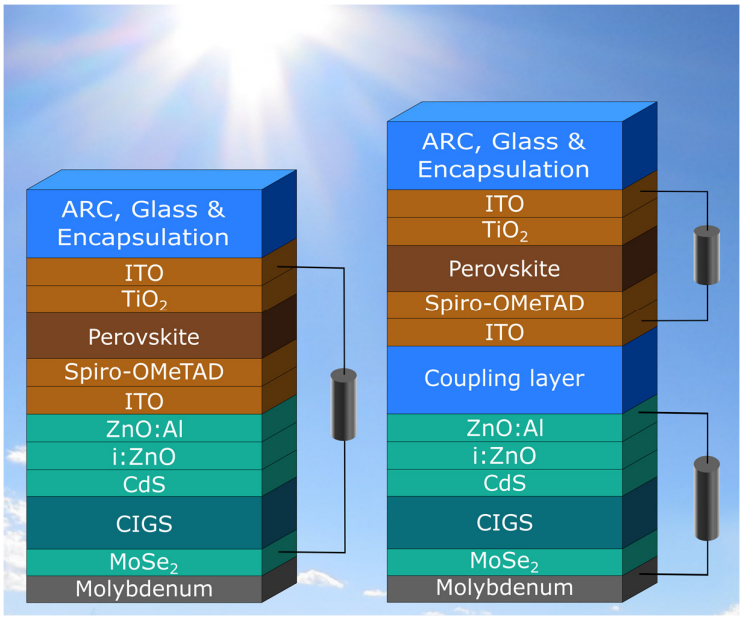

Figure 5.8: Schematic of the architecture of the virtually stacked 2T (left) and 4T (right) perovskite/CIGS tandem solar modules. The individual sub-cells are derived from references [158,159]. A summary of the layer thicknesses can be found in the Supporting Information of reference [9]. Adapted with permission from [9]. © John Wiley & Sons, Ltd.

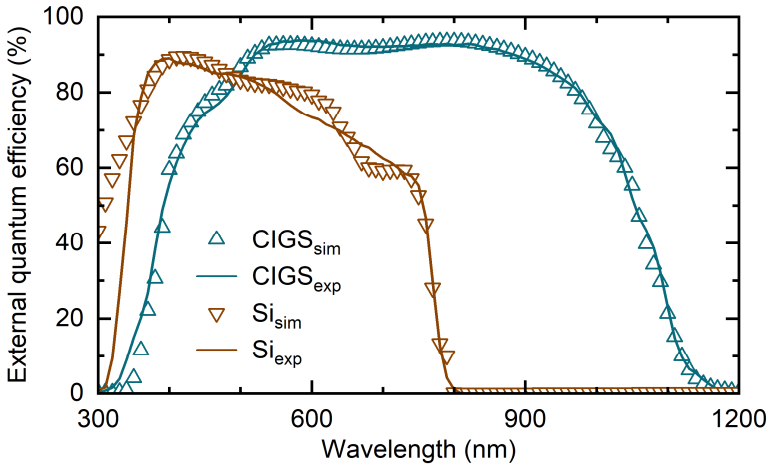

Figure 5.9: Comparison of the experimentally measured EQE of state-of-the-art CIGS and perovskite solar cells from references [158,159] and the calculated EQE of the optical models. Adapted with permission from [9]. © John Wiley & Sons, Ltd.

For the following examination, we exploit virtually stacked architectures of planar 2T and 4T perovskite/CIGS tandem solar modules, which are illustrated in **Figure 5.8**. The optical models of the individual sub-cells are calibrated with regard to the EQE of a perovskite single-junction solar cell of Ref. [158] and a CIGS single-junction solar cell of Ref. [159] (see **Figure 5.9**). A detailed summary of the layer thicknesses is available in the Supporting Information of the corresponding reference [9]. The major difference in architecture between the two configurations is the thickness of the rear ITO layer that acts as the rear electrode (thickness: 120 nm) in the 4T device and as the recombination junction (thickness: 30 nm) in the 2T device. Apart from the differing thickness and purpose of the rear ITO, both perovskite sub-cells consist of an ITO front electrode, a TiO_2 ETL, the perovskite absorber, a Spiro-OMeTAD HTL. For the following evaluation of the impact of irradiation conditions on the optimal device parameters of perovskite/CIGS tandem solar modules, methyl ammonium lead iodide ($CH_3NH_3PbI_3$) is used as a starting material for the absorber since it is commonly considered as a reference material. Furthermore, it exhibits similar optical properties compared to high-performance perovskite absorbers with a closely related stoichiometric composition [160]. In the modelled devices, the poorly temperature-stable Spiro-OMeTAD and perovskite limits the annealing temperatures of the ITO layers, which may result in increased parasitic absorption as discussed in Section 5.3. However, these processing constraints are neglected in the model. From an optical point of view, the choice of the HTL in this architecture is of subordinate nature as confirmed by simulations employing nickel oxide (NiO_x) as HTL [9]. An EVA optical coupling layer separates the sub-cells of the 4T device. The CIGS bottom-cells are composed of a molybdenum (Mo) rear contact, a molybdenum diselenide ($MoSe_2$) layer just below the CIGS absorber with a bandgap of 1.2 eV, a cadmium sulfide (CdS) buffer layer, and a front electrode consisting of an intrinsic zinc oxide (i-ZnO) and an aluminum-doped zinc oxide (ZnO:Al) layer. It should be noted that any shadowing of electrical interconnections is disregarded.

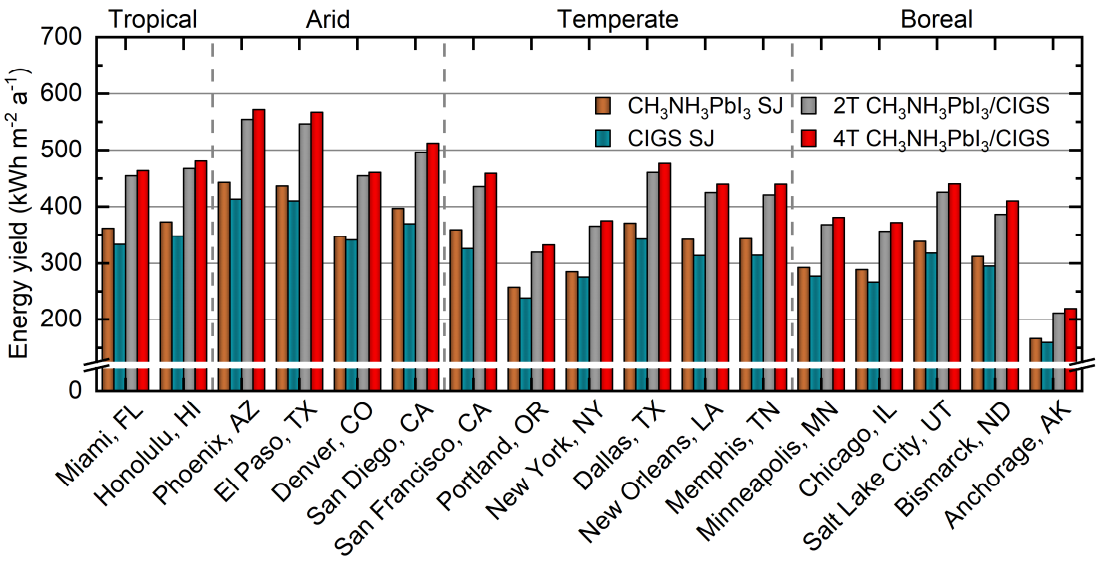

Figure 5.10: Overview of the EY of an opaque $CH_3NH_3PbI_3$ SJ (brown), an opaque CIGS SJ (teal) and $CH_3NH_3PbI_3$/CIGS tandem solar modules in the 2T (gray) and 4T (red) configuration in various locations in the United States of America. The tandem solar modules are optimized for each location individually with a maximum perovskite thickness of 1000 nm. The specific locations are sorted by the first order of their corresponding Köppen climate classification [161]. Adapted with permission from [9]. © John Wiley & Sons, Ltd.

One obvious environmental aspect that could potentially influence the optimal device parameters of perovskite/CIGS tandem solar modules is the prevalent climatic condition at a specific location. For this reason, a variety of locations in the United States of America covering a broad range of climatic zones is studied. An overview of the EY of an opaque single-junction (SJ) $CH_3NH_3PbI_3$ (brown), an opaque CIGS SJ

(teal) and $CH_3NH_3PbI_3$/CIGS tandem solar modules in the 2T (gray) and 4T (red) configuration is provided in **Figure 5.10**. The tandem devices are optimized in terms of layer thickness in each location. The investigated locations are sorted by the first order of their Köppen climate classification, which categorizes tropical, arid, temperate and boreal climate zones [161]. The results of this overview show that the relative difference in performance between the 2T and 4T configurations hardly varies in between the individual locations and amount to ~3.5 % relative. A strong impact of climatic conditions on current matching losses, which should be observable in the relative performance of 2T and 4T devices, can thus be ruled out. It becomes evident that the same conclusion applies to perovskite/c-Si tandem PV, when recalling the comparable relative performance of 2T and 4T perovskite/c-Si tandem solar modules for two representative locations in very different climatic zones shown in **Figure 5.7**.

Having eliminated climatic conditions as a key parameter for current matching in 2T tandem solar modules, irradiation properties such as the ratio of specular versus diffuse irradiance and the location-specific spectral distribution come into focus. A convenient figure-of-merit for the latter is the average photon energy (APE), which is defined as the average energy of photons that are incident at a certain location over the period of one year. To identify the impact of the irradiation properties on current matching in 2T devices, four archetypal scenarios are required as summarized in **Figure 5.11**:

(1) *Phoenix Real Spectra*: the real measured spectra of the representative location of Phoenix (Arizona);
(2) *Phoenix Invariant Spectra*: a scenario that adapts the varying levels of specular and diffuse irradiation but displays an invariant APE by constantly employing an AM1.5G spectrum scaled to the measured intensity at every point in time;
(3) *Phoenix all* I_{specular}: the real measured spectra assuming all irradiation is specular;
(4) *Phoenix all* I_{diffuse}: the real measured spectra assuming all irradiation is diffuse.

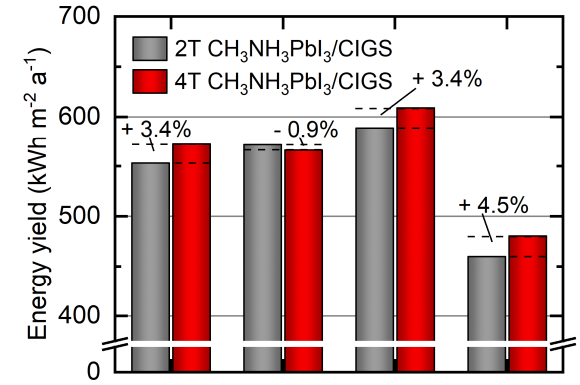

	Phoenix Real Spectra	*Phoenix Invariant Spectra*	*Phoenix all* I_{specular}	*Phoenix all* I_{diffuse}
Invariant *APE*	No	Yes (AM1.5g)	No	No
Fraction of I_{specular}	Varying	Varying	1	0
Fraction of I_{diffuse}	Varying	Varying	0	1

Figure 5.11: Comparison of the EY of perovskite/CIGS tandem solar modules in the 2T (gray) and 4T (red) configuration for four irradiation scenarios. Each irradiation scenario displays a unique characteristic as summarized in the lower table. The corresponding irradiation spectra can be found in the Supporting Information of reference [9]. Adapted with permission from [9]. © John Wiley & Sons, Ltd.

The corresponding irradiation spectra can be found in the Supporting Information of reference [9]. It should be pointed out that no scenario-specific optimization of the devices in terms of layer thickness is performed, which permits a fair comparison of current matching losses between all scenarios.

Starting from the reference scenario *Phoenix Real Spectra*, it is evident that relative difference between the EY of the 2T and 4T device in the scenarios *Phoenix all* I_{specular} and *Phoenix all* I_{diffuse} hardly differs from the reference. In the scenario *Phoenix Invariant Spectra*, however, the trend in relative difference in EY reverses and even favors the 2T device. This observation allows the conclusion that transient variations in the spectral irradiation predominantly affect current matching. The ratio of specular versus diffuse irradiance is of lower importance. Here, the module encapsulation with a typical refractive index of 1.45–1.5 diminishes the relevance of the angle of incidence by limiting the conical solid angle of incident light acceptance on the solar cell to ~40–45°. For this reason, the relative performance of 2T and 4T perovskite/c-Si tandem solar modules is also mainly affected by transient variations in the spectral irradiation and the ratio of specular versus irradiance is of minor relevance. In general, the dominant role of the APE results in the need of a more location-specific rather than climate-specific optimization of perovskite-based tandem solar modules.

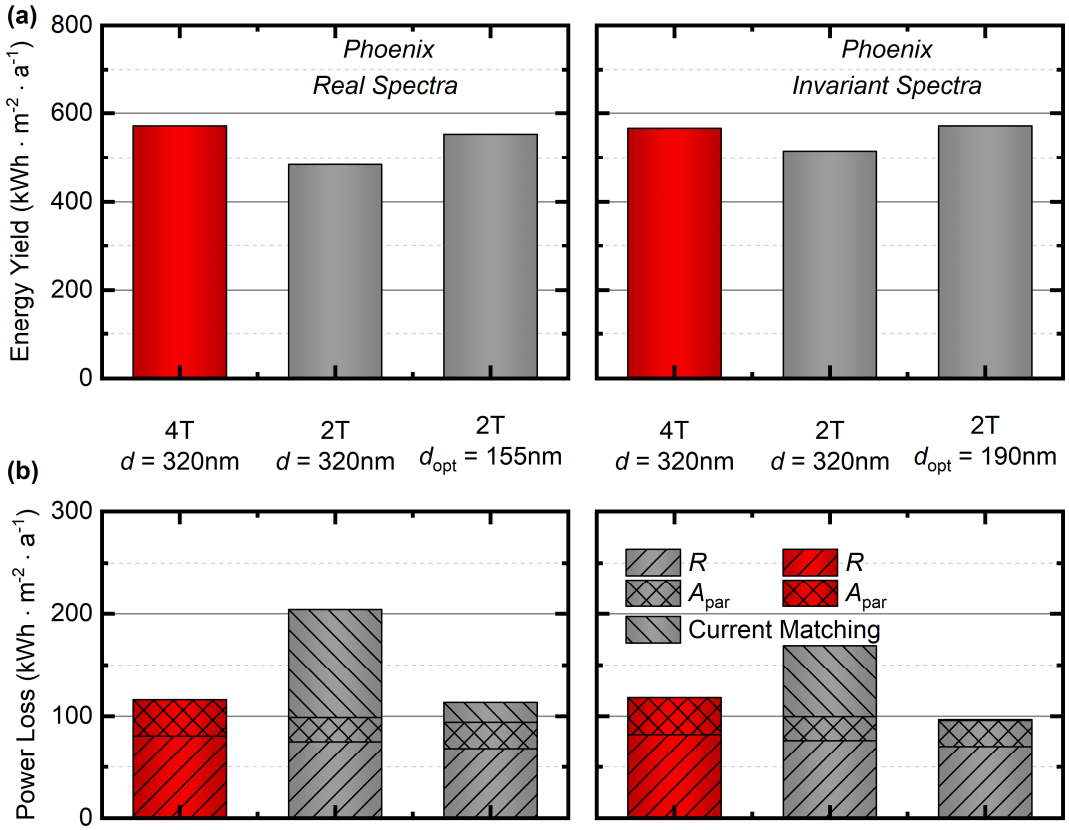

Figure 5.12: (a) Quantification of the annual EY of latitude-tilted perovskite/CIGS tandem solar modules in two different irradiation scenarios as defined in **Figure 5.11**. The 2T devices are once displayed with the same perovskite thickness as the 4T device and once optimized for each scenario individually. (b) Comparison of the power losses associated to reflection, parasitic absorption and current matching. The applied methodology for the quantification of the power loss can be found in the Supporting Information of reference [9]. Adapted with permission from [9]. © John Wiley & Sons, Ltd.

Location-specific optimization

The following section discusses the question of whether and how much location-specific optimization is required to make the most out of both configurations of perovskite/CIGS tandem solar modules. Beginning with the reference $CH_3NH_3PbI_3$ absorber material, **Figure 5.12** quantifies (a) the energy yield and (b) the

power losses associated to reflection, parasitic absorption and current matching for (1) the 4T configuration, (2) the 2T configuration with the same perovskite thickness (d = 320 nm) as the 4T device and (3) a 2T configuration with a location-specific optimized layer thickness. From the annual EY in the scenario *Phoenix Real Spectra*, it is directly evident that the 2T configuration (2) yields ~15 % less energy than the 4T configuration (1) and is in urgent need of an optimization of the device architecture. Once the perovskite absorber thickness is optimized (d = 155 nm), this relative difference reduces to ~3 %. In **Figure 5.12b**, the cause for this drastic improvement is directly identifiable. While the power losses associated to reflection and parasitic absorption approximately remain at the same level, current matching losses are reduced by ~81 %. The massive decrease in power losses originating from imperfect current matching transform this loss mechanism from the formerly dominant mechanism into the least important one. How strong current matching losses are correlated to the variations in the APE is demonstrated by the scenario disregarding spectral variations of *Phoenix Invariant Spectra*. In this scenario, device (2) displays ~34 % lower current matching losses and, contrary to the scenario *Phoenix Real Spectra* with temporal changes in APE, current matching losses can be eliminated by an optimization of the layer thickness.

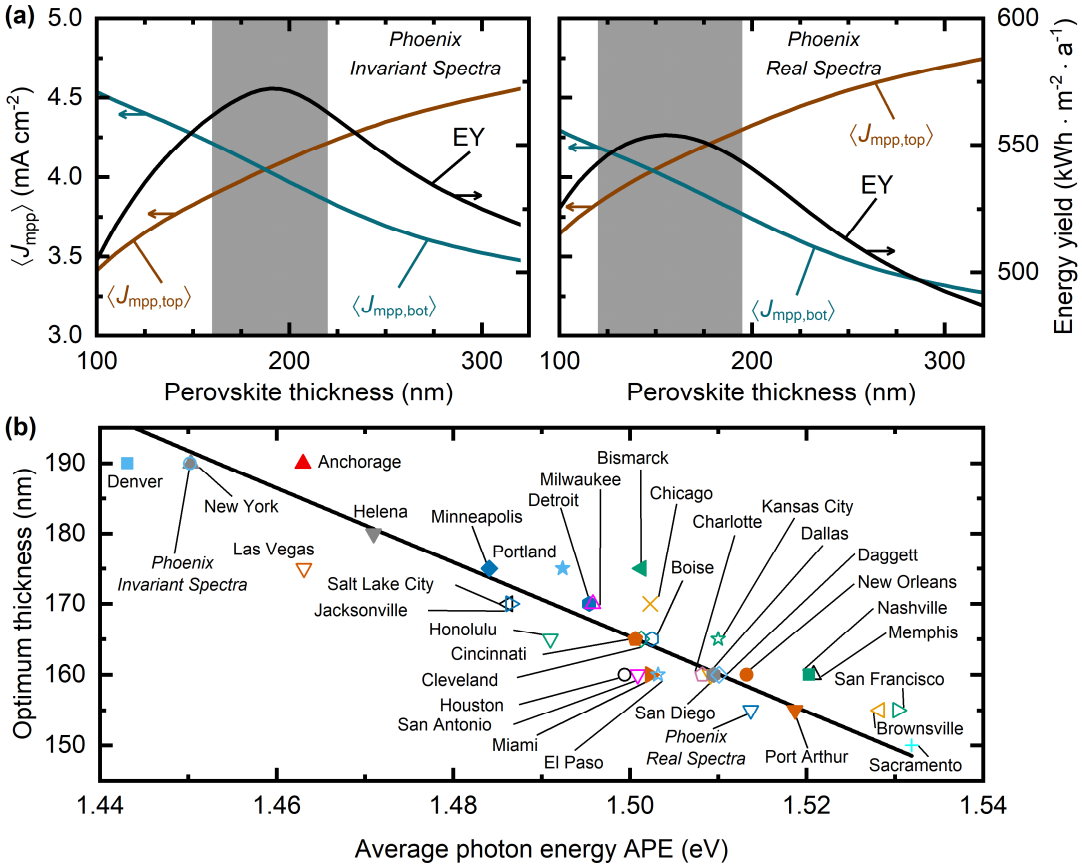

Figure 5.13: (a) The annual EY of latitude-tilted 2T perovskite/CIGS tandem solar modules and the corresponding average current densities at maximum power point $\langle J_{\mathrm{mpp}} \rangle$ in dependence of the perovskite absorber thickness for the irradiation scenarios *Phoenix Real Spectra* and *Phoenix Invariant Spectra*. (b) Overview of the optimum perovskite thickness identified for each of investigated locations as a function of the location's APE. Adapted with permission from [9]. © John Wiley & Sons, Ltd.

The identification of the tolerance of such an optimization in terms of layer thickness is resolved by investigating the current densities of both sub-cells at MPP $\langle J_{\mathrm{mpp}} \rangle$ averaged over the time span of an entire year. Naturally, the maximum EY in *Phoenix Real Spectra* and *Phoenix Invariant Spectra*, in **Figure 5.13a**, is located close to the layer thickness with matching $\langle J_{\mathrm{mpp}} \rangle$ of top- and bottom-cell since current matching

losses are minimal at this point. Nonetheless, it appears that the tolerance interval with at least 98 % of the maximum achievable EY covers a relatively broad range in perovskite thicknesses (*Phoenix Real Spectra*: ∼60 nm; *Phoenix Invariant Spectra*: ∼75 nm). Due to the higher APE in *Phoenix Real Spectra* (APE = 1.51 eV) than in *Phoenix Invariant Spectra* (APE = 1.45 eV), the former scenario requires a lower optimum perovskite thickness (d = 155 nm) to support minimum current matching losses than the latter (d = 190 nm). In general, this correlation of APE and optimum layer thickness is consistent in all investigated locations as highlighted by **Figure 5.13b**. Nonetheless, the range of the variations in between 150 nm and 190 nm in this study appears to be rather small. The small range suggests that an optimization of the perovskite thickness with regard to realistic irradiation conditions in general is already sufficient since a further location-specific optimization does not promise a significant gain. Considering the lower bandgap of Si (1.1 eV) compared to the investigated CIGS absorber (1.2 eV), the optimum perovskite thickness of perovskite/c-Si tandem solar modules naturally will be higher since the perovskite absorber needs to absorb more photons to sustain current matching. However, the correlation of optimum perovskite thickness and APE at a fixed perovskite bandgap is valid in the same way as for perovskite/CIGS tandem PV.

So far, the tuneability of the perovskite bandgap has been disregarded throughout the preceding discussion on perovskite/CIGS tandem PV. However, employing a bandgap closer to the theoretical optimum instead of the reference material $CH_3NH_3PbI_3$ (E_G = 1.55 eV) affects the mechanism of current matching drastically. Consequently, the analysis is expanded to the mixed halide wide bandgap perovskite absorbers $CH_3NH_3Pb[I_{1-x}Br_x]_3$, whose bandgap can be tuned in the range of 1.55 eV to 2.3 eV. For this study, a dataset of the refractive indices of $CH_3NH_3Pb[I_{1-x}Br_x]_3$ with integer stoichiometric compositions of bromide and iodide is interpolated to achieve a bandgap resolution of 0.05 eV [162]. To ensure comparability from an exclusive optical perspective, the electrical properties, such as the FF (∼80 %) and the V_{OC}/E_G (∼0.8) under STC remain constant throughout all bandgaps.

The results of the bandgap optimization of both the 2T and the 4T configuration installed in Phoenix (Arizona) in **Figure 5.14a** highlight the strong dependence of the annual EY on the top-cell's bandgap, in particular for the 2T configuration. The 4T device appears to be rather insensitive towards a change in the bandgap and benefits only by a boost of ∼6 % in EY by employing a 1.8 eV absorber instead of $CH_3NH_3PbI_3$ (1.55 eV). In contrast, the heavy impact of the top-cell's bandgap on current matching invokes a strong sensitivity of the 2T device to this optimization. Moreover, the EY of 2T device increases by ∼13 % by chosing the optimum top-cell bandgap. When comparing the bandgap optimization of the perovskite absorber in Phoenix to the other representative location, Portland (Oregon), which exhibits a lower APE, the importance of the average spectral irradiation becomes apparent (see **Figure 5.14b**). The optimal perovskite bandgap of 1.8 eV of the 4T device is unchanged, whereas for the 2T device a slightly lower bandgap of 1.8 eV in Portland instead of 1.85 eV in Phoenix is favored. In the optimum case, a remarkable increase of ∼52% in EY of both tandem configurations is identified compared to the base CIGS PV technology. The EY of both configurations levels out in a bandgap range of 1.8–1.85 eV. Naturally, the optimal perovskite bandgap depends on the bandgap of the bottom-cell's absorber (CIGS: E_G = 1.2 eV, Si: E_G = 1.1 eV) and is slightly higher for the investigated perovskite/CIGS tandem devices than the optimal perovskite bandgap of 1.7–1.75 eV identified for perovskite/c-Si tandem PV shown above in **Figure 5.7**.

While the first two sub-figures only provide a hint at the relative performance of the two configurations, **Figure 5.14c** provides an overview over various locations covering the most relevant climatic zones. In average, fully optimized 2T and 4T perovskite/CIGS tandem solar modules generate a comparable annual EY under realistic irradiation conditions. Some places favor the monolithic architecture and some the mechanically-stacked, without a clear trend towards one or the other. Therefore, no final conclusion can be drawn to which of the two configurations is superior from the perspective of this study.

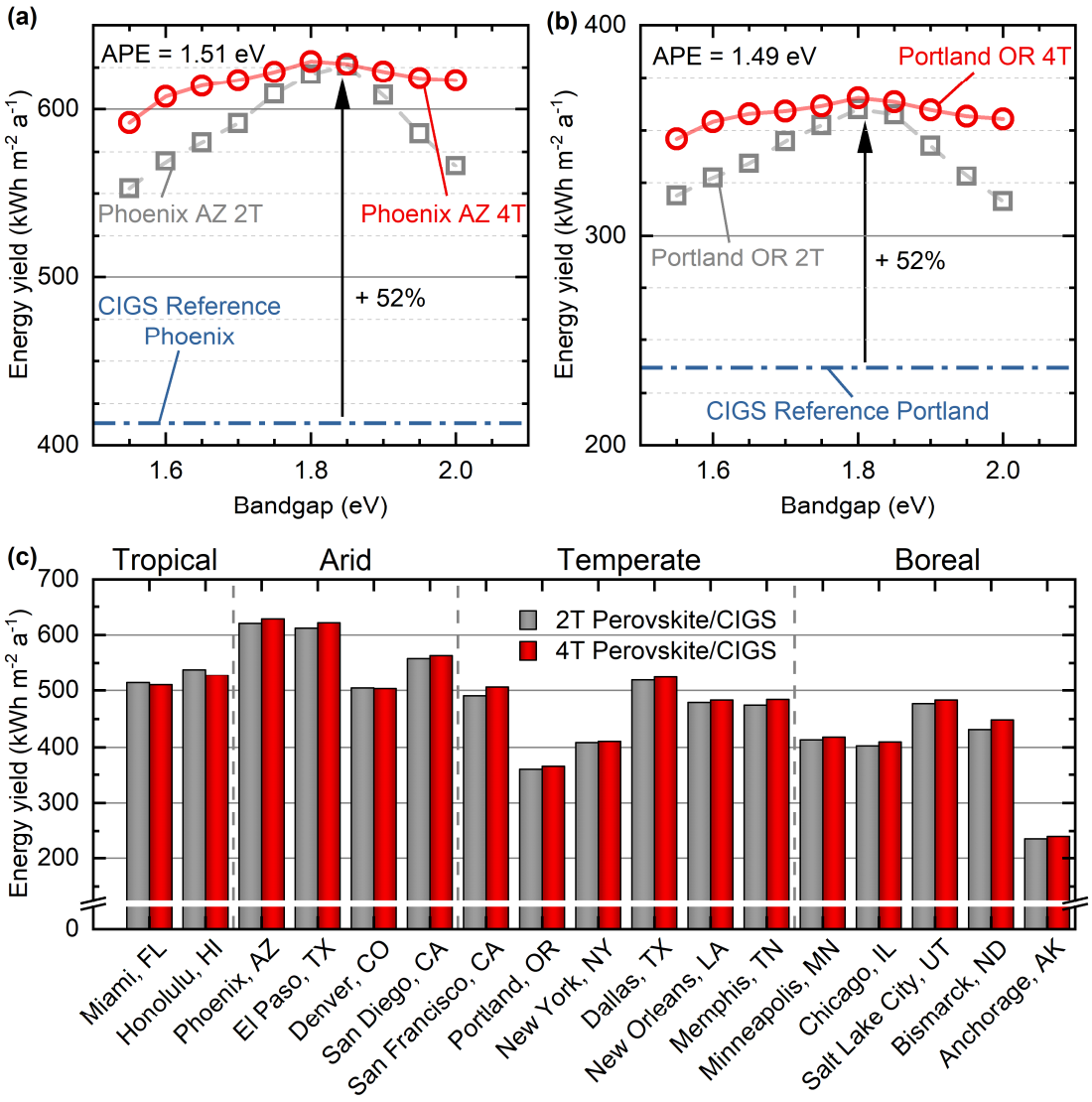

Figure 5.14: Annual EY of latitude-tilted perovskite/CIGS tandem solar modules in the 2T (dashed lines) and 4T configuration (solid lines) with a variety of $CH_3NH_3Pb[I_{1-x}Br_x]_3$ absorbers in two different climate zones: (a) arid Phoenix, Arizona and (b) humid Portland, Oregon. The tandem solar modules are optimized for each location individually with a maximum perovskite thickness of 1000 nm. (c) Overview of the maximum EY of wide bandgap (1.8 eV) perovskite/CIGS tandem solar modules in both the 2T and 4T configuration in various locations in the United States of America. The locations are sorted by the first order of their Köppen climate classification [161]. Adapted with permission from [9]. © John Wiley & Sons, Ltd.

In the preceding discussion of **Figure 5.13**, the optimization of the key parameter of the $CH_3NH_3PbI_3$ absorber's layer thickness in perovskite/CIGS tandem solar modules towards realistic irradiation conditions has been raised. The use of wide bandgap perovskite materials changes the picture significantly. The left side of **Figure 5.15** displays the energy losses of the three major loss mechanisms for perovskite/CIGS tandem solar modules in the 4T configuration, as well as in the 2T configuration, before and after the optimization for a perovskite bandgap of 1.55 eV. In contrast to the stark reduction of current matching losses for this bandgap, a perovskite bandgap of 1.8 eV, which is around the optimum, heavily facilitates current matching. Thus, the relevance of an optimization of the perovskite decreases drastically. In general, a perovskite bandgap close to the optimal bandgap for the respective tandem technology – whether it be perovskite/CIGS or perovskite/c-Si – supports current matching and diminishes the importance of optimizing the layer thickness of the perovskite absorber.

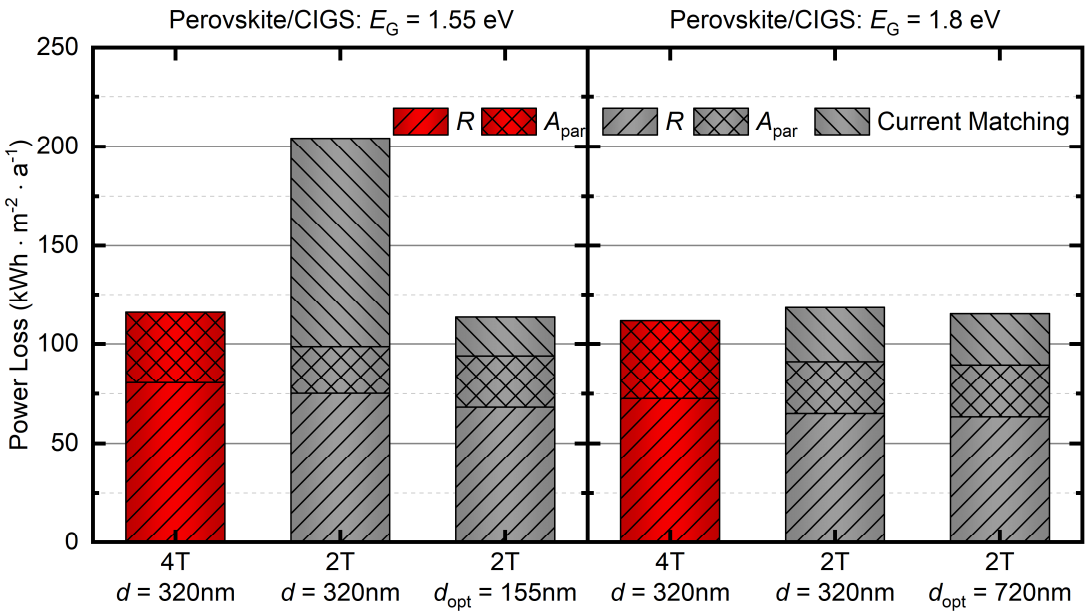

Figure 5.15: Annual power losses originating from reflection, parasitic absorption and current matching of perovskite/CIGS tandem solar modules in the 4T (red) and the 2T (gray) configuration with two different perovskite bandgaps: 1.55 eV (left) and 1.8 eV (right). The 2T configuration is once shown with the same perovskite thickness as the 4T configuration and once with an optimized perovskite thickness.

Keeping the goal of maximizing the power output of the tandem technology in mind, these results highlight the need for well-performing wide bandgap perovskite absorbers. It should be underlined again that yet such materials are not within the bounds of possibility, and that this study employs artificially designed materials.

5.5 Inactive areas

An aspect specific to tandem devices but a matter of solar modules in general is the issue of inactive areas. These losses are illustrated in **Figure 5.16** and include the module border area, spacing in between the wafers, metallic fingers and bus bars, as well as interconnection lines of thin-film PV technologies. This list already indicates that in the discussion of inactive areas it is necessary to distinguish between conventional c-Si solar modules, which consist of several densely packed solar cells, on the one hand and thin/film solar modules, which are monolithically integrated. All considerations for c-Si single-junction solar modules directly apply to 2T tandem solar modules and the bottom-cell of 4T tandem devices since these are likely to be contacted in the very same manner. Analogously, inactive areas of the top solar module of 4T tandem devices underlie the same constraints as those of thin-film single-junction solar modules.

The metallic frame at the module borders of commercial c-Si solar modules typically shades around 7 % of the total area and provides robustness and easy mounting possibilities to the solar module [163,164]. The reduction of module border areas is, therefore, primarily an issue of employing a lower amount of lightweight and robust materials, typically aluminum alloys, rather than an issue that could be tackled with optical concepts.

The second type of inactive area, which is exclusive for silicon PV and does not occur in thin-film PV, originates from the module's geometry, in particular from wafer spacing. Spacing area defines the spacing in between the single wafers and in between the wafers. These areas sum up to around 4 % [165] and depend crucially on the packing density of the silicon wafers. Raw silicon wafers are fabricated from cylindrical ingots and cut into semi-square cells to increase the packing density in a solar module. In commercially available

high-efficiency solar modules the packing density reaches as high as 96 % [163]. Since perfect packing with semi-square cells is not feasible, scattering backsheets are employed that trap some of the light inside the solar module by exploiting reflection at the glass/air interface. These backsheets reduce the effective area share of spacing areas by ~1 % absolute [166].

The third kind of inactive area is represented by tabbing and bus bars that transport the generated current in the individual solar cells along the large dimensions of a solar module. Due to the large amount of current, bus bars typically exhibit a width of around 1 mm. The most intuitive approach from a technological point of view is the development of advanced contacting technologies that display a smaller area share than standard bus bar designs or feature a lower optical footprint. In fact, the company Meyer-Burger commercialized the new SmartWire contacting technology (SWCT) in recent years that replaces effectively planar bus bars by a large number of continuous fine finger lines made of coated copper wires integrated into a foil. The circular geometry of the wires leads to a significantly larger cross-section and thus lower electrical losses. In addition, the optical footprint decreases effectively by 25 % [44]. In theory the effective shading can be as low as 30 % of the actual area in a module environment [167,168].

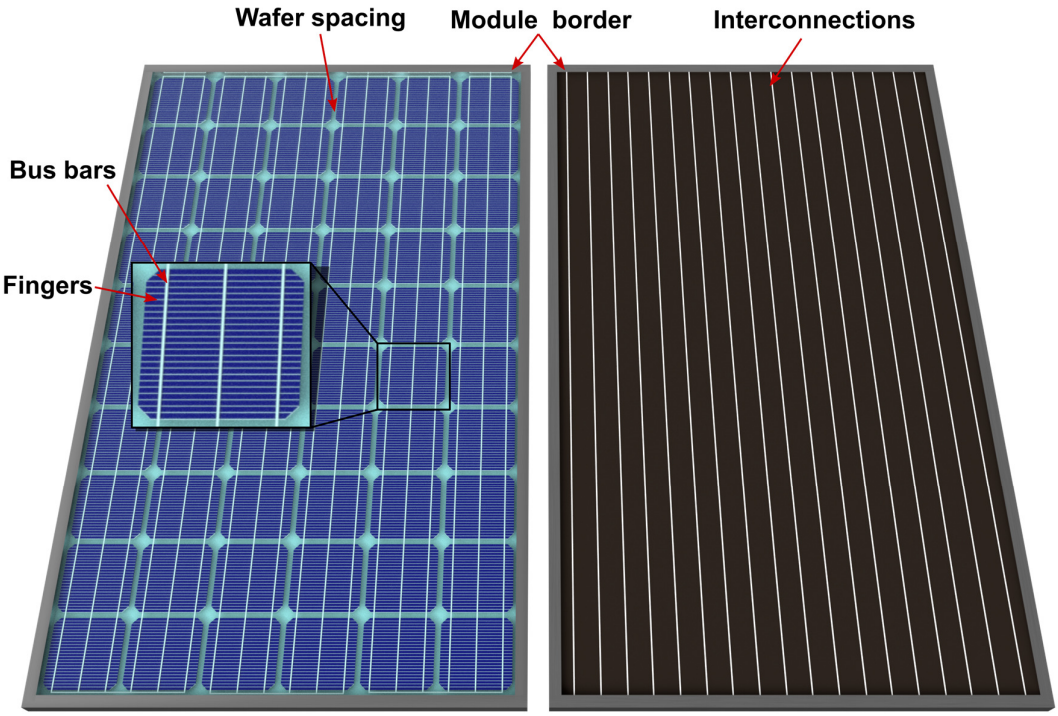

Figure 5.16: Illustrations of (left) a c-Si solar module and (right) any thin-film solar module. Labels indicate the specific inactive area losses.

Complementary to bus bars, metallic fingers of the individual c-Si solar cells collect the generated current and transport them to the closest bus bar or closest intersection to the next copper wire in the SWCT. The distance in between fingers and their individual dimensions are a compromise between low shading and low resistive loss [169]. In combination with bus bars, fingers shade around 5–10 % of the total module area, but steadily close in on the lower end of this range. A decrease of inactive area originating from contact fingers will mainly be a result of two ongoing developments: (1) a reduction of finger width deposited by screen printing, which is currently around 40 µm [170] and 20 µm on the roadmap [5], and (2) a reduced effective optical shading by semi-circular or circular cross-sections, as demonstrated by Meyer-Burger's SWCT. Circular cross-sections can be achieved via advanced deposition techniques, such as advanced screen

printing [43] or electroplating [46]. Triangular cross-sections are another intriguing alternative from an optical point of view, since they almost eliminate optical shading losses [40,41,61,62], but they may only pose a solution to inactive areas of silicon PV and not to inactive areas of thin-film solar modules. As outlined in Section 5.3, this compromise is closely connected to the choice of TCO material and thickness. An optimization of finger spacing and TCO thickness demonstrates that AM1.5G-averaged optical losses of down to 2 % are within reach [124] under the assumption of 50 µm wide metallic fingers.

In contrast to wafer-based c-Si single-junction and 2T tandem solar modules, as well as for bottom-cells of 4T perovskite/c-Si devices, packing density or metallized areas do not play any role for inactive area loss in thin-film solar modules. Instead, interconnection lines are the only source of inactive areas beside the module frame. They consist of three scribing lines: P1, P2 and P3, which separate the rear contact, the absorber and the front electrode, respectively. The width of the line crucially depends on the scribing technique. While advanced laser scribing achieves line widths of 20–50 µm [171–173], mechanical scribing is limited to around 30–90 µm and suffers from chipping effects due to the brittleness of the absorber materials [51,173]. For the established CIGS thin-film technology, PV manufacturers are currently trying to replace mechanical scribing methods usually employed for the P2 and P3 scribing lines by laser scribing techniques [70]. Considering the width of each scribing line and their spacing, a total inactive area per cell stripe of up to 300 µm is not unusual, which corresponds to inactive area losses of ∼5 % [47–51]. Further optimizations of the fabrication processes for interconnection may eventually lead to outstanding geometrical fill factors (GFF) of up to 98 % [51]. Nonetheless, the limited conductivity of TCO materials hinders a complete elimination of inactive areas by interconnection lines in thin-film PV or metallic contact fingers in Si PV. Therefore, a further reduction of the effective shading is targeted via the integration of optical cloaking concepts introduced in the Chapter 1. A detailed investigation of cloaking techniques based on freeform surfaces follows in the following Chapters 6 and 7.

5.6 Summary

The preceding sections of this chapter provide a discussion of optical loss mechanisms occurring in perovskite-based tandem solar modules. Here, the considerations are gathered and compared to each other to highlight the potential gain by eliminating each loss mechanism. **Table 5.1** displays a comparison of the contributions of all loss mechanisms of perovskite/c-Si tandem solar modules discussed earlier.

Table 5.1: Summary of the contribution of each loss mechanism to the overall optical losses of 2T and 4T perovskite/c-Si tandem solar modules based on the representative state-of-the-art tandem devices of refs. [26,27].

Configuration	Reflection	Parasitic absorption	Current matching	Inactive area
2T	2 %	11 %	4 %	16 %
4T	3 %	12 %	–	Top: 12 % Bottom: 16 %

Front-side texturing of the c-Si bottom-cell promises minimal reflection losses for both the 2T and 4T configuration. For the former, however, a front-side texture entails the technological challenge of fabricating a conformal perovskite top-cell. This challenge necessitates either evaporation deposition techniques or the employment of light-trapping textures at other interfaces of the architecture, such as the first air/glass interface. In terms of annual EY loss of perovskite/c-Si tandem solar modules based on the representative tandem devices of refs. [26,27], reflection losses (without escape reflection due to incomplete light trapping

in the Si absorber) sum up to only around 2 % and 3 % of the maximum achievable EY for the 2T and 4T architecture, respectively. This values are only achieved, once the front interface of the c-Si absorber exhibits a texture.

In contrast, parasitic absorption losses are a significantly larger source for optical losses. In particular, the front CTL and TCO of the 2T configuration and the additionally required electrode of the 4T configuration are among the biggest offenders in this regard as shown in **Figure 5.5**. A further reduction of this loss mechanism is expected to stem from reduced layer thicknesses of CTLs and the integration of optically superior TCO materials.

Moreover, current matching plays an important role for the 2T configuration under the constantly changing realistic irradiation conditions. Due to its series connection, the lower generated current out of both sub-cells limits the maximum power output. However, if properly optimized, the share of current matching losses can be as low as ∼4 %. Especially wide bandgap perovskite absorbers ($E_G \approx$ 1.7–1.8 eV) facilitate current matching significantly. If stable perovskite absorbers of this bandgap range will not be available, special attention needs to be paid to an optimization of the layer thickness of the top perovskite absorber to minimize current matching losses.

The fourth source for optical losses in perovskite-based tandem solar modules originate from many kinds of inactive areas. In total, inactive areas sum up to around 16 %. Here, border area in the form of a robust frame cover around 7 % of the total area. Spacing in between individual wafers contributes another ∼4 % for 2T tandem devices and for the bottom-cell of 4T tandems. On the cell level, metal contact grids for c-Si sub-cells and interconnection lines for thin-film solar modules cover around 5 % of the total area. Even when neglecting the share of inactive areas due to the wafer spacing and the framing required for robustness, a substantial area of ∼5 % of the perovskite/c-Si tandem solar modules is shaded by metallic contact grids and interconnection lines. These areas required for minimal electrical losses can be optimized in terms of both area coverage and their effective optical shading. Considering the total installed PV capacity of 45 GW at the end of 2018 [3] and assuming an average module efficiency of 15 % results in a total module area of approximately 300 km². The share of this area of 5 % covered by metallic contact grids and interconnection lines then sum up to ∼15 km² or 2100 football fields. In terms of PV capacity, this corresponds to ∼340 MW, a tenth of the newly installed PV in Germany in 2018 [3]. Even though these numbers highlight the huge potential for the optimization of metallic contact grids and interconnection lines, a complete elimination of these is not feasible due to the limited conductivity of available TCO materials. However, optical cloaking concepts provide a possibility to reduce the effective optical shading to nearly zero. The following Chapter 696 discusses an optical cloaking concept based on freeform surfaces that promises to reduce the optical losses due to shading by metal fingers and interconnection lines.

6 Optical simulations and energy yield modelling of freeform surface cloaks

This chapter provides a detailed investigation of the working principle of FFS cloaks. The origin of the design of the FFS cloaks studied in this thesis is provided in Section 2.3. This investigation encompasses two different implementation approaches of the FFS cloaks in solar modules. On the one hand, bare FFS cloaks, as designed by M. Schumann [60], are investigated. This approach promises the best optical performance but is not compatible with the conventional architecture of solar modules, which commonly display a planar front surface. On the other hand, this chapter considers embedded FFS cloaks. The latter are compatible with the conventional architecture of solar modules since they are integrated as cavities in the front cover glass of the solar module. The increased compatibility comes at the cost of a compromised optical performance. Furthermore, this chapter studies the impact of embedded FFS cloaks on the energy yield of a representative 4T perovskite/c-Si tandem solar module of Ref. [26] and discusses how embedded FFS cloaks may affect the optimum spacing in between inactive areas.

Acknowledgements and contributions

The majority of the results in the following chapter on freeform surface (FFS) cloaks was already published in a study on CIGS thin-film solar modules in Ref. [174]. *In light of the application of the liquid glass technique for the fabrication of embedded FFS cloaks, the simulations in Ref.* [174] *have been reproduced with fused silica glass instead of the polymer material. The ray-tracing simulations used in this chapter was developed by M. Schumann and extended by the author to consider absorption and dispersion. The applied EY modelling framework was developed in collaboration with Raphael Schmager, Ulrich W. Paetzold and Jonathan Lehr. Details about this framework are provided in Chapter 4. All simulations of this chapter were performed by the author.*

6.1 Working principle of bare freeform surface cloaks

In view of the subsequent analysis of designs of FFS cloaks that are compatible with the architecture of conventional solar modules, the working principle of a bare FFS cloak (without a front cover glass) is investigated. The geometry of the FFS cloak is defined by three design parameters: (1) the lateral extent of the cloaked area R_1, (2) the lateral extent of the cloak R_2 and (3) the distance between the inactive area and the center of the FFS cloak y_0 (see Section 2.3). The investigated bare FFS cloak is based on the optimum design parameters as suggested by M. Schumann *et al.* [60]. Therefore, it is referred to as the *bare original FFS cloak* here. The optimum parameters for a 200 µm-wide inactive area are R_1 = 100 µm, R_2 = 1000 µm and y_0 = 100 µm. With regard to the total width of a unit cell of 5000 µm in this study, the inactive area correlates to a GFF = 4 %. A planar layer of the same refractive index as that of the cloak n_{cloak} serves as a reference. It is called the *planar reference* in the following.

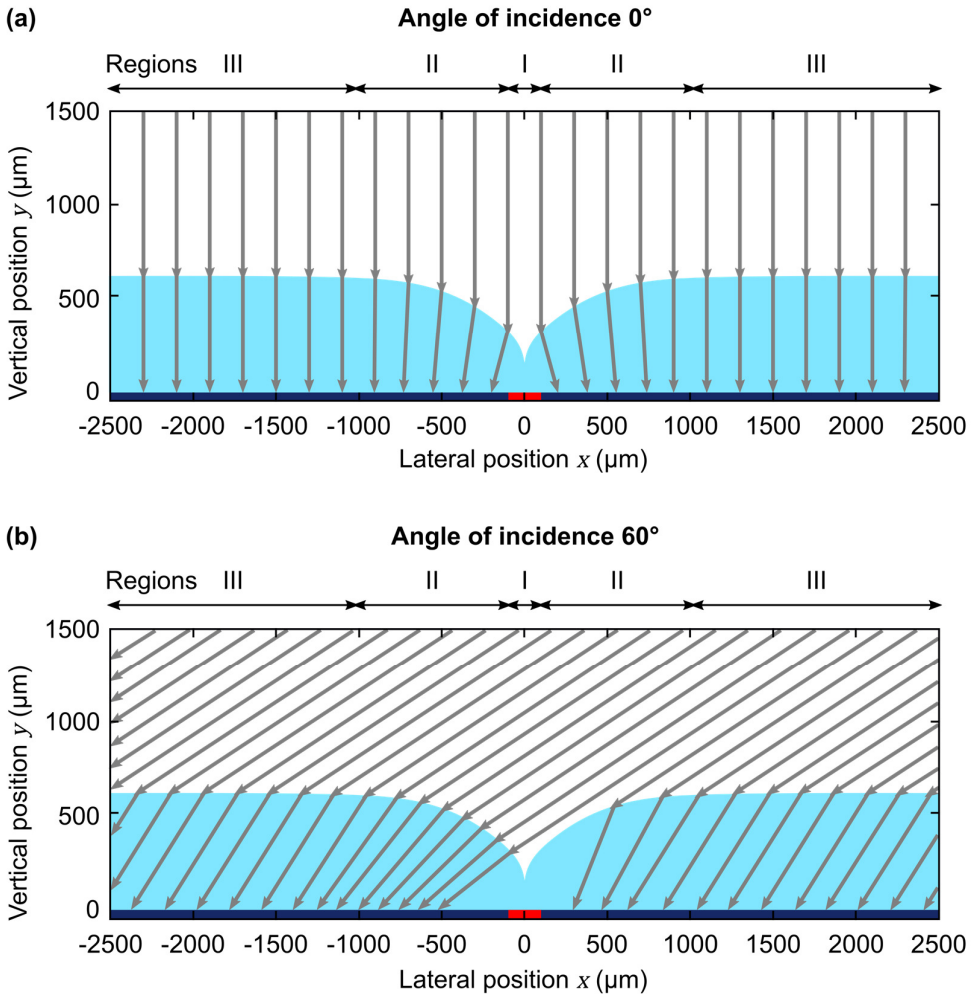

Figure 6.1: Illustration of the refraction of incident light by the *bare original FFS cloak* at (a) normal incidence and at (b) an angle of incidence of 60°. The active area of the solar module is indicated in dark blue and the inactive area in red. Paths of reflected rays are omitted for clarity.

The working principle of the *bare original FFS cloak* under illumination at normal incidence is illustrated in **Figure 6.1a**. Incident light is refracted and guided away from the inactive area (red) by the *bare original FFS cloak* into the active area of the solar module (blue). Under normal incidence, the light rays starting in region I ($|x| \in [0, 1000]$) are homogeneously redistributed into region II ($|x| \in [100, 1000]$). Region III is

the planar area in between two adjacent FFS cloaks. The dimension of this region depends on the distance between two inactive areas and the lateral extent of the FFS cloak. Practically, this region could be eliminated by reducing the distance between adjacent inactive areas until the FFS cloaks start to overlap. A reduction of the distance between two inactive areas has the additional benefit that a thinner TCO is required for the lateral transport of charge carriers towards the inactive areas, which represent the metallic contacts or interconnection lines [155]. A more detailed discussion on this topic follows in Section 6.3.

The ability of the FFS cloak to guide light into the active area is not only limited to normal incidence but also sustains at oblique angles of incidence. **Figure 6.1b** illustrates the outstanding cloaking performance of the *bare original FFS cloak* at large angles of incidence such as the depicted case of 60°. The outer flanks of the FFS cloak ensure that incident light is still refracted into the active area. It should be noted that a considerable portion of light hits the *bare original FFS cloak* under near-to-normal incidence in regions I and II ($x \in [-1000, 0]$), which reduces reflection losses and in turn increases light incoupling compared to the *planar reference*.

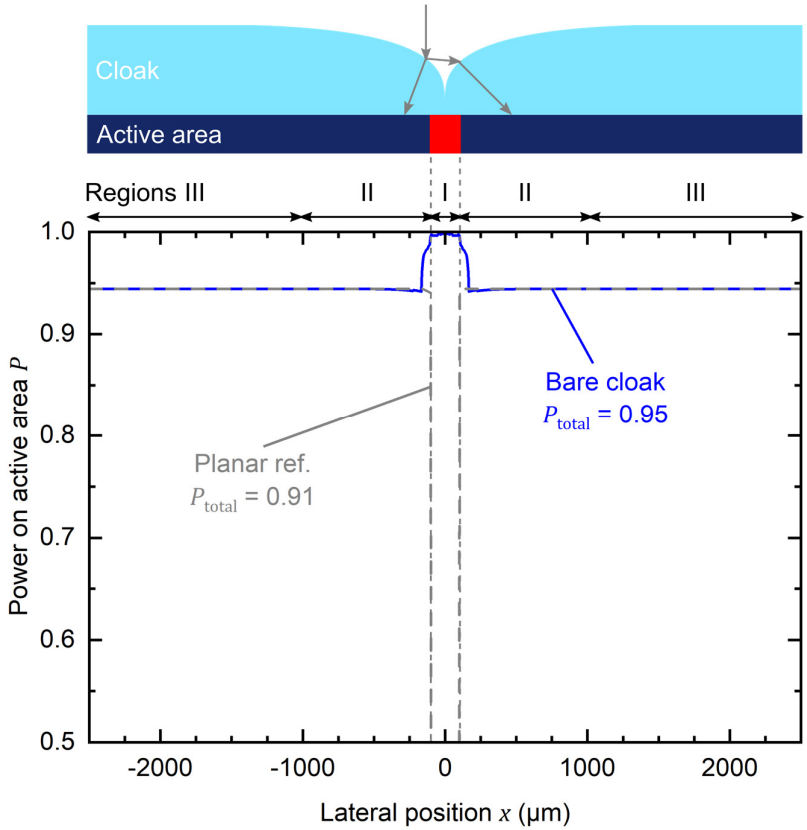

Figure 6.2: Power on the active area $P(x)$ of the solar module of rays starting at lateral position x for the *planar reference* cover and the *bare original FFS cloak*. The active area of the solar module is indicated in dark blue and the inactive area in red. Adapted with permission from [174]. © Elsevier 2018.

The *bare original FFS cloak* increases the power incident on the active area $P(x)$ of rays starting above the inactive area of the solar module to close to unity (region I in **Figure 6.2**). In regions II and III, the FFS cloak is close to planar and consequently displays a very similar $P(x)$ as the *planar reference*. One interesting observation is that the *bare original FFS cloak* boosts $P(x)$ in the part of region II beyond that of the *planar reference* even though there is no inactive area located in region II. The observable increase in $P(x)$ extents by ~70 µm into region II. This observation is a consequence of the fact that incident light in this part of region II is reflected towards the opposing flank of the *bare original FFS cloak* and has a second change to enter the

FFS cloak. This effect is commonly referred to as improved light incoupling. It is illustrated by representative ray paths in **Figure 6.2**.

A differentiation and quantification of the two underlying optical effects – cloaking and light incoupling – proves to be challenging. An investigation of architectures that incrementally transition from the architecture of the *planar reference* to that of the *bare original FFS cloak* provides a possible approach to meet this challenge. This transition is outlined schematically on the right hand side of **Figure 6.3**. Associated to each incremental transition are the following optical effects:

1) **Index matching:** Introducing a layer at the interface between the ambient air and the pristine solar module changes the reflectance and $P(x)$ of the new architecture II compared to architecture I. If the refractive index (n_{cloak} = 1.46) of the new layer is in between the refractive indices of the TCO top layer of the solar module ($n_{\mathrm{TCO}} \approx 1.95$ at λ = 550 µm) and the ambient air (n = 1), the effective matching of the refractive indices increases the overall power incident on the active area.
2) **Cloaking:** Assuming a transparent interconnection (architecture 3) depicts the case of ideal *cloaking* or in other words an invisible inactive area. This cloaking effect directly correlates to the GFF and, thus, leads to a maximum expected gain by $\zeta_{\mathrm{max}} = \mathrm{GFF}/(1-\mathrm{GFF}) = 4.2$ % when disregarding any additional optical effects. This transparent interconnection is only a virtual representation of the cloaking effect, since invisibility cloaking is not feasible via a planar surface of a homogeneous material.
3) **Light incoupling:** The third optical effect is improved light incoupling by the reduction of reflection via the curvature of the FFS. In a part of region II (see **Figure 6.2**), reflected light is directed towards the opposing flank of the FFS in architecture 4, providing an increased probability to be coupled into the cloak layer. In combination, cloaking and light incoupling sum up to a relative increase in P of ζ = 4.5 % at normal incidence, which translates directly to an increase in J_{SC}.

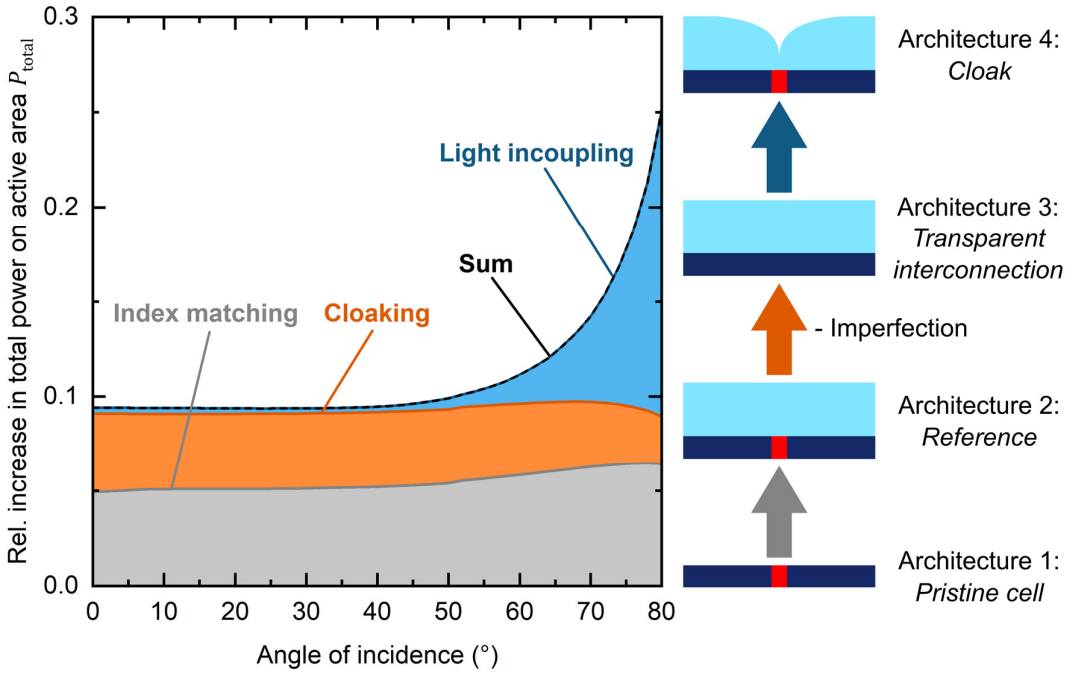

Figure 6.3: Cumulative illustration of the three underlying optical effects of the bare original FFS cloak, which contribute to the angular-resolved relative increase in power on the active area of the solar module at a wavelength of 550 nm. Adapted with permission from [174]. © Elsevier 2018.

It should be pointed out that this quantification is only valid for FFS cloaks that provide perfect cloaking of the inactive area. Once the inactive area is not perfectly cloaked, imperfect cloaking needs to be considered. This level of imperfection is defined as the difference between P_{total} of a cloak (architecture 4) with and without an inactive area below. For imperfect cloaking of inactive areas, this level is subtracted from the value of cloaking obtained from mere geometrical considerations and leads to lower values once the imperfection is non-zero. This approach enables a mathematical distinction of cloaking and light incoupling.

The results show that the relative increase in P_{total} by the *bare original FFS cloak* remains constant across the entire angular range, which is equivalent to omnidirectional cloaking. In particular, the outer domains of the curvature of the FFS cloak ensure this ability as already illustrated before in **Figure 6.1b**. Another interesting finding is the strong contribution of light incoupling to the relative increase in P_{total} at large angles of incidence. This trend is a consequence of the lower Fresnel reflection of a considerable portion of light rays hitting the non-planar surface of the *bare original FFS cloak* at close-to-normal incidence (see **Figure 6.1b**). Furthermore, the relative increase in P by index matching slightly varies at oblique angles of incidence due to the different amount of Fresnel reflection of the pristine cell and the *planar reference*. From here on, cloaking and light incoupling are focused exclusively since the planar architecture is used as the reference architecture.

6.2 Working principle of embedded freeform surface cloaks

Even though the *bare original FFS cloak* provides perfect cloaking and ideal optical performance, it is not an option for the deployment on solar modules under realistic operation conditions. The deep notch of the FFS cloak naturally is prone to soiling and the accumulation of dirt. This vulnerability is one of the reasons – with the simple production method of course being the key – why planar front covers are the industrial standard for solar modules. Therefore, the compatibility of optical cloaking concepts with commercial solar modules is a key requirement for further development of these concepts. An incorporation into the conventional architecture of solar modules maintains a planar front surface and, thus, eliminates the pronounced vulnerability to soiling. Considering a conventional architecture of a polymer encapsulant and a front cover glass, an embedment of the investigated FFS cloaks into the cover glass promises the most durable approach since optical concepts introduced into the polymer encapsulant may deform under the natural thermal cycling of realistic operation conditions. However, embedding the *bare original FFS cloak* (discussed in the preceding section) severely affects its light incoupling and cloaking abilities. The resulting air void of this *embedded original FFS cloak* introduces two additional interfaces between air and the cloak material. Therefore, parasitic reflection losses diminish the gain in P by redirecting incident light into the active area.

The reduced P of the *embedded original FFS cloak* is demonstrated in **Figure 6.4a**. While the *planar reference* and the *embedded original FFS cloak* display the same behavior in region III, parasitic reflection at the air/cloak interfaces of the *embedded original FFS cloak* reduces P_{total} below that of the *planar reference* in region II. In addition, for light incident above the inactive area (region I), $P(x)$ decreases from formerly close to unity to a value $\sim$0.92, which is still a significant improvement compared to the *planar reference* with $P(x)$ of zero. Overall, the relative increase in P_{total} shrinks to $\sim$1 %. For oblique angles of incidence, the negative impact of poor light incoupling intensifies and even overcomes the omnidirectional cloaking that the *embedded original FFS cloak* still provides (see **Figure 6.4b**). In fact, it exhibits a lower P_{total} than the *planar reference* for angles $>$55°. Consequently, embedding the original FFS cloak into the front cover glass has a vanishing impact on the amount of harvested light in the solar module. Therefore, an optimization of the design of the embedded FFS is required.

The most intuitive approach to tackle the issue of parasitic reflection is to reduce the lateral extent of the embedded FFS cloak by truncating the original design or by adjusting the cloak parameter R_2, which

represents the lateral extent. The architecture obtained by the former approach is referred to as the *embedded FFS cloak with optimized cutoff* and the latter as the *embedded FFS cloak with optimized* R_2 from here onwards. Both designs are optimized with regard to maximum annual EY in Phoenix (Arizona). The results of this optimization and further studies of the impact of embedded FFS cloaks on the annual EY of solar modules are provided in Section 6.3. For now, the two optimized designs are examined with regard to their underlying cloaking and light incoupling abilities.

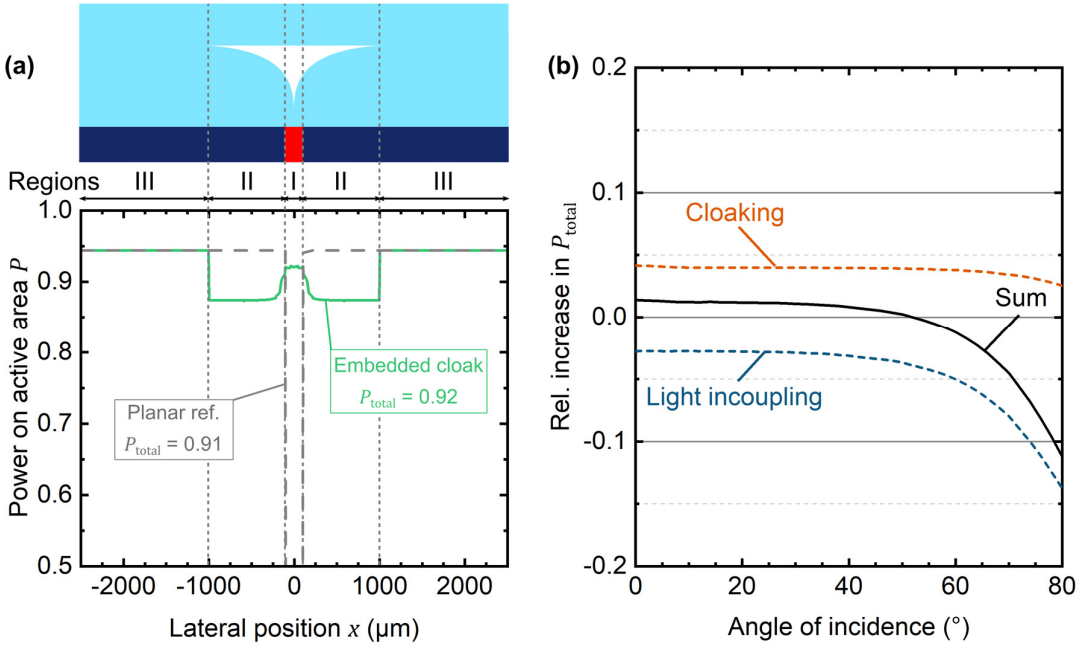

Figure 6.4: (a) Spatially resolved power on the active area $P(x)$ of a solar module for the *planar reference* and the *embedded original FFS cloak*. (b) Relative increase in total incident power P_{total} on the active area of a solar module by the *embedded original FFS cloak* compared to the *planar reference*. Both results are displayed for a wavelength of 550 nm. Adapted with permission from [174]. © Elsevier 2018.

The raytracing simulations highlight the substantial shrinkage of the region with reduced $P(x)$ (region II) for both the *embedded FFS cloak with optimized cutoff* (**Figure 6.5a**) and the *embedded FFS cloak with optimized* R_2 (**Figure 6.5b**). In both cases, parasitic reflection losses are almost entirely eliminated by the reduction of the lateral extent of the FFS. Consequently, both optimizations lead to P_{total} at normal incidence that is almost on par with the *bare original FFS cloak* of 0.94, which correlates to a relative increase by 3.5 %. Concerning oblique angles of incidence, the negative impact on light incoupling by embedding the FFS cloak is strongly hampered by the optimization as depicted in **Figure 6.5c + d**. Furthermore, the *embedded FFS cloak with optimized cutoff* maintains perfect cloaking up to an angle of around 60°. The cloaking of the *embedded FFS cloak with optimized* R_2 slightly drops in between 25° and 35° but shows better cloaking at large angles of incidence >60°. At angles of incidence above 60°, the first light rays start to hit the inactive area since the reduced lateral extent of the FFS does not suffice to refract all incident light into the active area. In particular, the *embedded FFS cloak with optimized cutoff exhibits* a lower P_{total} than the *planar reference* for angles >60°, while the *embedded FFS cloak with optimized* R_2 maintains a comparable performance as the *planar reference* at such extreme angles.

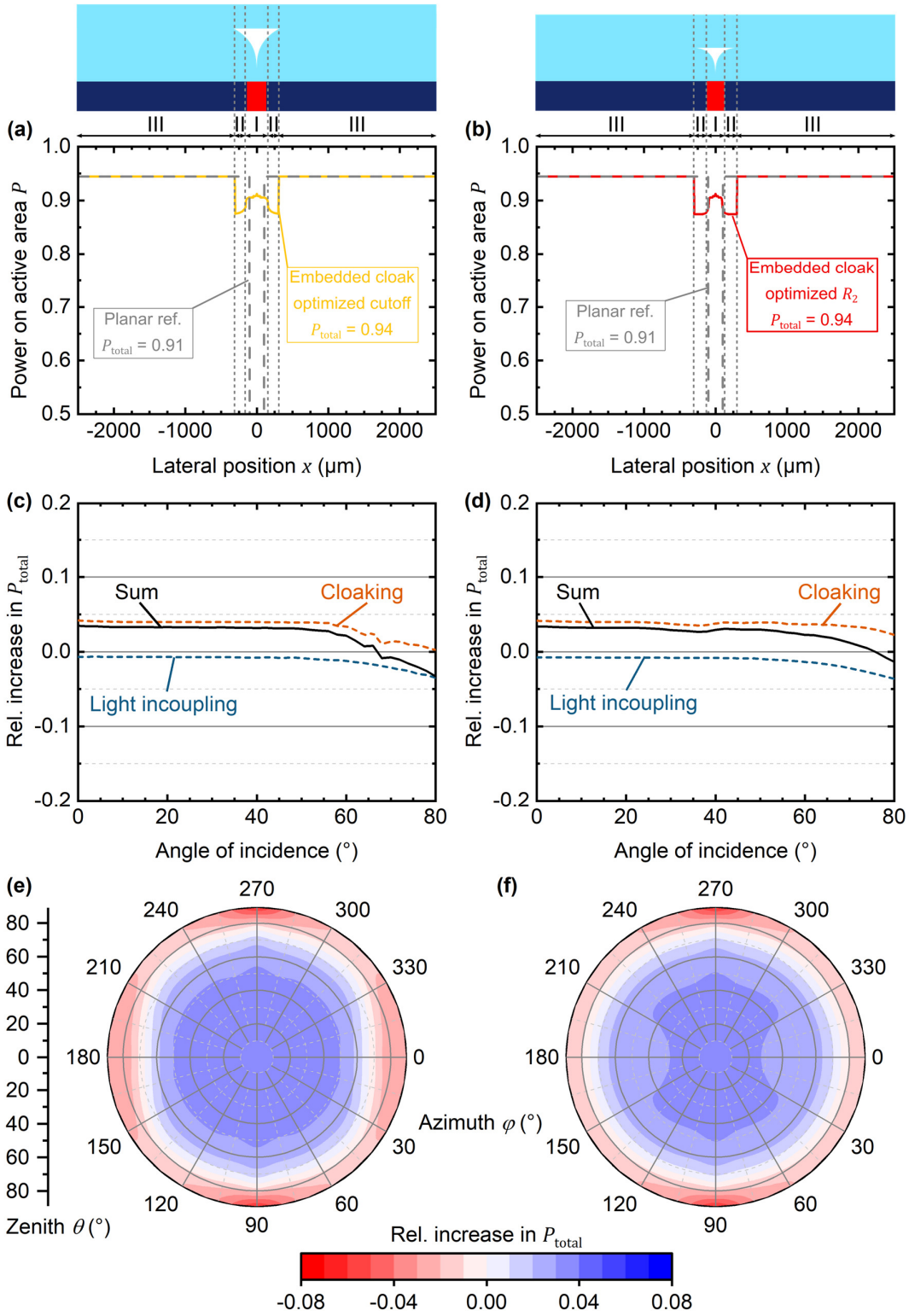

Figure 6.5: Spatially resolved power $P(x)$ incident on the active area of (a) the *embedded FFS cloak with optimized cutoff* and (b) the *embedded FFS cloak with optimized* R_2 compared to the *planar reference*. The corresponding relative increase in total incident power P_{total} of both designs in the cross-sectional plane is provided in (c) and (d) and for all azimuth angles in (e) and (f). All results are displayed for a wavelength of 550 nm. Adapted with permission from [174]. © Elsevier 2018.

The relative increase in P_{total} shown in **Figure 6.5e + f** for the *embedded FFS cloak with optimized cutoff* and the *embedded FFS cloak with optimized* R_2, respectively, demonstrates that the *embedded FFS cloak with optimized cutoff* maintains its excellent cloaking ability for all azimuth angles, but exhibits poor performance for zenith angles >60°. In particular for φ = 90° and φ = 270°, the embedment of FFS cloak with optimized cutoff reduces the incident light on the active area of the solar module by up to 8.3 % for $\theta > 60°$. In contrast, the *embedded FFS cloak with optimized* R_2 does not suffer from such a strong reduction in P_{total} for large zenith angles and performs on par with the *planar reference* for the most part of the azimuth angle range. Poor light incoupling only leads to a notable reduction of P_{total} by 5.8 % for azimuth angles orthogonal to the cross-sectional plane (φ = 90° and φ = 270°). Furthermore, it demonstrates a considerable increase in P_{total} for all zenith angle <60°. Its slight drop in relative increase in P_{total} between the zenith angles θ of 25° and 35° (see **Figure 6.5d**) vanishes for azimuth angles greater than 35°.

In general, embedding FFS cloaks into the cover glass of solar modules appears to be a viable option from an optical perspective. The drawback of parasitic reflection losses originating from the embedment of the FFS cloak is to overcome by a design optimization of the FFS cloak. For both approaches, the optimization leads to a significant increase in P_{total} that almost copes with the GFF of the inactive areas in the case of near to normal incidence. For very oblique angles of incidence >60°, the P_{total} is comparable to that of the *planar reference*, in particular for the *embedded FFS cloak with optimized* R_2. The variations in relative increase in P_{total} of both designs of embedded FFS cloaks with the azimuth angle are small and consequently negligible for investigations of the impact of embedded FFS cloaks on the annual energy yield of solar module in the following Section 6.3.

6.3 Embedded freeform surface cloaks under realistic irradiation conditions

For the application of embedded FFS cloaks in solar modules, an outstanding optical performance under realistic irradiation conditions is key. Therefore, an optimization of the design of embedded FFS cloaks must be conducted with regard to the EY. The 4T perovskite/c-Si tandem solar module, which is modelled in Chapter 5 and is based on Ref. [26], is used as the base technology for the optimization. Additionally, the same contacting scheme – 200 µm-wide inactive areas with a spacing of 5 mm – as in the two preceding Sections 6.1 and 6.2 is assumed for the perovskite top-cell. Since the bottom-cell of Ref. [26] is a back-contacted c-Si solar cell, no additional shading by the bottom-cell is considered. Consequently, the modelled 4T perovskite/c-Si tandem solar module exhibits a GFF of 4 % for both sub-cells. It should be noted that the inactive areas of a 4T perovskite/c-Si tandem solar module are typically consisting of interconnection lines. However, the following conclusions are also valid for metallic contact fingers of 2T perovskite/c-Si tandem devices, since the cloaking of inactive areas via freeform surfaces is independent of the electrical configuration of a tandem solar module. For the optimization, two representative locations are chosen: (1) Phoenix (Arizona) with a large share of specular irradiation of 70 % annually and (2) Portland (Oregon) with a large share of diffuse irradiation of 49 % annually. The comparison of two locations of fundamentally different ratios of specular versus diffuse irradiation demonstrate the sensitivity of optimum design parameters of embedded FFS cloaks with regard to the irradiation conditions. Since refraction is a broadband optical phenomenon, the impact of the APE on the performance of the FFS cloaks is negligible. Additionally, only the cross-sectional plane of the FFS cloaks (zenith angle θ = 0°) is considered to keep the computation times within reasonable limits. This assumption is justified given the minor variations in relative improvement in P_{total} with the azimuth angle shown in the preceding Section 6.2 and the fact that this plane covers the largest angles of incidence of realistic irradiation with regard to the geometry of the FFS cloak.

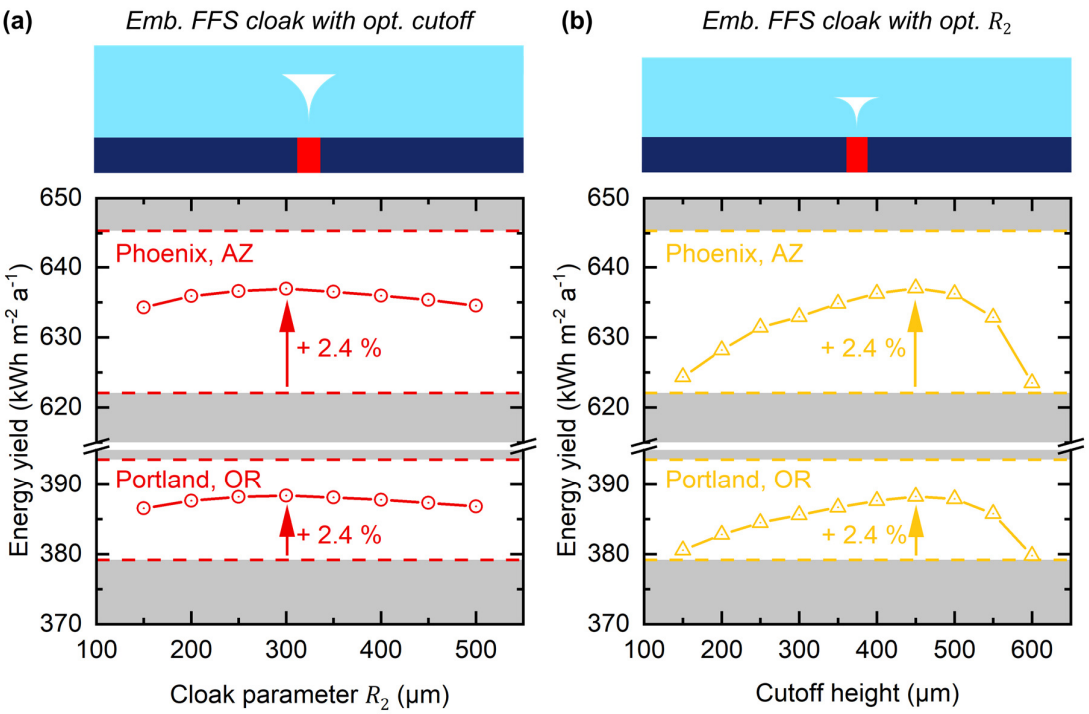

Figure 6.6: Annual energy yield of the representative 4T perovskite/c-Si solar module of Ref. [26] with FFS cloaks embedded into the cover glass in dependence on (a) the cloak parameter R_2 and (b) the cutoff height at two representative locations with an optimized tilt. Additionally, the EY of a *planar reference* with (below curves) and without (above curves) 4 % of inactive area is indicated by dashed lines for each scenario.

The results of the optimization show that the optimum parameters (R_2 = 300 µm and cutoff = 450 µm) differ significantly from the parameters of the *original bare FFS cloak*. For the *embedded FFS cloak with optimized* R_2, the cloak parameter R_2 is reduced from initially 1000 µm to 300 µm. Thus, the cloak extends only beyond the inactive area by 200 µm. In the case of the *embedded FFS cloak with optimized cutoff*, the *embedded original FFS cloak* is truncated by 25 % so that it also exceeds the inactive areas by ~200 µm. It is noteworthy that each micrometer that the FFS cloak exceeds the inactive area has a negative impact on the relative performance compared to the *planar reference* at normal incidence as explained in **Figure 6.4**. However, a larger dimension of the FFS cloak supports cloaking at more oblique angles of incidence than a smaller FFS cloak. The optimum cloak parameter R_2 and cutoff are, therefore, a compromise of highest P_{total} under all angles of incidence of realistic irradiation conditions. Moreover, the optimization has a high tolerance to the ratio of specular versus diffuse irradiation, since the optimal parameters for R_2 and the cutoff are the same under the very different irradiation conditions of the two representative locations. In addition, the optimum in EY is broadly extended depending of the cloak parameter R_2, while that of the cutoff is more pronounced, which is owed to the fact that, unlike varying the cloak parameter R_2 directly, a truncation does not reduce the FFS cloak's lateral extent linearly. Overall, both optimized designs of embedded FFS cloaks promise a 2.4 % increase in annual EY, regardless of the location under investigation. In view of the maximum potential increase of 3.7 % for a planar reference without inactive areas, this gain in EY corresponds to a cloaking efficiency under realistic irradiation conditions of 65 %.

When looking at the relative improvement of power generation by the optimally tilted 4T perovskite/c-Si tandem solar module over the course of a day, it becomes evident that embedding FFS cloaks into the cover glass is particularly beneficial around noon of a sunny day as shown for the example of June 10$^{\text{th}}$ in Phoenix (Arizona) in **Figure 6.7a**. Then, a large amount of irradiation impinges the solar module at close-to-normal incidence (see **Figure 6.7c**) and the efficient cloaking ability of the embedded FFS cloaks at these

angles results in an increase in power output by up to 2.9 %. In the early morning and late evening, both designs of the FFS cloak produce a power output comparable to that of the *planar reference*, since efficient cloaking and poor light incoupling approximately keep the balance for strongly diffuse irradiation. Nevertheless, this observation does not allow a general statement about the cloaking performance under highly diffuse irradiation conditions. For example, the embedded FFS cloaks improve the power output of the tandem solar module noticeable by up to 2.3 % around noon of a very cloudy day (see **Figure 6.7b + d**). In general, no distinct difference in terms of cloaking performance under realistic irradiation conditions of the *embedded FFS cloak with optimized* R_2 and the one *with optimized cutoff* are perceptible.

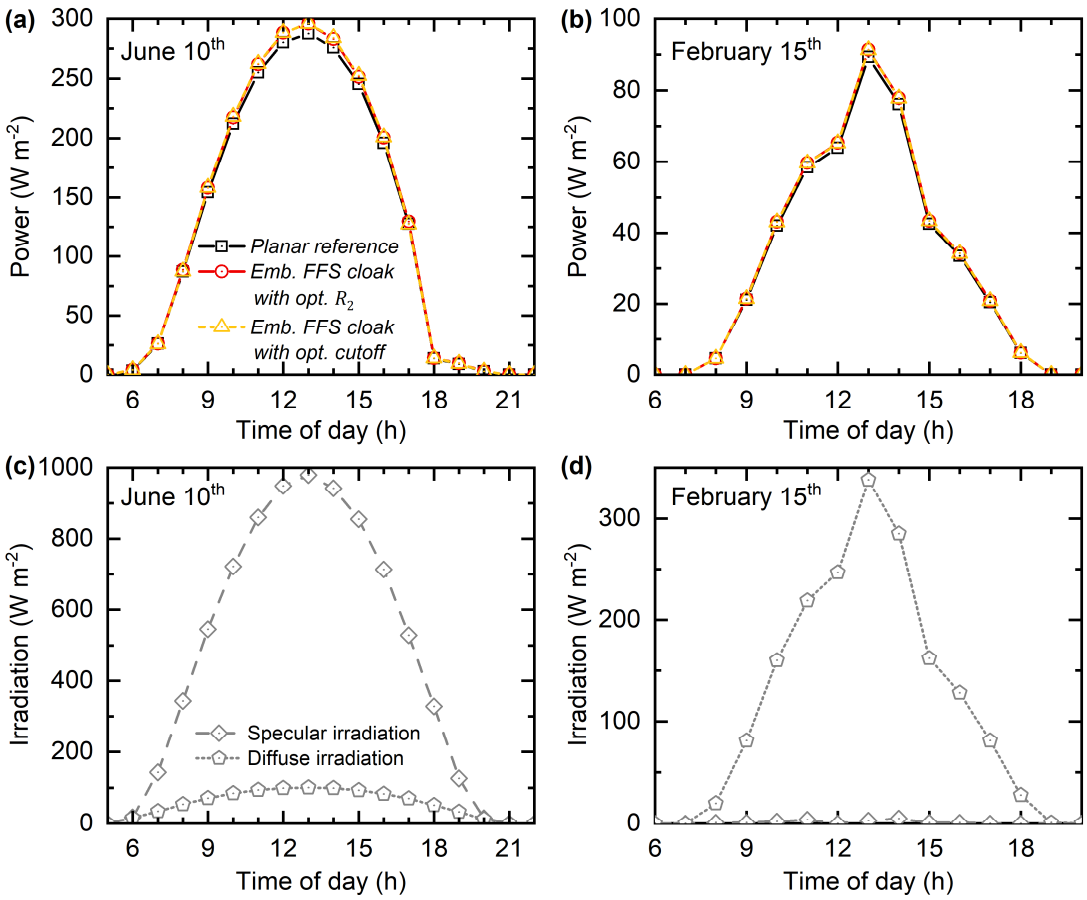

Figure 6.7: Generated power of the representative 4T perovskite/c-Si tandem solar module of Ref. [26] with FFS cloaks embedded into the cover glass in Phoenix (Arizona) over the course of (a) a representative sunny day (June 10th) and (b) a representative cloudy day (February 15th). The corresponding specular and diffuse irradiation incident on the optimally tilted tandem solar module is given in (c) and (d).

To optimize the power output of the 4T perovskite/c-Si tandem solar module further, the effective cloaking of inactive areas allows the consideration of increasing the inactive area by a larger number of metallic contact fingers or interconnection lines, while maintaining a comparable shading loss as a non-cloaked device. In general, the thickness of the front TCO required for low resistive losses and an efficient charge transport is determined by the spacing between the inactive areas [175]. The smaller the spacing, the thinner the TCO. However, the spacing of inactive areas cannot be reduced indefinitely because the GFF of inactive areas increases with a smaller spacing. Therefore, the contact scheme commonly is a compromise between low resistivity of the TCO and low shading losses by inactive areas. In view of an effectively reduced optical footprint of inactive areas with FFS cloaks, a larger number of metallic contact fingers and interconnection lines is conceivable. A new optimal spacing between the inactive areas is computed for the

representative 4T perovskite/c-Si tandem solar module under realistic irradiation conditions at a representative location (Phoenix, Arizona) via EY modelling. The thickness of the front TCO of the tandem device is reduced to the same extent as the inactive area spacing to guarantee almost constant resistance losses. The calculations span from a spacing of 5 mm and an initial TCO thickness of 200 µm to spacing of 2 mm and a corresponding TCO thickness of 80 µm.

The results in **Figure 6.8** show that the initial spacing and TCO thickness already represent the optimal contact scheme for the *planar reference*. In contrast, both designs of embedded FFS cloaks shift the optimal spacing to the same extent towards smaller values and a larger number of metallic contact fingers or interconnection lines so that the optimal spacing between the inactive areas is 2.8 mm for the cloaked 4T perovskite/c-Si tandem solar module. The lower thickness of the front TCO results in a reduced parasitic absorption of this layer. Consequently, the relative increase in annual EY grows from formerly 2.4 % to 3.1 % compared to the maximum EY of the *planar reference*.

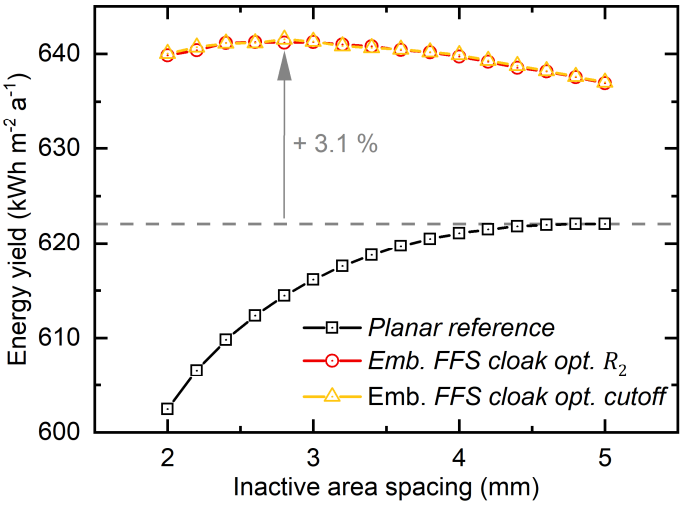

Figure 6.8: Annual EY of the representative 4T perovskite/c-Si tandem solar module in Phoenix (Arizona) at optimal tilt in dependence of the spacing between the inactive areas. As a cover glass, a *planar reference* (black) and embedded FFS cloaks with optimized R_2 (red) and cutoff (yellow) are considered. The thickness of the front TCO is reduced in same amount as the inactive area spacing to maintain the sheet resistance of the front TCO.

6.4 Summary

In this chapter, the working principle of the optical concept of FFS cloaks is discussed and two different designs compatible with the conventional architecture of solar modules are proposed. It is apparent that the *bare original FFS cloak* shows the ideal optical performance for all angles of incidence, which is due to its excellent light incoupling properties shown in **Figure 6.1** and **Figure 6.2**. However, once encapsulated, the original design of the FFS cloak requires an optimization, since the large lateral extent of the *embedded original FFS cloak* introduces a large amount of parasitic reflection. The optimization of the lateral extent of the FFS cloak via (1) a cutoff or (2) a reduction of the cloak parameter R_2 results in a comparable P_{total} to the *bare original FFS cloak* for angles of incidence of up to 50°. For larger angles of incidence, the relative increase in P_{total} compared to the *planar reference* decreases for both the *embedded FFS cloak with optimized* R_2 and the *embedded FFS cloak with optimized cutoff* and turns negative for angles above 70–75°. This trend towards a negative contribution is even more pronounced for the latter.

Furthermore, the cloaking performance under realistic irradiation conditions of the two proposed designs of embedded FFS cloaks are analyzed via EY modelling in two representative locations with fundamentally different ratios of specular to direct irradiation. For both locations – the very sunny Phoenix

(Arizona) and the cloudy Portland (Oregon) – a relative increase of 2.4 % the annual EY is identified. In view of a GFF of inactive areas of 4 %, this relative increase corresponds to a cloaking efficiency of 65 % under realistic irradiations conditions. The reduction of the shading losses of inactive areas via FFS cloaking suggests redesigning the front contact scheme of the investigated tandem solar module by simultaneously reducing the spacing between the inactive areas and the thickness of the front TCO. This way, resistive losses remain approximately constant. Consequently, the optimal spacing reduces from 5 mm of the *planar reference* to 1.8 mm and the relative increase in EY compared to the *planar reference* increases from formerly 2.4 % to 3.1 %.

With regard to upscaling, it should be noted that although the proposed designs of embedded FFS cloaks do not differ in their ability to cloak inactive areas under realistic irradiation conditions, they have significantly different volumes. In fact, the *embedded FFS cloak with optimized* R_2 exhibits a 51 % smaller cross-section than the *embedded FFS cloak with optimized cutoff*. This value is directly translatable to volume and fabrication time using DLW, which is a critical parameter to accelerate this time-consuming fabrication technique.

7 Prototypes of freeform surface cloaks in perovskite-silicon tandem solar modules

This chapter reports on prototype FFS cloaks applied to perovskite, c-Si and CIGS solar cells and modules with a particular focus on the development of fabrication techniques of FFS cloaks that are compatible with the conventional architecture of perovskite/c-Si tandem solar modules in both the 2T and 4T configuration.

Acknowledgements and contributions

The prototype FFS cloaks applied to CIGS solar modules and c-Si solar cells in this section were already published in Refs. [91,174]*. In Ref.* [174]*, the fabrication of the CIGS solar modules was performed at ZSW. Ben Breitung and Tobias Berger deposited the Al_2O_3 layer on top of the 3D-DLW master structures via atomic layer deposition. The fabrication of FFS stamps via 3D-DLW, photo-nanoimprint lithography and encapsulation via polymer bonding were performed by the author. FZJ Jülich fabricated the silicon solar cells used in the study about embedding FFS cloaks into the cover glass of solar modules* [91]*. The author carried out all experimental work on the fabrication of the FFS cloaks by imprinting into a glass-like resist, as well as by embedding them into cover glass fabricated via the liquid glass technique. The liquid glass precursor is supplied by Frederik Kotz and Patrick Risch from IMTEK Freiburg. Tobias Abzieher, Thomas Feeney, Ihteaz Hossain and Sara Moghadamzadeh deposited the electrodes, the CTLs and the absorber layer for the fabrication of thin-film perovskite solar cells on glass superstrates.*

7.1 Overview of investigated architectures

To begin with, this section provides an overview of fabrication techniques of FFS cloaks targeted for CIGS, c-Si and perovskite PV. In total, four prototype FFS cloaks (see **Figure 7.1**) are fabricated and characterized:

- **Architecture I:** a bare FFS cloak imprinted into the glass-like resist OrmoComp applied to a CIGS mini solar module,
- **Architecture II:** a FFS cloak optimized for embedment imprinted into OrmoComp and encapsulated under a PDMS layer and a cover glass applied to a CIGS mini solar module,
- **Architecture III:** a FFS cloak embedded into a cover glass fabricated via the liquid glass technique and laminated to a c-Si solar cell using EVA, and
- **Architecture IV:** a perovskite solar cell deposited on a glass superstrate with embedded FFS cloaks fabricated via the liquid glass technique.

Starting from the very first prototype of FFS cloaks fabricated on a c-Si solar cell [64], the concept of FFS cloaking is transferred to the monolithic interconnection lines of a CIGS thin-film solar module (see architecture I). The key hurdles during this step of development are the substantially larger dimensions of the cloak owing to the larger width of interconnection lines in CIGS solar modules compared to metallic finger grids of c-Si solar cells. Moving forward from the bare FFS cloak, architecture II aims at embedding the FFS cloak into the encapsulant. As outlined in Section 6.2, the embedment of a FFS cloak introduces significant parasitic reflection losses that can be minimized via two design optimizations: (1) truncation of the cloak and (2) reduction of the lateral extent via the cloak parameter R_2 (see Section 2.3). Architecture II makes use of the former optimization by truncating the cloak at an optimized height and then encapsulating it under a protective cover glass using a PDMS layer to mediate the contact between the cover glass and the FFS cloak. However, the use of the applied glass-like polymer OrmoComp on a commercial scale is not reasonable due to its high price. Therefore, alternative materials come into focus. Imprinting the FFS cloaks into the commercial standard polymeric encapsulant EVA is not feasible, since this material is liquefied in the subsequent lamination of the protective cover glass and the FFS cloak is not retained. A fully integrated, durable and, most importantly, compatible route to integrate FFS cloaks into the conventional architecture of solar modules becomes available by the emergence of liquid glass. This technique enables the embedment of FFS cloaks as cavities directly into the front cover glass. In architecture III, such front cover glass is laminated to c-Si solar cells with EVA. Considering the essential need to minimize the fabrication time of FFS master structures using DLW the alternative optimization of the design of embedded FFS cloaks via the cloak parameter R_2 is chosen from architecture III onwards, since it exhibits 51 % less volume compared to an optimized truncated FFS cloak as outlined in the preceding Chapter 6. Lastly, architecture IV represents the final technological challenge of processing a perovskite solar cell directly on a cover glass with embedded FFS cloaks for the application as the top-cell in a perovskite-based tandem solar module.

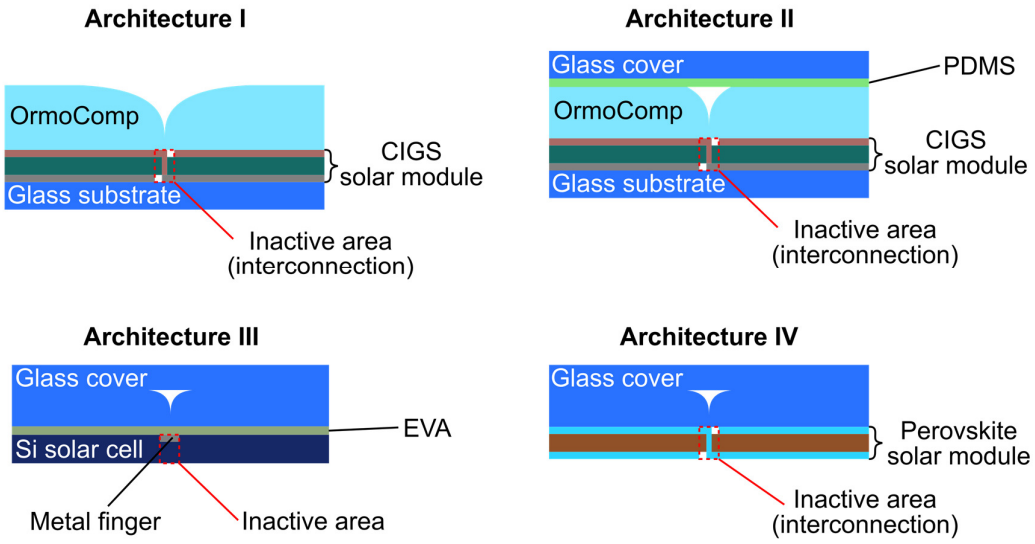

Figure 7.1: Overview of investigated architectures of Si, CIGS and perovskite solar cells and modules covered with FFS cloaks imprinted into an OrmoComp layer or embedded into the cover glass. FFS cloaks imprinted into an OrmoComp layer either are investigated bare, e.g. without encapsulation (architecture I), or encapsulated (architecture II).

7.2 Freeform surface cloaks imprinted into the encapsulant

Owing to the increased width of interconnection lines of thin-film solar modules (~200 µm) compared to screen-printed metallic fingers of c-Si solar cells (~50 µm), the transfer of FFS cloaks (definition in Chapter 6) from c-Si PV to CIGS thin-film PV (architecture I in **Figure 7.1**) requires the adaption of the design parameters of the FFS cloak. The investigated CIGS solar modules display a width of the interconnection lines of ~220 µm. Considering the width of a cell stripe of 4.7 mm, the inactive area constitutes a GFF of 4.7 %. To allow for imperfections during fabrication and misalignment of the FFS cloaks with regard to the metallic fingers, a tolerance of 80 µm is considered, which sums up to 300 µm that need to be cloaked. The optimum parameters for this width are R_1 = 150 µm, R_2 = 1500 µm and $y(0)$ = 150 µm according to design rules outlined in Section 2.3. In the following discussion, this set of parameters is referred to as the *original FFS cloak* with (encapsulated) and without (bare) cover glass. For the application to the CIGS thin-film solar module (device parameters provided in Ref. [174]), a master structure of nine FFS cloaks with a total area of 1.27 cm² is prepared via DLW. A PDMS replica of these master structures is then used to imprint the FFS cloaks into an OrmoComp layer via UV-NIL. The fabrication of the PDMS replica and the process and setup for UV-NIL are described in Sections 3.2.2 and 3.2.3, respectively. The inset of **Figure 7.2** shows a photograph of the resulting prototype. The efficient cloaking of the bright interconnection lines is readily identifiable from the absence of reflection in the cloaked area (blue rectangle). Contrary, the interconnection lines of the *planar reference* (red rectangle) reflect incident light distinctly. The impact of the FFS cloaks on the performance of the CIGS solar module manifests a significant increase in J_{SC} by 1.8 mA cm^{-2}, which correlates to 5.9 % relative. Owing to the excellent light incoupling properties of the *original FFS cloak without cover glass* (see Section 6.1), this even exceeds the theoretical gain of expected for just cloaking the inactive areas of $\zeta = \mathrm{GFF}/(1-\mathrm{GFF}) = 4.9$ %. Optical simulations (see Section 6.1) show that light incoupling and cloaking add to a theoretical gain of 5.4 % for a GFF of 4.7 %. The increase in J_{SC} is accompanied by an increase in PCE from 10.7 % to 11.6 %.

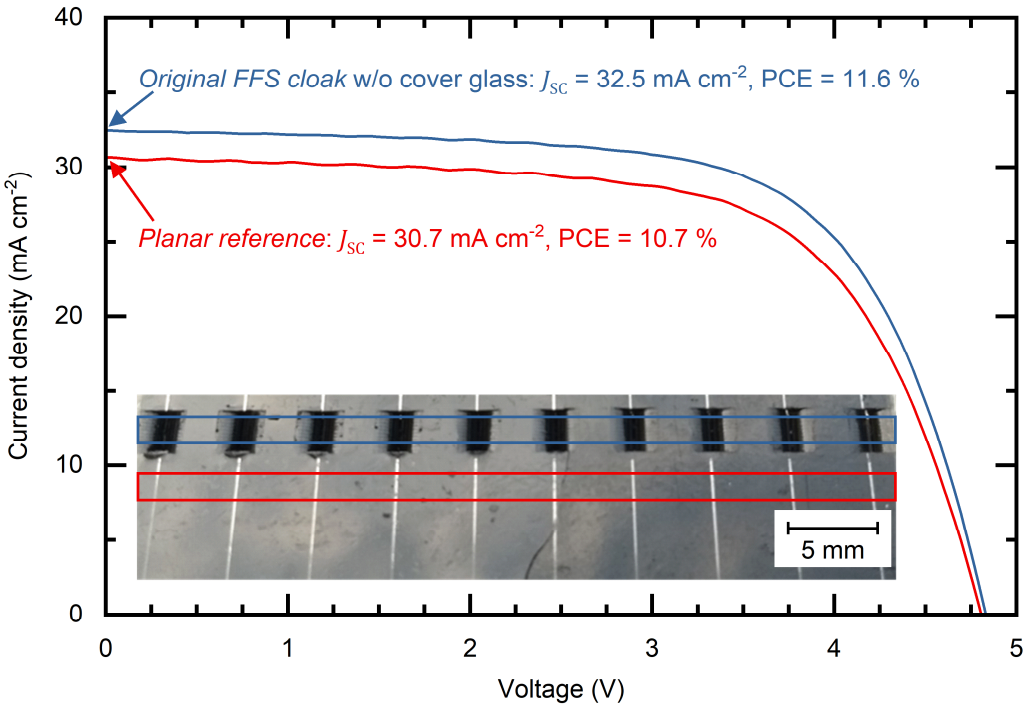

Figure 7.2: Measured current-density–voltage characteristic of a strip of a CIGS solar mini-module with the *original FFS cloak w/o cover glass* (blue) and a *planar reference* (red). Corresponding areas of the measurements are indicated by the rectangular boxes in the inset. Adapted with permission from [174]. © Elsevier 2018.

Regardless of the remarkable boost to solar module performance, this architecture is not applicable to realistic operation conditions. Due to the curved surface of the FFS cloak, its notch is potentially prone to soiling and the accumulation of dirt. Furthermore, standard front cover glasses for PV industry employ a planar front surface. Consequently, the incorporation of FFS cloaks into the conventional architecture of solar modules marks one of the key challenges for this technology. As a proof-of-concept, the given prototype of the FFS cloak is encapsulated under a planar front cover glass. A thin film of cured PDMS is used to bond the cover glass to the PDMS layer and the joint glass/PDMS encapsulation to the FFS cloak imprinted into OrmoComp. The process is described in Section 3.3.1. The flexibility of the thin PDMS film facilitates the elimination of air bubbles at the two interfaces. Nonetheless, a perfect interface remains challenging. In the inset of **Figure 7.3a**, a single CIGS cell stripe is shown once before (*original FFS cloak without cover glass*) and once after encapsulation with a front glass (*original FFS cloak with cover glass*).

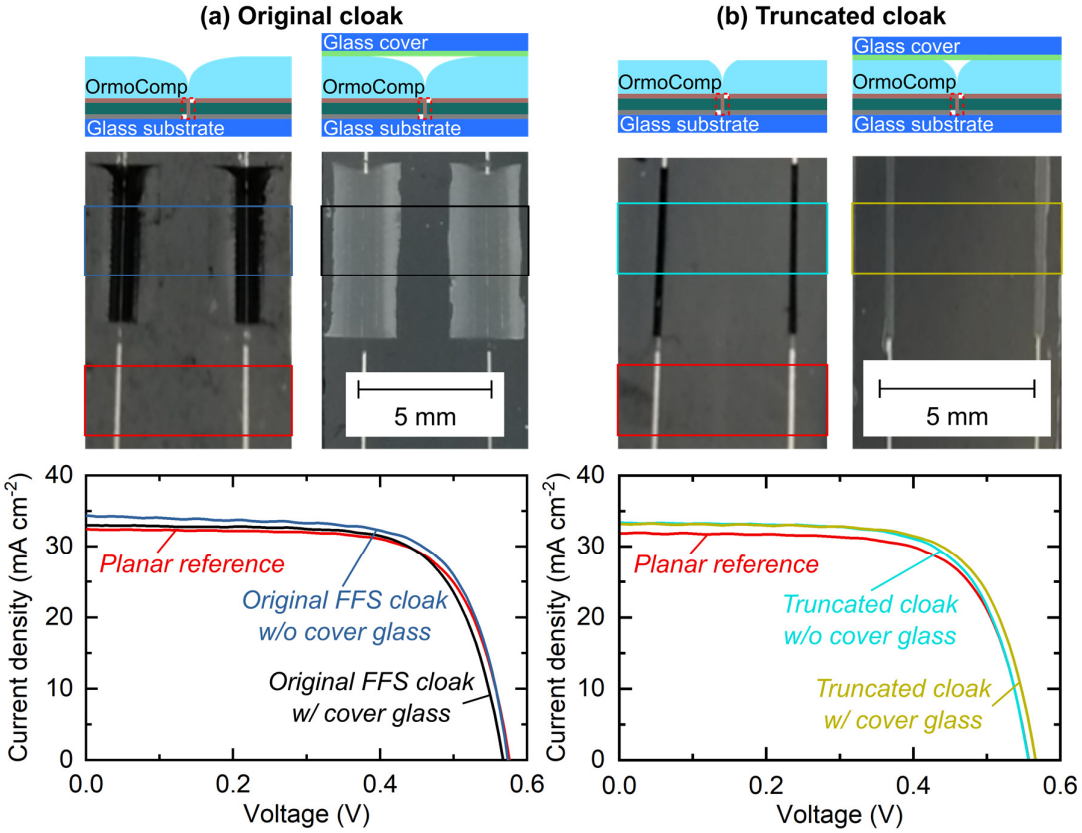

Figure 7.3: Measured current-density–voltage characteristics of prototypes of individual cell stripes of a CIGS solar module with (a) the *original FFS cloak* and (b) the *truncated FFS cloak*. Both designs are shown with and without a cover glass. Corresponding areas of the measurements are indicated by the rectangular boxes in the insets. Adapted with permission from [174]. © Elsevier 2018.

With regard to the optical performance, only the *bare original FFS cloak* results in a significant increase in J_{SC} of the CIGS cell stripe of $\zeta_{J_{\mathrm{SC}}}$ = 5.8 ± 0.4 %, which is in good agreement with both the aforementioned theoretical limit of 5.4 % and the previous result on nine interconnection lines of a CIGS solar module. In contrast, once encapsulated, the *original FFS cloak with cover glass* boosts the cell stripe's J_{SC} by mere 1.5 ± 0.4 %. The data of the correlated increase in PCE for both prototypes are provided in **Table 7.1**. The small gain of the FFS cloak once covered with a front glass clarifies the need for an optimization of the design parameters of the FFS cloak.

For the application to the CIGS cell stripe, an optimized truncation at a height of 435 µm is used so that the FFS cloak slightly exceeds the inactive area. This optimization is performed with regard to maximum power on the active area P_{total} at normal incidence, which means that the FFS cloak has the same lateral extent as the interconnection line (w = 220 µm). Once optimized the *truncated FFS cloak with cover glass* boasts a relative increase in J_{SC} of $\zeta_{J_{\mathrm{SC}}}$ = 4.1 ± 0.4 %, which is on par with that of the *truncated FFS cloak without cover glass* of $\zeta_{J_{\mathrm{SC}}}$ = 4.7 ± 0.4 %. The slightly lower relative increase in J_{SC} is to be expected due to the parasitic reflection loss at the two additional air/glass interfaces that the cavity introduces. The corresponding increase in PCE is provided in **Table 7.2**. It should be noted that the V_{OC} of the reported J-V characteristics is substantially lower than that of a fully illuminated solar module, since the shadow mask (area = 12.6 mm²), which is used to measure the FFS cloak and the *planar reference* separately, covers a large fraction (~85 %) of the active area. Additionally, the adjacent CIGS cell stripes are shunted intentionally for contacting the targeted cell stripe individually.

Table 7.1: Short circuit current densities (J_{SC}), power conversion efficiency (PCE) of the *original FFS cloak* with and without a cover glass and the corresponding relative increase of J_{SC} ($\zeta_{J_{SC}}$) and PCE (ζ_{PCE}) compared to the *planar reference*. Reprinted with permission from [174]. © Elsevier 2018.

	Planar reference	*Original FFS cloak without cover glass*	*Original FFS cloak with cover glass*
J_{SC} (mA cm^{-2})	32.5	34.4	33.0
PCE (%)	12.7	13.8	13.2
$\zeta_{J_{SC}}$	-	5.8	1.5
ζ_{PCE}	-	8.7	3.9

Table 7.2: Short circuit current densities (J_{SC}), power conversion efficiency (PCE) of the *truncated FFS cloak* with and without a cover glass and the corresponding relative increase of J_{SC} ($\zeta_{J_{SC}}$) and PCE (ζ_{PCE}) compared to the *planar reference*. Reprinted with permission from [174]. © Elsevier 2018.

	Planar reference	*Truncated FFS cloak without cover glass*	*Truncated FFS cloak with cover glass*
J_{SC} (mA cm^{-2})	31.9	33.4	33.2
PCE (%)	12.4	12.9	13.2
$\zeta_{J_{SC}}$	-	4.7	4.1
ζ_{PCE}	-	4.0	6.5

So far, the performance of the FFS cloaks on CIGS cell stripes have exclusively been investigated at normal incidence. However, oblique angles of incidence are an essential component of realistic operation conditions of solar modules. Even though the modification of the FFS design via truncation results in a boost of the J_{SC} at normal incidence, the ability of omnidirectional cloaking is compromised as illustrated by simulations in Section 6.2. Performing angle-dependent J-V measurements allows for the experimental confirmation of simulation results. The relative increase in J_{SC} of a CIGS cell stripe by applying the *original FFS cloak* with and without a cover glass, as well as the *truncated FFS cloak with cover glass*, provided in **Figure 7.4** show a good agreement with simulations. The *original FFS cloak without cover glass* (blue data) displays the largest relative increase in J_{SC} and its light incoupling ability at oblique angles of incidence benefits immensely from its non-planar surface. Nonetheless, the required cover glass for the compatibility with the application to photovoltaics diminishes the performance boost almost entirely, since parasitic reflection losses and cloaking of the inactive areas compensate each other. In particular, at oblique angles of incidence, the *original FFS cloak with cover glass* (black data) performs worse than the *planar reference*. The optimized truncation enables the recovery of most of the FFS cloak's boost to solar cell performance for angles of incidence $<30°$. For more oblique angles, the relative increase in J_{SC} by the *truncated FFS cloak with cover glass* (grey data) is close to zero, which means that it performs as well as the *planar reference*. For further optimization, energy yield modelling is of vital importance to identify the compromise between parasitic reflection losses and FFS cloaking across the entire angle range since it provides a route to consider the complex nature of diffuse realistic irradiation conditions.

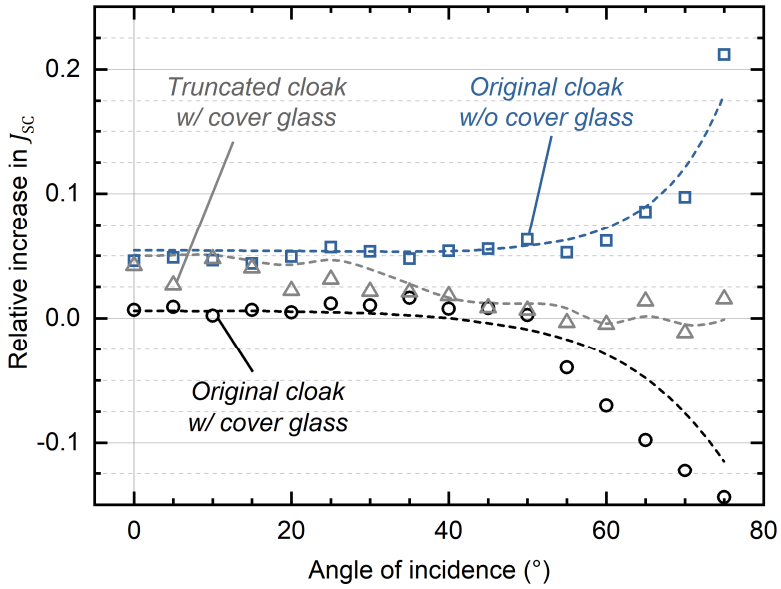

Figure 7.4: Relative increase of the J_{SC} of CIGS cells stripes with various designs of FFS cloaks (symbols) in dependence of the angle of incidence. For all designs, corresponding optical simulations (dashed lines) serve as references. Adapted with permission from [174]. © Elsevier.

7.3 Freeform surface cloaks embedded into liquid glass

The employment of the liquid glass technique marks the next milestone for the development of FFS cloaks compatible with the conventional architecture of solar modules sketched in **Figure 7.5a**. This technique enables the embedment of FFS cloaks in a fused silica glass slide. This way, a functionalized front cover glass for solar modules is manufactured that can be applied to photovoltaics just like any other standard front cover glass in industry. In this thesis, front cover glass with embedded FFS cloaks are fabricated via the liquid glass technique as a proof of concept. Compared to the approach of imprinting FFS cloaks into the polymeric encapsulant, the embedment of FFS cloaks into the cover glass promises an increased robustness and durability. A close-up view of the air void resulting from the embedment of a FFS cloak is shown in the microscope image in **Figure 7.5b**. The image demonstrates the excellent quality of transferring the FFS into fused silica glass using the technique outlined in Section 3.3.2. However, visual inspection on a larger scale (see **Figure 7.5c**) reveals the inclusion of small air bubbles originating from manual polymer bonding. The quality of the final cover glass may benefit from an automated and vacuum-assisted polymer bonding process, in particular with regard to upscaling. Other aspects concerning the sample quality are the planarity and surface roughness of the cover glass. The parameters are mostly affected by the surface quality of the glass slides and the attached plastic foils that are used to maintain a planar surface during the imprint of the FFS cloak into the liquid nanocomposite via UV-NIL. An in-depth discussion on these two parameters, in particular in the context of perovskite thin-film solar modules, follows later in this section.

Considering the necessity of upscaling, an alternative approach to optimize embedded FFS cloaks is pursued. Instead of optimized the lateral extent of the cavity by truncating the FFS at a certain height, the lateral extent of the FFS cloak is modified directly via the cloak parameter R_2 (please refer to Section 2.3). The optimization of R_2 reduces the volume of the FFS cloak by ~51 % (see Section 6.4) and speeds up the fabrication of master structures via DLW to the same extent. Once laminated to a monocrystalline silicon heterojunction solar cell with a standard polymeric encapsulant EVA, the setup corresponds to architecture III in **Figure 7.1**.

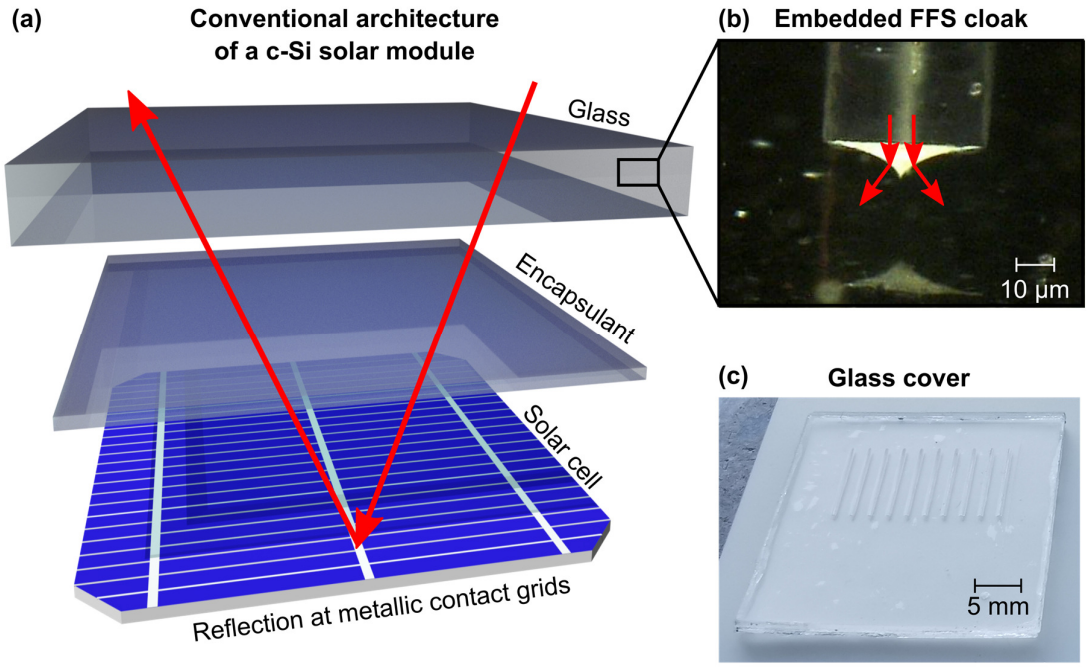

Figure 7.5: (a) Schematic of the conventional architecture of a c-Si solar module and an illustration of the reflection losses at metallic contact grids. (b) Microscope image of a FFS cloak embedded into a fused silica cover glass. (c) Photograph of a cover glass with embedded FFS cloaks fabricated via the liquid glass technique. Scales are indicated in each inset. Adapted with permission from [91]. © 2019 American Chemical Society.

In agreement with the ray-optical nature of the FFS cloak, the cover glass with embedded FFS cloaks boosts the measured EQE of the c-Si heterojunction solar cell over the entire wavelength range (see **Figure 7.6a**). Compared to the pristine solar cell, the EQE reduces due to parasitic absorption in the EVA and due to diminished anti reflection properties of the solar cell, whose front layers are optimized for air as the ambient medium. The strong parasitic absorption of EVA leads to a lower EQE in particular in the UV range. Since the layer thicknesses of the front layers are not optimized for encapsulation, the peak in EQE of the pristine c-Si solar cell around 650 nm is eliminated, which results in a flat EQE of the encapsulated c-Si solar cell across a broad wavelength range of 500 – 1000 nm. The increase in EQE is confirmed by the J-V characteristics of the three scenarios provided in **Figure 7.6b**. By encapsulating the pristine solar cell under the EVA encapsulant and the planar fused silica cover glass, around 2.4 mA cm^{-2} in J_{SC} are lost. However, introducing embedded FFS cloaks into the cover glass adds 1.2 mA cm^{-2} to the J_{SC} of the encapsulated c-Si solar cell. The relative increase in J_{SC} of both measurements cannot be compared directly, since the GFF of inactive areas with regard to the spot size differs. The home-built setup used for measuring the EQE of the c-Si solar cells generates a line spot with an area of 1 mm x 5 mm that crosses three metallic contact fingers with an average width of ~95 µm. With regard to the area of the spot, the inactive area sums up to 5.8 ± 0.3 %. A slightly lower GFF is apparent during J-V measurements. With regard to the area of the shadow mask of 13.4 mm x 2.5 mm that includes six contact fingers, the inactive area covers 4.4 ± 0.2 %. A detailed illustration is provided in Ref. [91]. Eventually, both measurements identify a significant increase in J_{SC} of 5.2 ± 0.5 % and 3.8 ± 0.5 % in the case of EQE and J-V characteristic, respectively, which corresponds to a cloaking efficiency of ~88 %. This value is quite remarkable under the consideration that perfect cloaking is not within reach due to parasitic reflection losses at the many air/glass interfaces of the cavity.

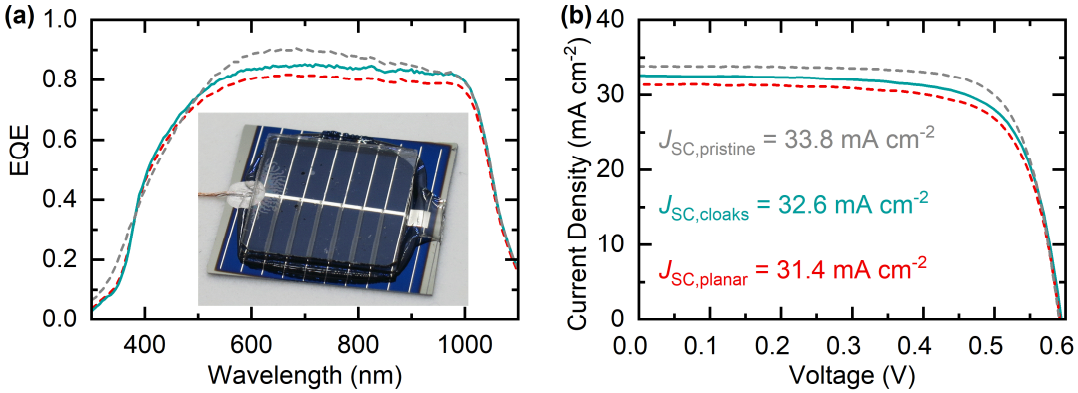

Figure 7.6: Measured external quantum efficiency (EQE) (a) and corresponding *J-V* characteristic (b) of a c-Si solar cell in a module environment under front cover glass with embedded FFS cloaks (light blue) compared to planar front cover glass fabricated via the LG technique (red). Additionally, data of the pristine solar cell is provided. Adapted with permission from [91]. © 2019 American Chemical Society.

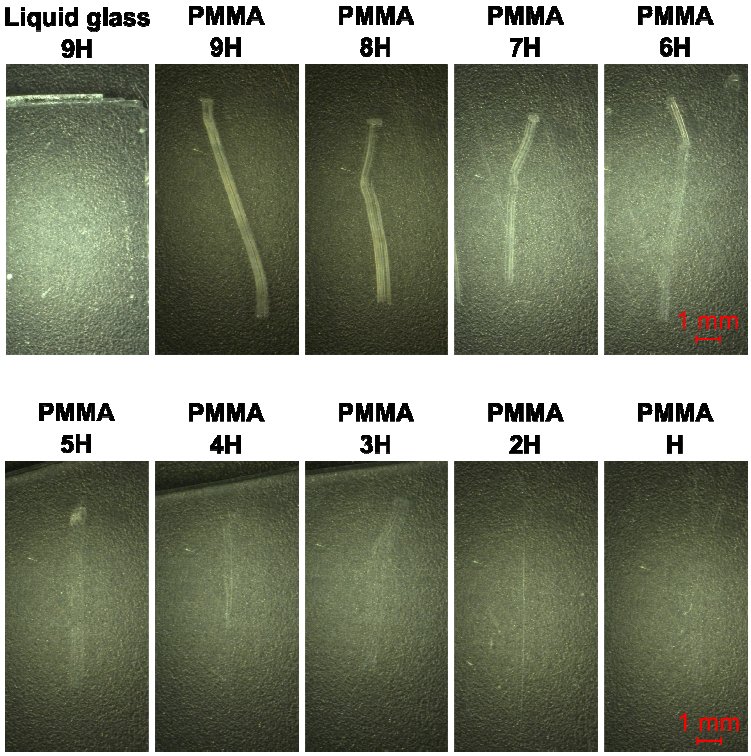

Figure 7.7: Photograph of pencil scratching tests (standard ASTM D3363) of a cover glass fabricated via the liquid glass technique and planar PMMA samples as a reference material. The combination of material and pencil hardness is indicated above each photograph. Adapted with permission from [91]. © 2019 American Chemical Society.

Scratch resistance

Next to efficiently cloaking inactive areas, mechanical stability and resilience towards realistic outdoor conditions is another crucial requirement for the application of front cover glass in PV installations. In early studies of fused silica glass fabricated via the liquid glass technique, a high Vickers hardness of 980 HV could be demonstrated. This Vickers hardness even overcomes that of conventional fused silica glass [93]. Pencil scratching tests according to the standard ASTM D3363 may provide a good starting point for further mechanical stability tests until standardized test routines on large scales such as IEC 61215 – including

bombardment with hailstones – become applicable to cover glass fabricated via the liquid glass technique. The procedure of scratching tests according to the standard ASTM D3363 are described in detail in Section 3.5 but also briefly recapitulated here. The scratching tests are conducted by firmly pushing lead pencils of decreasing hardness grades in the range of 9H to 9B across the samples (thickness ~800 µm). Then, the samples are visually inspected for scratching damage. Polymethylmethacrylate (PMMA), which is considered as one of the most suitable polymeric materials capable of introducing light management concepts to solar modules, is used as a reference [176]. The results shown in **Figure 7.7** reveal the strong scratch resistance of the fused silica glass fabricated via the liquid glass technique. Even with the hardest grade of the lead pencils, no structural damage can be inflicted on the material. In contrast, PMMA features a significantly lower scratch resistance. Only a medium pencil hardness of H leaves no visual sign of scratching damage. Consequently, the suitability of fused silica glass fabricated via the liquid glass technique is highlighted by its excellent scratch resistance.

The successful application of robust cover glass with embedded FFS cloaks to encapsulated solar cells demonstrates that this technique applicable to any other solar module that is encapsulated with a polymeric encapsulant and a protective cover glass. Possible PV technologies include among others CIGS and Si single-junction solar modules, as well as 2T perovskite/c-Si and perovskite/CIGS tandem solar modules.

Thin-film deposition on cover glass

The next step towards cloaking of inactive areas in 4T perovskite/c-Si tandem solar modules is the fabrication of thin-film perovskite solar cells (PSC) directly on glass superstrates with embedded FFS cloaks fabricated via the liquid glass technique. For perovskite-based 4T tandem solar modules, a deposition of the perovskite top-cell on a glass superstrate should be favored, since the process conditions of the front TCO and selective contact are not constraint then by the poor thermal stability of the perovskite as elaborated in Section 5.3. Therefore, a glass superstrate with embedded FFS cloaks fabricated via the liquid glass technique must exhibit a sufficient surface quality to support the deposition of conformal thin films.

Cover glass fabricated via the liquid glass technique may feature spikes that originate from the imprinting process. Even though these spikes are not recognizable, the AFM images provided in **Figure 7.8**, they are noticeable by manual inspection. Nonetheless, the apparent surface quality and a root mean square (RMS) surface roughness of 109.6 nm indicate that a deposition of conformal thin films is a challenge, especially for solution-based deposition techniques such as spin-coating. After mechanical polishing according to the procedure described in Section 3.3.2, the surface quality is improved significantly and exhibits a RMS surface roughness of 3.3 nm. The remaining spikes are most likely due to dust particles.

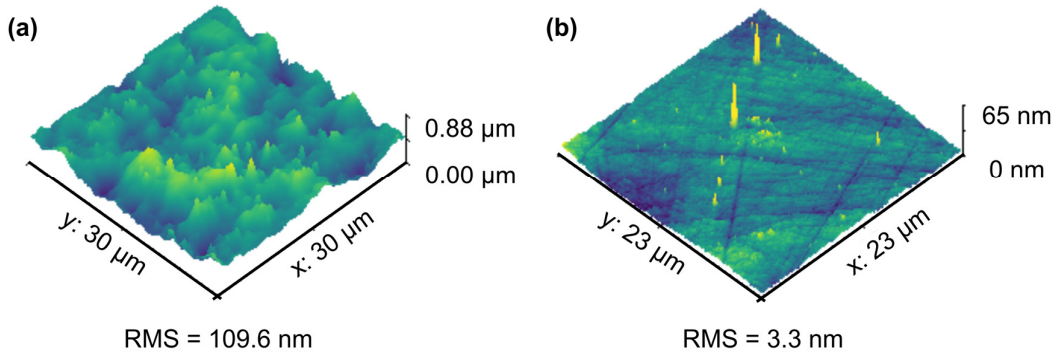

Figure 7.8: Atomic force microscopy images of cover glass fabricated via the liquid glass technique (a) before and (b) after mechanical polishing. The RMS surface roughness is indicated for both samples.

In view of the targeted upscaling of the cloaking concepts, evaporation is the method of choice to deposit the layers of the thin-film PSC on the cover glass fabricated via the liquid glass technique. The detailed process steps are provided in Section 3.4, but the architecture is briefly reviewed here. The front

contact grid of the PSC consists of ten 200 µm-wide gold (Au) fingers with a spacing of 2 mm. This results in a GFF of inactive areas of 10 %. The subsequent layers are 150 nm of ITO, 5 nm of 2,2',7,7'-tetra(*N,N*-di-*p*-tolyl)amino-9,9-spirobifluorene (Spiro-TTB), 500 nm of a coevaporated $CH_3NH_3PbI_3$ absorber, 21 nm of hole-blocking C_{60} and 5 nm of bathocuproine (BCP) and a 75 nm-thick Au rear metal contact [95].

Even though the fabricated PSCs are all short-circuited, the cloaking of inactive areas is confirmed by reflectance measurements, for which a spot of 1 mm x 4 mm is used that spans across two metal fingers. Consequently, the GFF of metal fingers is 10 % with regard to the spot size. The reflectance of an opaque perovskite solar cell reduces by up to 5 % compared to a *planar reference* as shown in **Figure 7.9**. However, the reduction of reflectance is limited to a narrow spectral range of ~500 – 800 nm, which is caused by two effects. On the one hand, the PSC becomes transparent for wavelengths longer than the bandgap wavelength (~800 nm) and all incident light is reflected by the rear metallization. On the other hand, the reflectance at the glass/gold interface significantly decreases for wavelengths $\lambda < 540$ nm and the incident light is most likely absorbed in the Au. Therefore, the effect of FFS cloaking is not detectable by reflectance measurements in this spectral range. In view of the GFF of the metal fingers, the cloaking efficiency of the prototype is 50 %, which is significantly lower than the cloaking efficiency of 88 % achieved for c-Si solar cells reported above. A probable source for imperfect cloaking via any optical concept is misalignment of the FFS cloak with regard to the inactive area. In fact, when inspecting the inset of **Figure 7.9** closely, a small misalignment of the FFS cloak and the metal fingers is noticeable, even though the FFS cloaks are designed with a tolerance in the width of the cloaked area of 100 µm.

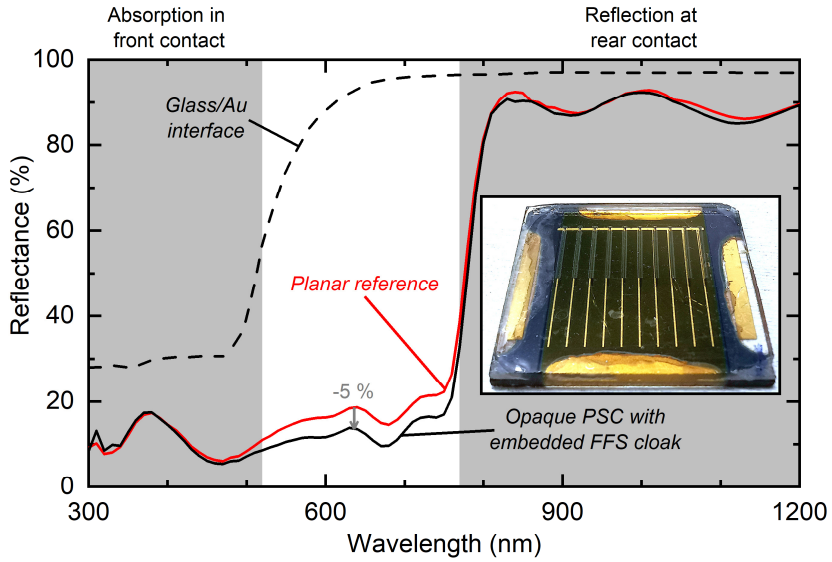

Figure 7.9: Reflectance of an opaque perovskite solar cell on a glass superstrate with embedded FFS cloaks (black) compared to a *planar reference* (red). Furthermore, the reflectance of unpolarized light at a glass/Au interface based on Fresnel's Equations is provided (dashed line). Due to the vanishing reflectance of the metal fingers in the short wavelength range and the strong reflectance at the rear contact in the long wavelength range, the spectral range of reduced reflectance of the cloaked perovskite cell (white background) reduces to ~500 – 800 nm.

Contrary to the architecture of the perovskite top-cell in conventional 4T perovskite/c-Si tandem solar modules, the investigated PSC features metallic contact fingers instead of interconnection lines. Therefore, the PSCs should be fabricated with interconnection lines instead of an evaporated Au grid in a next step. Laser scribing of the interconnection lines promises to improve alignment drastically due to a possible automated positioning of the laser beam on the micrometer scale. Additionally, since interconnection lines run through the entire layer stack, the distinction between front and rear inactive areas does not apply and the alignment of front and rear inactive areas is not of relevance.

7.4 Summary

In summary, this chapter demonstrates several prototypes of FFS cloaks applied to solar cells and modules with the goal to establish architectures and fabrication processes compatible with the architecture of 2T and 4T perovskite/c-Si tandem solar modules. As a first step towards this goal, a FFS cloak based on the optimum parameters derived by Schumann et al. [60] is applied to CIGS thin-film solar modules by imprinting the FFS cloak into an encapsulating, polymeric layer. This prototype demonstrates that the concept of FFS cloak is feasible for such large inactive areas as the ∼200 µm-wide interconnection lines of thin-film solar modules by an increase in J_{SC} of 5.9 % compared to a planar reference for a GFF of inactive area of 4.7 %. In addition to cloaking, the increased light incoupling due to the FFS cloak's curved surface contributes to this large increase in J_{SC} as described in Section 6.1.

To reduce the solar module's susceptibility to soiling, the initial design is then embedded under a protective cover glass by plasma bonding of the polymer FFS cloak and the cover glass. In order to minimize the strong parasitic reflection losses introduced by this embedment, the design needs to be adapted. Once the design of the FFS cloak is optimized, the CIGS solar module with embedded FFS cloaks outperforms the planar reference by 4.1 % [174].

Furthermore, a fabrication process – the liquid glass technique – that enables the embedment of FFS cloaks into the robust cover glass is established in the field of PV and successfully demonstrated by laminating the fabricated cover glass to c-Si solar cells [91]. The encapsulated c-Si solar cells feature a larger J_{SC} by 3.8 % than a planar reference for a GFF of inactive area of 4.4 %. Compared to imprinting a FFS cloak into the polymeric encapsulant, this approach displays a more robust integration of the FFS cloak in to the architecture of the solar module. The cover glass exhibits a good resilience towards scratching damage, in particular when compared to PMMA, which serves as a reference material. In general, this architecture is practicable for any PV technology relying on a polymeric encapsulant and a protective cover glass for module encapsulation, among others 2T perovskite/c-Si tandem solar modules.

Having shown both the effective cloaking of inactive areas via FFS cloaks and successful embedment of FFS cloaks into the robust cover glass, the deposition of PSCs on glass superstrates fabricated via the liquid glass technique is pursued in a next step towards cloaked inactive areas of 4T perovskite/c-Si tandem solar modules. Since the perovskite top-cell is preferably processed on a glass superstrate (see Section 5.3), the cover glass fabricated via the liquid glass technique require a smooth surface to support the deposition of conformal thin films. Mechanical polishing of cover glass fabricated via the liquid glass technique is investigated to prepare its surface for the deposition of thin-film PSCs. However, PSCs deposited on the polished glass superstrates are short-circuited. Nevertheless, the impact of the embedded FFS cloaks on the reflectance of the PSC is quantified. In a wavelength range, where the effect of cloaking is measurable via spectrophotometry, the FFS cloak reduces reflectance by up to 5 % for a GFF of inactive areas of 10 %, which indicates poor alignment of the FFS cloaks with regard to the inactive areas. However, moving from metal grids to laser-scribed interconnection lines promises to improve alignment significantly in future work. Even though effective cloaking of inactive areas of PSCs via embedded FFS cloaks is successfully demonstrated, the deposition of functioning PSCs on glass superstrates fabricated via the liquid glass technique remains a challenge for the future.

8 Conclusion

This thesis reports on optical cloaking of inactive areas by FFS cloaks for the application in perovskite/c-Si tandem solar modules. An analysis of optical losses in perovskite/c-Si tandem solar modules via optical simulations and EY modelling is performed to compare cloaking of inactive areas with the reduction of other optical losses, such as reflection, parasitic absorption and current matching. Furthermore, optical simulations are used to establish the understanding of the working principle of FFS cloaks. Based on the gained knowledge, two designs of FFS cloaks are proposed, which are compatible with the conventional architecture of perovskite/c-Si tandem solar modules due to their embedment into the encapsulation layers of solar modules. Additionally, this thesis presents prototypes of FFS cloaks imprinted into the polymeric encapsulant and FFS cloaks embedded into the protective cover glass of solar modules via the liquid glass technique.

8.1 Summary and discussion

Below, the three main results of this thesis are summarized and discussed in the context of current developments in the field perovskite-based tandem solar modules.

Light management in perovskite-based tandem solar modules

Optical losses in perovskite/c-Si tandem solar modules associated to reflection, parasitic absorption, current matching of 2T tandem solar modules and inactive areas are quantified by means of self-written optical simulations, individually and as part of an EY modelling framework. For each optical loss mechanism, the development of architectures and materials is discussed for the example of the representative state-of-the-art devices modelled from literature [26,27].

The results show that optical losses due to parasitic absorption and shading by inactive areas are the largest optical loss mechanisms, while losses in J_{SC} due to reflection are minimized efficiently to values of 4 % by pyramidal texturing of the c-Si bottom-cell and the incorporation of ARCs. Parasitic absorption accounts for a loss in J_{SC} of 7 % and 8 % for 2T and 4T perovskite/c-Si tandem solar modules, respectively. This loss in J_{SC} correlates to a loss of the same magnitude in annual EY. Compared to materials used in early prototypes, the representative state-of-the-art perovskite/c-Si tandem solar modules already present a considerable improvement in terms of parasitic absorption losses. However, employing optically superior TCO materials complemented by metallic grids or the fabrication of thinner conformal layers of CTLs promise a further reduction of parasitic absorption losses [124,155].

Furthermore, the investigation of losses associated to current matching in 2T devices reveals that an optimization of the architecture of a representative 2T perovskite/CIGS tandem solar module results in a drastic reduction of current matching losses. Consequently, the 2T device employing $CH_3NH_3PbI_3$ with an optimized thickness produces an EY ∼3.5 % lower than that of a 4T device averaged over a large variety of locations in the United States, which cover a wide range of climatic zones. The EY modelling further shows that perovskite bandgaps of ∼1.7 – 1.8 eV facilitates current matching considerably and reduces the relevance of optimizing the thickness of the perovskite absorber layer. The annual EY of perovskite-based tandem solar modules in the 2T and 4T configuration balance out, when perovskite absorbers with a bandgap in this optimum range are employed. This means that the battle for the superior configuration of perovskite-based tandem solar modules is most probably decided by economic factors, such as fabrication costs and integration into existing fabrication lines, rather than by the maximum EY.

Apart from the large loss mechanism of parasitic absorption, inactive areas are another major source of losses in solar modules in general and reduce the active area, and thus the annual EY, by up to 16 %. Around third of the inactive area loss is associated to metallic contact grids and interconnection lines (∼5 % of the total area). Even though effort is invested to reduce the optical footprint of metallic contact grids and interconnection lines, optical cloaking promises a significant potential boost to the annual EY of perovskite-based tandem solar modules.

Working principle of freeform surface cloaks

With the goal of FFS cloaks that are compatible with conventional architectures of solar modules and simultaneously resilient to soiling losses, a new design of FFS cloaks starting from the *original bare FFS cloak* designed by M. Schumann *et al.* [60] needs to be designed. Therefore, the understanding of the working principle of bare FFS cloaks is established first. Due to its curved surface, the *original bare FFS cloak* not only shows omnidirectional cloaking, but also demonstrates excellent light incoupling properties, in particular at large angles of incidence. In terms of cloaking and light incoupling, the *original bare FFS cloak* features the

ideal optical performance. However, the curved surface of the FFS cloak increases its susceptibility to soiling and the accumulation of dirt.

The established understanding of the working principle of FFS cloaks is used to modify its design for the embedment under a protective cover glass. Embedding the FFS cloak into the cover glass provides a planar front surface and, thus, reduces the device's susceptibility to soiling to levels of commercial solar modules. However, the embedment comes at the cost of increased reflection losses due to the large area of air/cloak interfaces. The amount of reflection losses is minimized by reducing the lateral extent of the FFS cloak via design modifications: (1) a truncation of the height (cutoff) of the FFS cloak, which effectively reduce the lateral extent, and (2) an optimization of the cloak parameter R_2, which directly represents the lateral extent. Once optimized, both designs of FFS cloaks exhibit a relative increase in power on the active area P_{total} of 3.5 % at normal incidence for a considered GFF of inactive areas of 4 %. However, due to the modification of the design of the FFS cloaks, they do not feature perfect omnidirectional cloaking anymore. At oblique angles of incidence, the optical performance of both designs keeps the balance. While the *embedded FFS cloak with optimized cutoff* performs better at angles of incidence below 60° in terms of P_{total}, the *embedded FFS cloak with optimized* R_2 has superior angular stability and outperforms the former at angles of incidence above 60°.

To identify the superior out of the two proposed design modifications under realistic irradiation conditions, EY modelling of a representative 4T perovskite/c-Si tandem solar module with FFS cloaks is carried out. Both modification approaches yields a relative increase in EY of 2.4 % compared to a planar reference. The successful cloaking of inactive areas under realistic irradiation conditions liberates the compromised front contacting scheme of solar modules in general. Usually, the front contact scheme is a compromise of small inactive area losses defined by spacing between inactive areas and low resistance losses defined by the TCO thickness. Since embedded FFS cloaks effectively reduce the amount of inactive areas, the spacing between inactive areas can be reduced while simultaneously reducing the TCO thickness until a new optimal front contacting scheme emerges. In the case of the representative 4T perovskite/c-Si tandem solar module, the spacing of inactive areas is reduced from 5 mm to 1.8 mm. The TCO thickness from initially 200 nm reduces to the same extent. While the EY of the *planar reference* reduces with smaller spacing due to increased GFF of inactive areas, the EY of the optimized front contact scheme is 3.1 % higher than the maximum EY of the *planar reference*.

Embedded FFS cloaks applied in perovskite-based tandem solar modules

Within the scope of this thesis, prototypes of FFS cloaks applied to various PV technologies are fabricated with the goal to establish fabrication techniques compatible with the architecture of state-of-the-art 2T and 4T perovskite/c-Si tandem solar modules.

First, the concept of FFS cloaks is successfully applied to the interconnection lines of CIGS thin-film solar modules to demonstrate that FFS cloaks are in theory applicable to any dimension of inactive areas. For this prototype, the FFS cloak is imprinted into the polymeric encapsulant. The *original bare FFS cloak* improves the J_{SC} of the CIGS solar module by 5.9 % with regard to a GFF of inactive areas of 4.7 %. The *original bare FFS cloak* features the ideal optical performance, since it combines omnidirectional cloaking with excellent light incoupling. However, the *original bare FFS cloak* exhibits an increased susceptibility to soiling due to its non-planar surface. To increase resilience to soiling, embedded FFS cloaks are presented by covering a modified FFS cloak with a protective cover glass. Even though, the embedment of the FFS cloak increases reflection losses, the resulting increase in J_{SC} of 4.1 % is still remarkable.

Additionally, an alternative fabrication technique to embed FFS cloaks into the protective cover glass – the liquid glass technique – is applied. This technique allows the embedment of FFS cloaks directly into the robust cover glass. A good compatibility with conventional encapsulation techniques of solar modules is the consequence, since the cover glass fabricated via the liquid glass technique can be laminated in the very

same way as conventional cover glass. Furthermore, the material is characterized by an outstanding resilience towards scratching damage, which underlines its suitability to outdoor applications. Laminating the cover glass with embedded FFS cloaks fabricated via the liquid glass technique to c-Si heterojunction solar cells results in a noticeable increase in J_{SC} of 3.8 % compared to a planar reference. Considering a GFF of inactive areas of 4.4 %, this increase in J_{SC} corresponds to a cloaking efficiency of ~88 %.

The established process of embedding FFS cloaks into the cover glass via the liquid glass technique poses a viable option for 2T perovskite/c-Si tandem solar modules, since these are most likely contacted in the very same way as c-Si single-junction solar modules, which are by standard encapsulated by laminating the cover glass using a polymeric encapsulant. However, 2T perovskite/c-Si tandem solar cells or modules have not been available within the timeframe of this thesis, but the high cloaking efficiency achieved for c-Si single-junction solar cells demonstrates the effectiveness for the very similar contacting scheme of 2T perovskite/c-Si tandem solar modules.

As a next step towards cloaking of inactive areas in 4T perovskite/c-Si tandem solar modules via embedded FFS cloaks, the deposition of PSCs on a glass superstrate fabricated via the liquid glass technique is performed. In 4T perovskite/c-Si tandem solar modules the preferable deposition of the perovskite top-cell on a glass superstrate (see Section 5.3), which also acts as the cover glass, renders the use of a polymeric encapsulant superfluous. For thin-film deposition, the surface of the cover glass has to exhibit a quality that supports the deposition of conformal thin films. Therefore, grinding and polishing of glass superstrates fabricated via the liquid glass technique is pursued. Even though the fabricated PSCs are short-circuited, the ability of the FFS cloak to guide the incident light towards the active area is confirmed via reflectance measurements. The reflectance of the PSC is reduced by 5 %. Considering a GFF of inactive area of the PSC of 10 %, this reduction in reflectance corresponds to a cloaking efficiency of 50 %, which highlights the severe issue of precise alignment of FFS cloaks and inactive areas. In fact, alignment is identified as a key challenge and a major disadvantage of any optical cloaking concept compared to the alternative of tailored contacts.

8.2 Outlook

Having shown – both theoretically and experimentally – by the example of CIGS, c-Si and perovskite single-junction solar cells that embedded FFS cloaks effectively reduce optical losses due to inactive areas of solar modules, some challenges to overcome and some possibilities to explore remain for future work. In particular, the development of new front contacting schemes of perovskite/c-Si tandem solar modules with a larger number of metallic contact fingers in the 2T configuration or a larger number of interconnection lines in the 4T configuration represents an interesting opportunity enabled by embedded FFS cloaks.

At present, the concept of embedded FFS cloaks faces three major challenges: (1) time-consuming fabrication of master structures using DLW, (2) large-scale fabrication of embedded FFS cloaks, and (3) alignment of FFS cloaks with regard to the inactive areas.

Regarding the first challenge, tremendous efforts are invested to advance DLW to be of use on an industrial scale. In particular, the development of two-photon grayscale lithography promises a considerable boost to fabrication times of FFS cloaks since it enables the ultra-fast fabrication of freeform microstructures on industrial scale [177]. Nonetheless, high-precision milling may be an interesting alternative, since it enables the fabrication of more durable metallic master structures compared to the DLW master structures comprised of cured resist. The fabrication of metallic master structures has the additional benefit of reducing the number of process steps by eliminating the transfer of master structures into a PDMS stamp, since a milled metallic master is directly usable as a stamp for UV-NIL. Alternatively, the fabrication of master stamps by powder bed fusion may be an interesting and highly innovative technique to fabricate more robust and durable master stamp than the currently used PDMS [178]. However, commercial machines yet do not feature the required resolution to be straightforwardly applicable for optical cloaking concepts [179].

Closely related to the time-consuming fabrication of master structures is the second challenge of large-scale fabrication of FFS cloaks. Even though further research efforts have to be invested to fabricate PSCs successfully on robust cover glass fabricated via the liquid glass technique, cover glass with embedded FFS cloaks represents the most promising approach to cloak inactive areas of the perovskite top-cell in 4T perovskite/c-Si tandem solar modules. Furthermore, it represents the most durable approach to integrate optical cloaking concepts into the architecture of both 2T and 4T perovskite/c-Si tandem solar modules under the natural thermal cycling of outdoor conditions [91]. For 2T devices, an embedment of optical concepts into polymeric encapsulants other than the market standard EVA, such as PDMS, during the lamination process may be an alternative to the embedment into the cover glass but represents a major technological challenge.

Lastly, precise alignment of optical cloaking concepts with regard to the inactive areas is a key issue. For 4T perovskite/c-Si tandem solar modules, laser scribing of the interconnection lines of the perovskite top-cell promises to facilitate precise alignment due to the automated positioning on the micrometer scale of the laser beam used. Alignment of a cover glass with embedded FFS cloaks with regard to the metallic contact grids of 2T perovskite/c-Si tandem solar modules, however, may only be solved by optically assisted positioning of the cover glass during lamination. Given the fact that the FFS cloak may be designed in a way that it considers a certain tolerance of for example 100 µm, precise alignment of FFS cloaks and inactive areas seems manageable.

References

1. *BP Statistical Review of World Energy Statistical Review of World* (2019).

2. *World Energy Outlook 2018* (2018).

3. S. Philips and W. Warmuth, *Fraunhofer ISE: Photovoltaics Report 2019* (2019), (March).

4. C. Kost, J. N. Mayer, J. Thomsen, N. Hartmann, C. Senkpiel, S. Philipps, S. Nold, S. Lude, N. Saad, and T. Schlegel, *Levelized Cost of Electricity: Renewable Energy Technologies* (2018), (March).

5. *International Technology Roadmap for Photovoltaic (ITRPV)* (2019), (10th Edition).

6. M. A. Green, "Limits on the open-circuit voltage and efficiency of silicon solar cells imposed by intrinsic Auger processes," IEEE Trans. Electron Devices **31**(5), 671–678 (1984).

7. A. Richter, M. Hermle, and S. W. Glunz, "Reassessment of the Limiting Efficiency for Crystalline Silicon Solar Cells," IEEE J. Photovoltaics **3**(4), 1184–1191 (2013).

8. A. D. Vos and A. De Vos, "Detailed balance limit of the efficiency of tandem solar cells," J. Phys. D. Appl. Phys. **13**(5), 839 (1980).

9. M. Langenhorst, B. Sautter, R. Schmager, J. Lehr, E. Ahlswede, M. Powalla, U. Lemmer, B. S. Richards, and U. W. Paetzold, "Energy yield of all thin-film perovskite/CIGS tandem solar modules," Prog. Photovoltaics Res. Appl. **27**(4), 290–298 (2019).

10. M. a. Green, A. Ho-Baillie, and H. J. Snaith, "The emergence of perovskite solar cells," Nat. Photonics **8**(7), 506–514 (2014).

11. M. Grätzel, "The light and shade of perovskite solar cells," Nat. Mater. **13**(9), 838–842 (2014).

12. D. P. McMeekin, G. Sadoughi, W. Rehman, G. E. Eperon, M. Saliba, M. T. Horantner, A. Haghighirad, N. Sakai, L. Korte, B. Rech, M. B. Johnston, L. M. Herz, and H. J. Snaith, "A mixed-cation lead mixed-halide perovskite absorber for tandem solar cells," Science **351**(6269), 151–155 (2016).

13. N. N. Lal, Y. Dkhissi, W. Li, Q. Hou, Y. B. Cheng, and U. Bach, "Perovskite Tandem Solar Cells," Adv. Energy Mater. **7**(18), 1–18 (2017).

14. S. Albrecht and B. Rech, "Perovskite solar cells: On top of commercial photovoltaics," Nat. Energy **2**(1), (2017).

15. J.-P. Correa-Baena, M. Saliba, T. Buonassisi, M. Grätzel, A. Abate, W. Tress, and A. Hagfeldt, "Promises and challenges of perovskite solar cells," Science **358**(6364), 739–744 (2017).

16. G. E. Eperon, M. T. Hörantner, and H. J. Snaith, "Metal halide perovskite tandem and multiple-junction photovoltaics," Nat. Rev. Chem. **1**(12), 0095 (2017).

17. J. Werner, B. Niesen, and C. Ballif, "Perovskite/Silicon Tandem Solar Cells: Marriage of Convenience or True Love Story? - An Overview," Adv. Mater. Interfaces **5**(1), 1700731 (2018).

18. S. Essig, C. Allebé, T. Remo, J. F. Geisz, M. A. Steiner, K. Horowitz, L. Barraud, J. S. Ward, M. Schnabel, A. Descoeudres, D. L. Young, M. Woodhouse, M. Despeisse, C. Ballif, and A. Tamboli, "Raising the one-sun conversion efficiency of III–V/Si solar cells to 32.8% for two junctions and 35.9% for three junctions," Nat. Energy **2**(9), 17144 (2017).

19. "NREL Efficiency Chart," https://www.nrel.gov/pv/assets/pdfs/best-research-cell-efficiencies.20190923.pdf (accessed October 3, 2019).

20. T. C.-J. J. Yang, P. Fiala, Q. Jeangros, and C. Ballif, "High-Bandgap Perovskite Materials for Multijunction Solar Cells," Joule **2**(8), 1421–1436 (2018).

21. M. H. Futscher and B. Ehrler, "Efficiency Limit of Perovskite/Si Tandem Solar Cells," ACS Energy Lett. **1**(4), 863–868 (2016).

22. M. H. Futscher and B. Ehrler, "Modeling the Performance Limitations and Prospects of Perovskite/Si Tandem Solar Cells under Realistic Operating Conditions," ACS Energy Lett. **2**(9), 2089–2095 (2017).

23. M. T. Hörantner and H. J. Snaith, "Predicting and optimising the energy yield of perovskite-on-silicon tandem solar cells under real world conditions," Energy Environ. Sci. **10**(9), 1983–1993 (2017).

24. J. Lehr, M. Langenhorst, R. Schmager, S. Kirner, U. Lemmer, B. S. Richards, C. Case, and U. W. Paetzold, "Energy yield modelling of perovskite/silicon two-terminal tandem PV modules with flat and textured interfaces," Sustain. Energy Fuels **2**(12), 2754–2761 (2018).

25. O. Dupré, B. Niesen, S. De Wolf, and C. Ballif, "Field Performance versus Standard Test Condition Efficiency of Tandem Solar Cells and the Singular Case of Perovskites/Silicon Devices," J. Phys. Chem. Lett. **9**(2), 446–458 (2018).

26. T. Duong, Y. L. Wu, H. Shen, J. Peng, X. Fu, D. Jacobs, E.-C. C. E. C. Wang, T. C. Kho, K. C. Fong, M. Stocks, E. Franklin, A. Blakers, N. Zin, K. McIntosh, W. Li, Y. B. Y.-B. B. Cheng, T. P. White, K. Weber, and K. Catchpole, "Rubidium Multication Perovskite with Optimized Bandgap for Perovskite-Silicon Tandem with over 26% Efficiency," Adv. Energy Mater. **7**(14), 1700228 (2017).

27. F. Sahli, J. Werner, B. A. Kamino, M. Bräuninger, R. Monnard, B. Paviet-Salomon, L. Barraud, L. Ding, J. J. Diaz Leon, D. Sacchetto, G. Cattaneo, M. Despeisse, M. Boccard, S. Nicolay, Q. Jeangros, B. Niesen, and C. Ballif, "Fully textured monolithic perovskite/silicon tandem solar cells with 25.2% power conversion efficiency," Nat. Mater. **17**(9), 820–826 (2018).

28. M. Jaysankar, M. Filipič, B. Zielinski, R. Schmager, W. Song, W. Qiu, U. W. Paetzold, T. Aernouts, M. Debucquoy, R. Gehlhaar, and J. Poortmans, "Perovskite–silicon tandem solar modules with optimised light harvesting," Energy Environ. Sci. **11**(6), 1489–1498 (2018).

29. C. O. Ramírez Quiroz, Y. Shen, M. Salvador, K. Forberich, N. Schrenker, G. D. Spyropoulos, T. Heumüller, B. Wilkinson, T. Kirchartz, E. Spiecker, P. J. Verlinden, X. Zhang, M. A. Green, A. Ho-Baillie, and C. J. Brabec, "Balancing electrical and optical losses for efficient 4-terminal Si–perovskite solar cells with solution processed percolation electrodes," J. Mater. Chem. A **6**(8), 3583–3592 (2018).

30. B. Chen, Z. Yu, K. Liu, X. Zheng, Y. Liu, J. Shi, D. Spronk, P. N. Rudd, Z. Holman, and J. Huang, "Grain Engineering for Perovskite/Silicon Monolithic Tandem Solar Cells with Efficiency of 25.4%," Joule **3**(1), 177–190 (2019).

31. M. Jošt, E. Köhnen, A. B. Morales-Vilches, B. Lipovšek, K. Jäger, B. Macco, A. Al-Ashouri, J. Krč, L. Korte, B. Rech, R. Schlatmann, M. Topič, B. Stannowski, and S. Albrecht, "Textured interfaces in monolithic perovskite/silicon tandem solar cells: advanced light management for improved efficiency and energy yield," Energy Environ. Sci. **11**(12), 3511–3523 (2018).

32. "Perovskite world record of 28% | Oxford PV," https://www.oxfordpv.com/news/oxford-pv-perovskite-solar-cell-achieves-28-efficiency (accessed June 18, 2019).

33. K. Yoshikawa, W. Yoshida, T. Irie, H. Kawasaki, K. Konishi, H. Ishibashi, T. Asatani, D. Adachi, M. Kanematsu, H. Uzu, and K. Yamamoto, "Exceeding conversion efficiency of 26% by heterojunction interdigitated back contact solar cell with thin film Si technology," Sol. Energy Mater. Sol. Cells **173**, 37–42 (2017).

34. Q. Han, Y.-T. Hsieh, L. Meng, J.-L. Wu, P. Sun, E.-P. Yao, S.-Y. Chang, S.-H. Bae, T. Kato, V. Bermudez, and Y. Yang, "High-performance perovskite/Cu(In,Ga)Se 2 monolithic tandem solar cells," Science **361**(6405), 904–908 (2018).

35. T. P. White, N. N. Lal, and K. R. Catchpole, "Tandem Solar Cells Based on High-Efficiency c-Si Bottom Cells: Top Cell Requirements for Efficiency," IEEE J. Photovoltaics **4**(1), 208–214 (2014).

36. N. N. Lal, T. P. White, and K. R. Catchpole, "Optics and Light Trapping for Tandem Solar Cells on Silicon," IEEE J. Photovoltaics **4**(6), 1380–1386 (2014).

37. P. Löper, B. Niesen, S.-J. Moon, S. Martin de Nicolas, J. Holovsky, Z. Remes, M. Ledinsky, F.-J. Haug, J.-H. Yum, S. De Wolf, and C. Ballif, "Organic-Inorganic Halide Perovskites: Perspectives for Silicon-Based Tandem Solar Cells," IEEE J. Photovoltaics **4**(6), 1545–1551 (2014).

38. B. W. Schneider, N. N. Lal, S. Baker-Finch, and T. P. White, "Pyramidal surface textures for light trapping and antireflection in perovskite-on-silicon tandem solar cells," Opt. Express **22**(S6), A1422 (2014).

39. S. Albrecht, M. Saliba, J.-P. Correa-Baena, K. Jäger, L. Korte, A. Hagfeldt, M. Grätzel, and B. Rech, "Towards optical optimization of planar monolithic perovskite/silicon-heterojunction tandem solar cells," J. Opt. **18**(6), 064012 (2016).

40. R. Saive, A. M. Borsuk, H. S. Emmer, C. R. Bukowsky, J. V Lloyd, S. Yalamanchili, and H. A. Atwater, "Effectively Transparent Front Contacts for Optoelectronic Devices," Adv. Opt. Mater. **4**(10), 1470–1474 (2016).

41. R. Saive, M. Boccard, T. Saenz, S. Yalamanchili, C. R. Bukowsky, P. Jahelka, Z. J. Yu, J. Shi, Z. Holman, H. A. Atwater, J. Y. Zhengshan, J. Shi, Z. Holman, and H. A. Atwater, "Silicon heterojunction solar cells with effectively transparent front contacts," Sustain. Energy Fuels **1**(3), 593–598 (2017).

42. R. Saive and H. A. Atwater, "Mesoscale trumps nanoscale: metallic mesoscale contact morphology for improved light trapping, optical absorption and grid conductance in silicon solar cells," Opt. Express **26**(6), A275 (2018).

43. H. Jiang, W. Shi, A. Shaikh, and E. Graddy, "Advanced screen printed polymer Ag paste for HIT cells," in *2011 37th IEEE Photovoltaic Specialists Conference* (IEEE, 2011), pp. 001456–001457.

44. T. Söderström, P. Papet, and J. Ufheil, "Smart Wire Connection Technology," in *28th European Photovoltaic Solar Energy Conference and Exhibition* (2013), pp. 495–499.

45. A. W. Blakers, "Shading losses of solar-cell metal grids," J. Appl. Phys. **71**(10), 5237–5241 (1992).

46. M. F. Stuckings and A. W. Blakers, "A study of shading and resistive loss from the fingers of encapsulated solar cells," Sol. Energy Mater. Sol. Cells **59**(3), 233–242 (1999).

47. M. Powalla, D. Hariskos, E. Lotter, M. Oertel, J. Springer, D. Stellbogen, B. Dimmler, and R. Schäffler, "Large-area CIGS modules: processes and properties," Thin Solid Films **431–432**, 523–533 (2003).

48. R. Gehlhaar, T. Merckx, C. M. de la Huerta, W. Qiu, D. Cheyns, and T. Aernouts, "Perovskite solar modules with minimal area loss interconnections," SPIE Newsroom (2015).

49. W. Qiu, T. Merckx, M. Jaysankar, C. Masse de la Huerta, L. Rakocevic, W. Zhang, U. W. Paetzold, R. Gehlhaar, L. Froyen, J. Poortmans, D. Cheyns, H. J. Snaith, and P. Heremans, "Pinhole-free perovskite films for efficient solar modules," Energy Environ. Sci. **9**(2), 484–489 (2016).

50. U. W. Paetzold, M. Jaysankar, R. Gehlhaar, E. Ahlswede, S. Paetel, W. Qiu, J. Bastos, L. Rakocevic, B. S. Richards, T. Aernouts, M. Powalla, and J. Poortmans, "Scalable perovskite/CIGS thin-film solar module with power conversion efficiency of 17.8%," J. Mater. Chem. A **5**(20), 9897–9906 (2017).

51. L. Rakocevic, R. Gehlhaar, T. Merckx, W. Qiu, U. W. Paetzold, H. Fledderus, and J. Poortmans, "Interconnection Optimization for Highly Efficient Perovskite Modules," IEEE J. Photovoltaics **7**(1), 404–408 (2017).

52. L. Kuna, G. C. Eder, C. Leiner, and G. Peharz, "Reducing shadowing losses with femtosecond-laser-

written deflective optical elements in the bulk of EVA encapsulation," Prog. Photovoltaics Res. Appl. **23**(9), 1120–1130 (2015).

53. I. Mingareev, R. Berlich, T. J. Eichelkraut, H. Herfurth, S. Heinemann, and M. C. Richardson, "Diffractive optical elements utilized for efficiency enhancement of photovoltaic modules," Opt. Express **19**(12), 11397 (2011).

54. P. Jahelka, R. Saive, and H. Atwater, "Total Internal Reflection for Effectively Transparent Solar Cell Contacts," http://arxiv.org/abs/1610.01047 (accessed July 5, 2017).

55. F. Chen, S. Pathreeker, J. Kaur, and I. D. Hosein, "Increasing light capture in silicon solar cells with encapsulants incorporating air prisms to reduce metallic contact losses," Opt. Express **24**(22), A1419–A1430 (2016).

56. A. Meulenberg, "The Sawtooth Coverslide: A New Means of Coupling Light into Solar Cells," J. Energy **1**(3), 151–154 (1977).

57. A. Boca, K. M. Edmondson, and R. R. King, "Prismatic covers for boosting the efficiency of high-concentration PV systems," in *2009 34th IEEE Photovoltaic Specialists Conference (PVSC)* (IEEE, 2009), pp. 131–136.

58. V. M. Andreev, A. B. Kazantsev, V. P. Khvostikov, E. V. Paleeva, V. D. Rumyantsev, and M. Z. Shvarts, "High-efficiency (24.6% AM 0) LPE grown AlGaAs/GaAs concentrator solar cells and modules," in *Proceedings of 1994 IEEE 1st World Conference on Photovoltaic Energy Conversion* (IEEE, 1994), **2**, pp. 2096–2099.

59. J. Zhao, A. Wang, and M. A. Green, "An optimized prismatic cover design for concentrator and nonconcentrator solar cells," J. Appl. Phys. **68**(3), 1345–1350 (1990).

60. M. F. Schumann, S. Wiesendanger, J. C. Goldschmidt, B. Bläsi, K. Bittkau, U. W. Paetzold, A. Sprafke, R. B. Wehrspohn, C. Rockstuhl, and M. Wegener, "Cloaked contact grids on solar cells by coordinate transformations: designs and prototypes," Optica **2**(10), 850–853 (2015).

61. R. Saive, H. A. Atwater, S. Yalamanchili, C. Bukowsky, and T. Russell, "Fabrication processes for effectively transparent contacts," U.S. patent 15999264 (August 17, 2018).

62. R. Saive, H. A. Atwater, S. Coplin, M. Kelzenberg, S. Yalamanchili, C. Bukowsky, and T. Russell, "Superstrates Incorporating Effectively Transparent Contacts and Related Methods of Manufacturing," U.S. patent 16192704 (November 15, 2018).

63. M. F. Schumann, S. Wiesendanger, J.-C. Goldschmidt, K. Bittkau, U. W. Paetzold, A. Sprafke, R. B. Wehrspohn, C. Rockstuhl, and M. Wegener, "Cloaking of Metal Contacts on Solar Cells," in *CLEO: 2015* (OSA, 2015), (JUNE), p. SW1I.6.

64. M. F. Schumann, M. Langenhorst, M. Smeets, K. Ding, U. W. Paetzold, and M. Wegener, "All-Angle Invisibility Cloaking of Contact Fingers on Solar Cells by Refractive Free-Form Surfaces," Adv. Opt. Mater. **5**(17), 1700164 (2017).

65. P. Würfel, *Physics of Solar Cells: From Basic Principles to Advanced Concepts* (Wiley-VCH, 2016).

66. M. A. Green, *Solar Cells: Operating Principles, Technology and System Applications / Martin A. Green* (University of New South Wales, 1992).

67. American Society for Testing and Materials (ASTM), "Solar Spectral Irradiance: Air Mass 1.5," https://rredc.nrel.gov/solar//spectra/am1.5/ (accessed June 5, 2019).

68. C. A. Gueymard, D. Myers, and K. Emery, "Proposed reference irradiance spectra for solar energy systems testing," Sol. Energy **73**(6), 443–467 (2002).

69. C. D. Bailie, M. G. Christoforo, J. P. Mailoa, A. R. Bowring, E. L. Unger, W. H. Nguyen, J. Burschka, N.

Pellet, J. Z. Lee, M. Grätzel, R. Noufi, T. Buonassisi, A. Salleo, and M. D. McGehee, "Semi-transparent perovskite solar cells for tandems with silicon and CIGS," Energy Environ. Sci. **8**(3), 956–963 (2015).

70. C. Schultz, M. Schüle, M. Richter, H.-U. Pahl, H. Endert, J. Bonse, I. Dirnstorfer, B. Rau, R. Schlatmann, V. Quaschning, F. Fink, and B. Stegemann, "P1 , P2 and P3 structuring of CIGSE solar cells with a single laser wavelength," in *26th European Photovoltaic Solar Energy Conference and Exhibition* (2011), pp. 2540–2543.

71. J. C. Maxwell, "A Dynamical Theory of the Electromagnetic Field," Philos. Trans. R. Soc. London **155**, 459–512 (1865).

72. J. D. Jackson, *Klassische Elektrodynamik* (De Gruyter, 2006).

73. E. Hecht, *Optik* (De Gruyter, 2014).

74. J. B. Pendry, "Controlling Electromagnetic Fields," Science **312**(5781), 1780–1782 (2006).

75. C. C. Katsidis and D. I. Siapkas, "General transfer-matrix method for optical multilayer systems with coherent, partially coherent, and incoherent interference," Appl. Opt. **41**(19), 3978–3987 (2002).

76. S. J. Byrnes, "Multilayer optical calculations," http://arxiv.org/abs/1603.02720.

77. S. C. Baker-Finch, K. R. McIntosh, S. C. Baker-Finch, and K. R. McIntosh, "Reflection of normally incident light from silicon solar cells with pyramidal texture," Prog. Photovoltaics Res. Appl. **19**(4), 406–416 (2011).

78. "OPAL 2," https://www2.pvlighthouse.com.au/calculators/OPAL 2/OPAL 2.aspx (accessed May 15, 2019).

79. K. R. McIntosh and S. C. Baker-Finch, "OPAL 2: Rapid optical simulation of silicon solar cells," in *2012 38th IEEE Photovoltaic Specialists Conference* (IEEE, 2012), pp. 000265–000271.

80. G. Yun, K. Crabtree, and R. a. Chipman, "Properties of the polarization ray tracing matrix," in *Polarization Science and Remote Sensing III*, J. A. Shaw and J. S. Tyo, eds. (2007), **6682**(September 2007), p. 66820Z.

81. N. Buch-Månson, A. Spangenberg, L. P. C. Gomez, J.-P. Malval, O. Soppera, and K. L. Martinez, "Rapid Prototyping of Polymeric Nanopillars by 3D Direct Laser Writing for Controlling Cell Behavior," Sci. Rep. **7**(1), 9247 (2017).

82. R. G. Gordon, "ALD Precursors and Reaction Mechanisms," in *Atomic Layer Deposition for Semiconductors*, C. S. Hwang, ed. (Springer US, 2014), pp. 15–46.

83. J. Dendooven and C. Detavernier, "Basics of Atomic Layer Deposition: Growth Characteristics and Conformality," in *Atomic Layer Deposition in Energy Conversion Applications* (Wiley-VCH Verlag GmbH & Co. KGaA, 2017), pp. 1–40.

84. M. Colburn, S. C. Johnson, M. D. Stewart, S. Damle, T. C. Bailey, B. Choi, M. Wedlake, T. B. Michaelson, S. V. Sreenivasan, J. G. Ekerdt, and C. G. Willson, "Step and flash imprint lithography: a new approach to high-resolution patterning," in *Emerging Lithographic Technologies III*, Y. Vladimirsky, ed. (1999), **Proc. SPIE**.

85. M. Bender, M. Otto, B. Hadam, B. Vratzov, B. Spangenberg, and H. Kurz, "Fabrication of nanostructures using a UV-based imprint technique," Microelectron. Eng. **53**(1), 233–236 (2000).

86. U. Plachetka, M. Bender, A. Fuchs, B. Vratzov, T. Glinsner, F. Lindner, and H. Kurz, "Wafer scale patterning by soft UV-Nanoimprint Lithography," Microelectron. Eng. **73**–**74**(June 2004), 167–171 (2004).

87. M. Meier, C. Nauenheim, S. Gilles, D. Mayer, C. Kügeler, and R. Waser, "Nanoimprint for future non-

volatile memory and logic devices," Microelectron. Eng. **85**(5–6), 870–872 (2008).

88. K. Wilken, U. W. Paetzold, M. Meier, N. Prager, M. Fahland, F. Finger, and V. Smirnov, "Nanoimprint texturing of transparent flexible substrates for improved light management in thin-film solar cells," Phys. Status Solidi - Rapid Res. Lett. **9**(4), 215–219 (2015).

89. M. Komuro, J. Taniguchi, Y. Tokano, S. Inoue, N. Kimura, H. Hiroshima, and S. Matsui, "Imprinting characteristics by photo-induced solidification of liquid polymer," Dig. Pap. - 2000 Int. Microprocess. Nanotechnol. Conf. MNC 2000 294–295 (2000).

90. C. Battaglia, J. Escarré, K. Söderström, L. Erni, L. Ding, G. Bugnon, A. Billet, M. Boccard, L. Barraud, S. De Wolf, F. J. Haug, M. Despeisse, and C. Ballif, "Nanoimprint lithography for high-efficiency thin-film silicon solar cells," Nano Lett. **11**(2), 661–665 (2011).

91. M. Langenhorst, D. Ritzer, F. Kotz, P. Risch, S. Dottermusch, A. Roslizar, R. Schmager, B. S. Richards, B. E. Rapp, and U. W. Paetzold, "Liquid Glass for Photovoltaics: Multifunctional Front Cover Glass for Solar Modules," ACS Appl. Mater. Interfaces **11**(38), 35015–35022 (2019).

92. F. Kotz, K. Plewa, W. Bauer, N. Schneider, N. Keller, T. Nargang, D. Helmer, K. Sachsenheimer, M. Schäfer, M. Worgull, C. Greiner, C. Richter, and B. E. Rapp, "Liquid Glass: A Facile Soft Replication Method for Structuring Glass," Adv. Mater. **28**(23), 4646–4650 (2016).

93. F. Kotz, N. Schneider, A. Striegel, A. Wolfschläger, N. Keller, M. Worgull, W. Bauer, D. Schild, M. Milich, C. Greiner, D. Helmer, and B. E. Rapp, "Glassomer-Processing Fused Silica Glass Like a Polymer," Adv. Mater. **30**(22), 1707100 (2018).

94. F. Kotz, K. Arnold, W. Bauer, D. Schild, N. Keller, K. Sachsenheimer, T. M. Nargang, C. Richter, D. Helmer, and B. E. Rapp, "Three-dimensional printing of transparent fused silica glass," Nature **544**(7650), 337–339 (2017).

95. T. Abzieher, J. A. Schwenzer, S. Moghadamzadeh, F. Sutterluti, I. M. Hossain, M. Pfau, E. Lotter, M. Hetterich, B. S. Richards, U. Lemmer, M. Powalla, and U. W. Paetzold, "Efficient All-Evaporated pin-Perovskite Solar Cells: A Promising Approach Toward Industrial Large-Scale Fabrication," IEEE J. Photovoltaics **9**(5), 1249–1257 (2019).

96. H. Frey and H. R. Khan, *Handbook of Thin-Film Technology* (Springer Berlin Heidelberg, 2015).

97. J. Girkin, *A Practical Guide to Optical Microscopy*, 1st ed. (Routledge, 2019).

98. B. Voigtländer, *Atomic Force Microscopy*, NanoScience and Technology (Springer International Publishing, 2019).

99. T. A. Germer, J. C. Zwinkels, and B. K. Tsai, *Spectrophotometry: Accurate Measurement of Optical Properties of Materials*, Experimental Methods in the Physical Sciences; 46 (Elsevier, 2014).

100. A. International, "Standard Test Method for Film Hardness by Pencil Test," https://compass.astm.org/EDIT/html_annot.cgi?D3363+05(2011)e2 (accessed October 17, 2019).

101. H. Schulte-Huxel, T. J. Silverman, M. G. Deceglie, D. J. Friedman, and A. C. Tamboli, "Energy Yield Analysis of Multiterminal Si-Based Tandem Solar Cells," IEEE J. Photovoltaics **8**(5), 1376–1383 (2018).

102. S. Senthilarasu, E. F. Fernández, F. Almonacid, and T. K. Mallick, "Effects of spectral coupling on perovskite solar cells under diverse climatic conditions," Sol. Energy Mater. Sol. Cells **133**, 92–98 (2015).

103. H. Liu, Z. Ren, Z. Liu, A. G. Aberle, T. Buonassisi, and I. M. Peters, "The realistic energy yield potential of GaAs-on-Si tandem solar cells: a theoretical case study," Opt. Express **23**(7), A382 (2015).

104. S. P. Philipps, G. Peharz, R. Hoheisel, T. Hornung, N. M. Al-Abbadi, F. Dimroth, and A. W. Bett, "Energy harvesting efficiency of III–V triple-junction concentrator solar cells under realistic spectral

conditions," Sol. Energy Mater. Sol. Cells **94**(5), 869–877 (2010).

105. R. Hosseinian Ahangharnejhad, A. B. Phillips, K. Ghimire, P. Koirala, Z. Song, H. M. Barudi, A. Habte, M. Sengupta, R. J. Ellingson, Y. Yan, R. W. Collins, N. J. Podraza, and M. J. Heben, "Irradiance and temperature considerations in the design and deployment of high annual energy yield perovskite/CIGS tandems," Sustain. Energy Fuels (2019).

106. A. Calcabrini, H. Ziar, O. Isabella, and M. Zeman, "A simplified skyline-based method for estimating the annual solar energy potential in urban environments," Nat. Energy **4**(3), 206–215 (2019).

107. R. Schmager, M. Langenhorst, J. Lehr, U. Lemmer, B. S. Richards, and U. W. Paetzold, "Methodology of energy yield modelling of perovskite-based multi-junction photovoltaics," Opt. Express **27**(8), A507 (2019).

108. S. Wilcox and W. Marion, "Users Manual for TMY3 Data Sets," https://www.nrel.gov/docs/fy08osti/43156.Pdf (accessed October 23, 2017).

109. C. A. Gueymard, "Parameterized transmittance model for direct beam and circumsolar spectral irradiance," Sol. Energy **71**(5), 325–346 (2001).

110. J. S. Bartlett, Á. M. Ciotti, R. F. Davis, and J. J. Cullen, "The spectral effects of clouds on solar irradiance," J. Geophys. Res. Ocean. **103**(C13), 31017–31031 (1998).

111. C. R. Osterwald, K. A. Emery, and M. Muller, "Photovoltaic module calibration value versus optical air mass: the air mass function," Prog. Photovoltaics Res. Appl. **22**(5), 560–573 (2014).

112. X. Liu, Q. Yang, H. Li, Z. Jin, W. Wu, S. Kizer, D. K. Zhou, and P. Yang, "Development of a fast and accurate PCRTM radiative transfer model in the solar spectral region," Appl. Opt. **55**(29), 8236 (2016).

113. H. H. Aumann, X. Chen, E. Fishbein, A. Geer, S. Havemann, X. Huang, X. Liu, G. Liuzzi, S. DeSouza-Machado, E. M. Manning, G. Masiello, M. Matricardi, I. Moradi, V. Natraj, C. Serio, L. Strow, J. Vidot, R. Chris Wilson, W. Wu, Q. Yang, and Y. L. Yung, "Evaluation of Radiative Transfer Models With Clouds," J. Geophys. Res. Atmos. **123**(11), 6142–6157 (2018).

114. J. Eisenlohr, N. Tucher, O. Höhn, H. Hauser, M. Peters, P. Kiefel, J. C. Goldschmidt, and B. Bläsi, "Matrix formalism for light propagation and absorption in thick textured optical sheets," Opt. Express **23**(11), A502 (2015).

115. N. Tucher, J. Eisenlohr, P. Kiefel, O. Höhn, H. Hauser, M. Peters, C. Müller, J. C. Goldschmidt, and B. Bläsi, "3D optical simulation formalism OPTOS for textured silicon solar cells," Opt. Express **23**(24), A1720 (2015).

116. M. K. Fuentes, *A Simplified Thermal Model for Flat-Plate Photovoltaic Arrays* (1987).

117. R. G. Ross Jr, "Flat-plate photovoltaic array design optimization," in *14th IEEE Photovoltaic Specialists Conference* (1980), pp. 1126–1132.

118. R. G. Ross Jr and M. I. Smokler, *Flat-Plate Solar Array Project: Final Report: Volume 6, Engineering Sciences and Reliability* (1986).

119. O. Dupré, R. Vaillon, and M. A. Green, "Physics of the temperature coefficients of solar cells," Sol. Energy Mater. Sol. Cells **140**, 92–100 (2015).

120. R. M. Corless, G. H. Gonnet, D. E. G. Hare, D. J. Jeffrey, and D. E. Knuth, "On the LambertW function," Adv. Comput. Math. **5**(1), 329–359 (1996).

121. X. Gao, Y. Cui, J. Hu, G. Xu, and Y. Yu, "Lambert W-function based exact representation for double diode model of solar cells: Comparison on fitness and parameter extraction," Energy Convers. Manag. **127**, 443–460 (2016).

122. A. Jain and A. Kapoor, "Exact analytical solutions of the parameters of real solar cells using Lambert W -function," Sol. Energy Mater. Sol. Cells **81**, 269–277 (2004).

123. Johann Heinrich Lambert, *Photometria, Sive de Mensura Et Gradibus Luminis, Colorum Et Umbra* (1760).

124. D. A. Jacobs, M. Langenhorst, F. Sahli, B. S. Richards, T. P. White, C. Ballif, K. R. Catchpole, and U. W. Paetzold, "Light Management: A Key Concept in High-Efficiency Perovskite/Silicon Tandem Photovoltaics," J. Phys. Chem. Lett. **10**(11), 3159–3170 (2019).

125. J. Werner, G. Dubuis, A. Walter, P. Löper, S.-J. Moon, S. Nicolay, M. Morales-Masis, S. De Wolf, B. Niesen, and C. Ballif, "Sputtered rear electrode with broadband transparency for perovskite solar cells," Sol. Energy Mater. Sol. Cells **141**, 407–413 (2015).

126. K. A. Bush, A. F. Palmstrom, Z. J. Yu, M. Boccard, R. Cheacharoen, J. P. Mailoa, D. P. McMeekin, R. L. Z. Hoye, C. D. Bailie, T. Leijtens, I. M. Peters, M. C. Minichetti, N. Rolston, R. Prasanna, S. Sofia, D. Harwood, W. Ma, F. Moghadam, H. J. Snaith, T. Buonassisi, Z. C. Holman, S. F. Bent, and M. D. McGehee, "23.6%-Efficient Monolithic Perovskite/Silicon Tandem Solar Cells With Improved Stability," Nat. Energy **2**(4), 1–7 (2017).

127. Y. Wu, D. Yan, J. Peng, T. Duong, Y. Wan, S. P. Phang, H. Shen, N. Wu, C. Barugkin, X. Fu, S. Surve, D. Grant, D. Walter, T. P. White, K. R. Catchpole, and K. J. Weber, "Monolithic perovskite/silicon-homojunction tandem solar cell with over 22% efficiency," Energy Environ. Sci. **10**(11), 2472–2479 (2017).

128. J. Werner, C.-H. Weng, A. Walter, L. Fesquet, J. P. Seif, S. De Wolf, B. Niesen, and C. Ballif, "Efficient Monolithic Perovskite/Silicon Tandem Solar Cell with Cell Area >1 cm^2," J. Phys. Chem. Lett. **7**(1), 161–166 (2016).

129. S. Albrecht, M. Saliba, J. P. Correa Baena, F. Lang, L. Kegelmann, M. Mews, L. Steier, A. Abate, J. Rappich, L. Korte, R. Schlatmann, M. K. Nazeeruddin, A. Hagfeldt, M. Grätzel, and B. Rech, "Monolithic perovskite/silicon-heterojunction tandem solar cells processed at low temperature," Energy Environ. Sci. **9**(1), 81–88 (2016).

130. J. P. Mailoa, C. D. Bailie, E. C. Johlin, E. T. Hoke, A. J. Akey, W. H. Nguyen, M. D. McGehee, and T. Buonassisi, "A 2-terminal perovskite/silicon multijunction solar cell enabled by a silicon tunnel junction," Appl. Phys. Lett. **106**(12), (2015).

131. J. Werner, L. Barraud, A. Walter, M. Bräuninger, F. Sahli, D. Sacchetto, N. Tétreault, B. Paviet-Salomon, S.-J. Moon, C. Allebé, M. Despeisse, S. Nicolay, S. De Wolf, B. Niesen, and C. Ballif, "Efficient Near-Infrared-Transparent Perovskite Solar Cells Enabling Direct Comparison of 4-Terminal and Monolithic Perovskite/Silicon Tandem Cells," ACS Energy Lett. **1**(2), 474–480 (2016).

132. B. Chen, Y. Bai, Z. Yu, T. Li, X. Zheng, Q. Dong, L. Shen, M. Boccard, A. Gruverman, Z. Holman, and J. Huang, "Efficient Semitransparent Perovskite Solar Cells for 23.0%-Efficiency Perovskite/Silicon Four-Terminal Tandem Cells," Adv. Energy Mater. **6**(19), 1601128 (2016).

133. P. Löper, S.-J. Moon, S. Martín de Nicolas, B. Niesen, M. Ledinsky, S. Nicolay, J. Bailat, J.-H. Yum, S. De Wolf, and C. Ballif, "Organic–inorganic halide perovskite/crystalline silicon four-terminal tandem solar cells," Phys. Chem. Chem. Phys. **17**(3), 1619–1629 (2015).

134. A. Richter, J. Benick, F. Feldmann, A. Fell, M. Hermle, and S. W. Glunz, "n-Type Si solar cells with passivating electron contact: Identifying sources for efficiency limitations by wafer thickness and resistivity variation," Sol. Energy Mater. Sol. Cells **173**, 96–105 (2017).

135. J. Escarré, K. Söderström, M. Despeisse, S. Nicolay, C. Battaglia, G. Bugnon, L. Ding, F. Meillaud, F.-J. Haug, and C. Ballif, "Geometric light trapping for high efficiency thin film silicon solar cells," Sol. Energy Mater. Sol. Cells **98**, 185–190 (2012).

136. J.-W. Schüttauf, G. Bugnon, M. Stuckelberger, S. Hanni, M. Boccard, M. Despeisse, F.-J. Haug, F. Meillaud, and C. Ballif, "Thin-Film Silicon Triple-Junction Solar Cells on Highly Transparent Front Electrodes With Stabilized Efficiencies up to 12.8%," IEEE J. Photovoltaics **4**(3), 757–762 (2014).

137. C. Ulbrich, A. Gerber, K. Hermans, A. Lambertz, and U. Rau, "Analysis of short circuit current gains by an anti-reflective textured cover on silicon thin film solar cells," Prog. Photovoltaics Res. Appl. **21**(8), 1672–1681 (2013).

138. G. Köppel, V. Preidel, S. Mangold, E. Rudigier-Voigt, M. Hývl, A. Fejfar, B. Rech, and C. Becker, "Nanoimprint-textured Glass Superstrates for Light Trapping in Crystalline Silicon thin-film Solar Cells," Energy Procedia **84**, 118–126 (2015).

139. F. Back, M. Bockmeyer, E. Rudigier-Voigt, and P. Löbmann, "Periodic nanostructures imprinted on high-temperature stable sol–gel films by ultraviolet-based nanoimprint lithography for photovoltaic and photonic applications," Thin Solid Films **562**, 274–281 (2014).

140. S. W. Youn, M. Takahashi, H. Goto, and R. Maeda, "Microstructuring of glassy carbon mold for glass embossing – Comparison of focused ion beam, nano/femtosecond-pulsed laser and mechanical machining," Microelectron. Eng. **83**(11–12), 2482–2492 (2006).

141. X. Luo, L. Lu, M. Yin, X. Fang, X. Chen, D. Li, L. Yang, G. Li, and J. Ma, "Antireflective and self-cleaning glass with robust moth-eye surface nanostructures for photovoltaic utilization," Mater. Res. Bull. **109**, 183–189 (2019).

142. E. Vazsonyi, K. De Clercq, R. Einhaus, E. Van Kerschaver, K. Said, J. Poortmans, J. Szlufcik, and J. Nijs, "Improved anisotropic etching process for industrial texturing of silicon solar cells," Sol. Energy Mater. Sol. Cells **57**(2), 179–188 (1999).

143. J. Borchert, R. L. Milot, J. B. Patel, C. L. Davies, A. D. Wright, L. Martínez Maestro, H. J. Snaith, L. M. Herz, M. B. Johnston, L. Martínez Maestro, H. J. Snaith, L. M. Herz, and M. B. Johnston, "Large-Area, Highly Uniform Evaporated Formamidinium Lead Triiodide Thin Films for Solar Cells," ACS Energy Lett. **2**(12), 2799–2804 (2017).

144. K. A. Bush, S. Manzoor, K. Frohna, Z. J. Yu, J. A. Raiford, A. F. Palmstrom, H.-P. Wang, R. Prasanna, S. F. Bent, and Z. C. Holman, "Minimizing Current and Voltage Losses to Reach 25% Efficient Monolithic Two-Terminal Perovskite–Silicon Tandem Solar Cells," ACS Energy Lett. **3**(9), 2173–2180 (2018).

145. "ENF. Glass Manufacturers," https://www.enfsolar.com/directory/material/glass (accessed June 17, 2019).

146. D. C. Miller, E. Annigoni, A. Ballion, J. G. Bokria, L. S. Bruckman, D. M. Burns, X. Chen, J. Feng, R. H. French, S. Fowler, C. C. Honeker, M. D. Kempe, H. Khonkar, M. Kohl, L.-E. Perret-Aebi, N. H. Phillips, K. P. Scott, F. Sculati-Meillaud, and J. H. Wohlgemuth, "Degradation in PV encapsulant strength of attachment: An interlaboratory study towards a climate-specific test," in *2016 IEEE 43rd Photovoltaic Specialists Conference (PVSC)* (IEEE, 2016), pp. 0095–0100.

147. E. Yousif and R. Haddad, "Photodegradation and photostabilization of polymers, especially polystyrene: review," Springerplus **2**(1), 398 (2013).

148. S.-Y. Chen, Y.-H. Lin, S.-P. Hsu, C.-P. Huang, L.-Y. Li, and C.-H. Du, "Industrially PERC Solar Cells with Integrated Front-Side Optimization," in *2018 IEEE 7th World Conference on Photovoltaic Energy Conversion (WCPEC) (A Joint Conference of 45th IEEE PVSC, 28th PVSEC & 34th EU PVSEC)* (IEEE, 2018), pp. 0980–0982.

149. L. Mazzarella, M. Werth, K. Jäger, M. Jošt, L. Korte, S. Albrecht, R. Schlatmann, and B. Stannowski, "Infrared photocurrent management in monolithic perovskite/silicon heterojunction tandem solar cells by using a nanocrystalline silicon oxide interlayer," Opt. Express **26**(10), A487 (2018).

150. D. Liu, Q. Wang, C. J. Traverse, C. Yang, M. Young, P. S. Kuttipillai, S. Y. Lunt, T. W. Hamann, and R. R.

Lunt, "Impact of Ultrathin C60on Perovskite Photovoltaic Devices," ACS Nano (2018).

151. F. Sahli, B. A. Kamino, J. Werner, M. Bräuninger, B. Paviet-Salomon, L. Barraud, R. Monnard, J. P. Seif, A. Tomasi, Q. Jeangros, A. Hessler-Wyser, S. De Wolf, M. Despeisse, S. Nicolay, B. Niesen, and C. Ballif, "Improved Optics in Monolithic Perovskite/Silicon Tandem Solar Cells with a Nanocrystalline Silicon Recombination Junction," Adv. Energy Mater. **8**(6), 1701609 (2018).

152. J. Zheng, C. F. J. Lau, H. Mehrvarz, F.-J. Ma, Y. Jiang, X. Deng, A. Soeriyadi, J. Kim, M. Zhang, L. Hu, X. Cui, D. S. Lee, J. Bing, Y. Cho, C. Chen, M. A. Green, S. Huang, and A. W. Y. Ho-Baillie, "Large area efficient interface layer free monolithic perovskite/homo-junction-silicon tandem solar cell with over 20% efficiency," Energy Environ. Sci. **11**(9), 2432–2443 (2018).

153. H. Shen, S. T. Omelchenko, D. A. Jacobs, S. Yalamanchili, Y. Wan, D. Yan, P. Phang, T. Duong, Y. Wu, Y. Yin, C. Samundsett, J. Peng, N. Wu, T. P. White, G. G. Andersson, N. S. Lewis, and K. R. Catchpole, "In situ recombination junction between p-Si and TiO 2 enables high-efficiency monolithic perovskite/Si tandem cells," Sci. Adv. **4**(12), eaau9711 (2018).

154. D. K. Cai, A. Neyer, R. Kuckuk, and H. M. Heise, "Optical absorption in transparent PDMS materials applied for multimode waveguides fabrication," Opt. Mater. (Amst). **30**(7), 1157–1161 (2008).

155. M. Morales-Masis, S. De Wolf, R. Woods-Robinson, J. W. Ager, and C. Ballif, "Transparent Electrodes for Efficient Optoelectronics," Adv. Electron. Mater. **3**(5), 1600529 (2017).

156. T. Duong, N. Lal, D. Grant, D. Jacobs, P. Zheng, S. Rahman, H. Shen, M. Stocks, A. Blakers, K. Weber, T. P. White, and K. R. Catchpole, "Semitransparent Perovskite Solar Cell With Sputtered Front and Rear Electrodes for a Four-Terminal Tandem," IEEE J. Photovoltaics **6**(3), 679–687 (2016).

157. B. A. Kamino, B. Paviet-Salomon, S.-J. Moon, N. Badel, J. Levrat, G. Christmann, A. Walter, A. Faes, L. Ding, J. J. Diaz Leon, A. Paracchino, M. Despeisse, C. Ballif, and S. Nicolay, "Low-Temperature Screen-Printed Metallization for the Scale-Up of Two-Terminal Perovskite–Silicon Tandems," ACS Appl. Energy Mater. **2**(5), 3815–3821 (2019).

158. M. van Eerden, M. Jaysankar, A. Hadipour, T. Merckx, J. J. Schermer, T. Aernouts, J. Poortmans, and U. W. Paetzold, "Optical Analysis of Planar Multicrystalline Perovskite Solar Cells," Adv. Opt. Mater. **5**(18), 1700151 (2017).

159. P. Jackson, R. Wuerz, D. Hariskos, E. Lotter, W. Witte, and M. Powalla, "Effects of heavy alkali elements in Cu(In,Ga)Se 2 solar cells with efficiencies up to 22.6%," Phys. status solidi - Rapid Res. Lett. **10**(8), 583–586 (2016).

160. S. Gharibzadeh, B. Abdollahi Nejand, M. Jakoby, T. Abzieher, D. Hauschild, S. Moghadamzadeh, J. A. Schwenzer, P. Brenner, R. Schmager, A. A. Haghighirad, L. Weinhardt, U. Lemmer, B. S. Richards, I. A. Howard, and U. W. Paetzold, "Record Open-Circuit Voltage Wide-Bandgap Perovskite Solar Cells Utilizing 2D/3D Perovskite Heterostructure," Adv. Energy Mater. **9**(21), 1803699 (2019).

161. M. C. Peel, B. L. Finlayson, and T. A. McMahon, "Updated world map of the Köppen-Geiger climate classification," Hydrol. Earth Syst. Sci. **11**(5), 1633–1644 (2007).

162. P. F. Ndione, Z. Li, and K. Zhu, "Effects of alloying on the optical properties of organic–inorganic lead halide perovskite thin films," J. Mater. Chem. C **4**(33), 7775–7782 (2016).

163. "Datenblatt SunPower MAXEON 3 (400W)," https://www.sunpower.de/sites/default/files/sunpower-maxeon-3-module-private-anwendungen-400-390-370.pdf (accessed July 16, 2019).

164. "SunPower X-Serie: X22-360," https://us.sunpower.com/sites/default/files/media-library/data-sheets/sunpower-x-series-residential-solar-panels-x22-360-datasheet-514618-revc.pdf (accessed July 16, 2019).

165. I. Haedrich, U. Eitner, M. Wiese, and H. Wirth, "Unified methodology for determining CTM ratios:

Systematic prediction of module power," Sol. Energy Mater. Sol. Cells **131**(7), 14–23 (2014).

166. M. Peters, S. Guo, and Z. Liu, "Full loss analysis for a multicrystalline silicon wafer solar cell PV module at short-circuit conditions," Prog. Photovoltaics Res. Appl. **24**(4), 560–569 (2016).

167. S. Braun, G. Micard, and G. Hahn, "Solar Cell Improvement by using a Multi Busbar Design as Front Electrode," Energy Procedia **27**(April), 227–233 (2012).

168. A. W. Blakers, "Shading losses of solar-cell metal grids," J. Appl. Phys. **71**(10), 5237–5241 (1992).

169. H. B. Serreze, "Optimizing Solar Cell Performance by Simultaneous Consideration of Grid Pattern Design and Interconnect Configurations," in *13th IEEE Photovoltaic Specialists Conference* (1978), pp. 1–8.

170. G. Beaucarne, G. Schubert, L. Tous, and J. Hoornstra, "Summary of the 6 th Workshop on Metallization and Interconnection for Crystalline Silicon Solar Cells," Energy Procedia **98**, 2–11 (2016).

171. R. Bartlome, B. Strahm, Y. Sinquin, A. Feltrin, and C. Ballif, "Laser applications in thin-film photovoltaics," Appl. Phys. B Lasers Opt. **100**(2), 427–436 (2010).

172. S.-J. Moon, J.-H. Yum, L. Lofgren, A. Walter, L. Sansonnens, M. Benkhaira, S. Nicolay, J. Bailat, and C. Ballif, "Laser-Scribing Patterning for the Production of Organometallic Halide Perovskite Solar Modules," IEEE J. Photovoltaics **5**(4), 1087–1092 (2015).

173. G. Eberhardt, H. Banse, U. Wagner, and T. Peschel, "Structuring of thin film solar cells," in *Laser-Based Micro- and Nanopackaging and Assembly IV*, W. Pfleging, Y. Lu, K. Washio, J. Amako, and W. Hoving, eds. (2010), **7585**(February 2010), p. 75850P.

174. M. Langenhorst, M. F. Schumann, S. Paetel, R. Schmager, U. Lemmer, B. S. Richards, M. Wegener, and U. W. Paetzold, "Freeform surface invisibility cloaking of interconnection lines in thin-film photovoltaic modules," Sol. Energy Mater. Sol. Cells **182**, 294–301 (2018).

175. M. W. Rowell and M. D. McGehee, "Transparent electrode requirements for thin film solar cell modules," Energy Environ. Sci. **4**(1), 131–134 (2011).

176. D. C. Miller and S. R. Kurtz, "Durability of Fresnel lenses: A review specific to the concentrating photovoltaic application," Sol. Energy Mater. Sol. Cells **95**(8), 2037–2068 (2011).

177. "Nanoscribe launches Quantum X for the fabrication of highly-precise microoptics," https://www.nanoscribe.com/en/news-insights/press-releases/nanoscribe-launches-quantum-x-for-the-fabrication-of-highly-precise-microoptics (accessed October 15, 2019).

178. D. Afonso, R. Alves de Sousa, R. Torcato, and L. Pires, *Incremental Forming as a Rapid Tooling Process*, SpringerBriefs in Applied Sciences and Technology (Springer International Publishing, 2019).

179. "Additive Fertigungssysteme: TruPrint 1000," https://www.trumpf.com/de_DE/produkte/maschinen-systeme/additive-fertigungssysteme/truprint-1000/ (accessed October 16, 2019).